Cell Stem Cell

Article

Modeling plasticity and dysplasia of pancreatic ductal organoids derived from human pluripotent stem cells

Graphical abstract

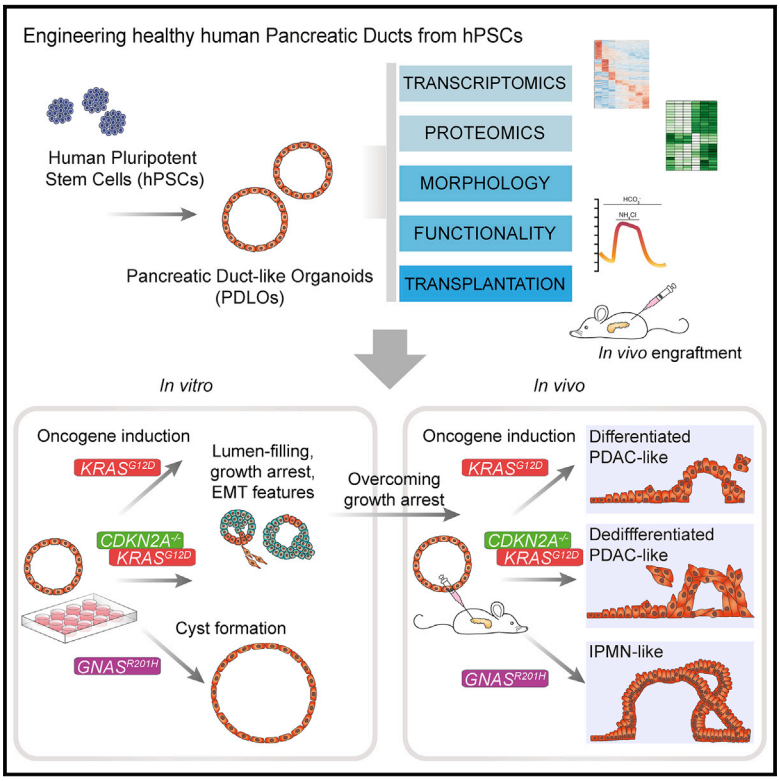

Highlights

- Robust differentiation of hPSCs into functional pancreatic duct-like organoids
- RNA-seq and proteome measurements confirm ductal identity and maturity
- Inducing KRAS^{G12D} in PDLOs causes EMT and growth arrest, GNAS$^{R201C/H}$ causes cystic growth
- PDAC- and IPMN-like tumor formation of oncogenic PDLO grafts

Authors

Markus Breunig, Jessica Merkle, Martin Wagner, ..., Matthias Meier, Meike Hohwieler, Alexander Kleger

Correspondence

alexander.kleger@uni-ulm.de

In brief

Kleger and colleagues developed a differentiation protocol guiding hPSCs into functional pancreatic duct-like organoids. Focusing on early pancreatic tumor formation, they show that the PDLO system is applicable for disease modeling *in vitro* and *in vivo*. The genetically defined background of PDLOs will allow the tracking of human pancreatic cancer development.

Breunig et al., 2021, Cell Stem Cell *28*, 1–20
June 3, 2021
https://doi.org/10.1016/j.stem.2021.03.005

CellPress

Cell Stem Cell

CellPress

Article

Modeling plasticity and dysplasia of pancreatic ductal organoids derived from human pluripotent stem cells

Markus Breunig,[1,19] Jessica Merkle,[1,19] Martin Wagner,[1] Michael K. Melzer,[1,2] Thomas F.E. Barth,[3] Thomas Engleitner,[4] Johannes Krumm,[5] Sandra Wiedenmann,[1,6] Christian M. Cohrs,[7,8,9] Lukas Perkhofer,[1] Gaurav Jain,[4] Jana Krüger,[1] Patrick C. Hermann,[1] Maximilian Schmid,[1] Tamara Madácsy,[10,11] Árpád Varga,[10,11] Joscha Griger,[4] Ninel Azoitei,[1] Martin Müller,[1] Oliver Wessely,[12] Pamela G. Robey,[13] Sandra Heller,[1] Zahra Dantes,[14] Maximilian Reichert,[14] Cagatay Günes,[2] Christian Bolenz,[2] Florian Kuhn,[1] József Maléth,[10,11,15] Stephan Speier,[7,8,9] Stefan Liebau,[16] Bence Sipos,[17] Bernhard Kuster,[5,18] Thomas Seufferlein,[1] Roland Rad,[4] Matthias Meier,[6,19,20] Meike Hohwieler,[1,19,20] and Alexander Kleger[1,19,20,21,*]

[1]Department of Internal Medicine I, Ulm University Hospital, Ulm, Germany
[2]Department of Urology, Ulm University, Ulm, Germany
[3]Institute of Pathology, Ulm University, Ulm, Germany
[4]Institute of Molecular Oncology and Functional Genomics, Center for Translational Cancer Research and Department of Medicine II, School of Medicine, Technical University of Munich, Munich, Germany
[5]Chair of Proteomics and Bioanalytics, Technical University of Munich, Freising, Germany
[6]Helmholtz Pioneer Campus, Helmholtz Zentrum München, Neuherberg, Germany
[7]Paul Langerhans Institute Dresden (PLID) of the Helmholtz Zentrum München at the University Clinic Carl Gustav Carus of Technische Universität Dresden, Helmholtz Zentrum München, Neuherberg, Germany
[8]Institute of Physiology, Faculty of Medicine, Technische Universität Dresden, Dresden, Germany
[9]German Center for Diabetes Research (DZD), Neuherberg, Germany
[10]First Department of Internal Medicine, University of Szeged, Szeged, Hungary
[11]MTA-SZTE Momentum Epithelial Cell Signalling and Secretion Research Group, University of Szeged, Szeged, Hungary
[12]Department of Cardiovascular & Metabolic Sciences, Lerner Research Institute, Cleveland, OH 44195, USA
[13]Skeletal Biology Section, National Institute of Dental and Craniofacial Research, National Institutes of Health, US Department of Health and Human Services, Bethesda, MD 20892, USA
[14]Medical Clinic and Polyclinic II, Klinikum rechts der Isar, Technical University Munich, Munich, Germany
[15]HCEMM-SZTE Molecular Gastroenterology Research Group, University of Szeged, Szeged, Hungary
[16]Institute of Neuroanatomy & Developmental Biology (INDB), Eberhard Karls University Tübingen, Tübingen, Germany
[17]Department of Internal Medicine VIII, University Hospital Tübingen, Tübingen, Germany
[18]Bavarian Biomolecular Mass Spectrometry Center (BayBioMS), Technical University of Munich, Freising, Germany
[19]These authors contributed equally
[20]Senior authors
[21]Lead contact
*Correspondence: alexander.kleger@uni-ulm.de
https://doi.org/10.1016/j.stem.2021.03.005

SUMMARY

Personalized *in vitro* models for dysplasia and carcinogenesis in the pancreas have been constrained by insufficient differentiation of human pluripotent stem cells (hPSCs) into the exocrine pancreatic lineage. Here, we differentiate hPSCs into pancreatic duct-like organoids (PDLOs) with morphological, transcriptional, proteomic, and functional characteristics of human pancreatic ducts, further maturing upon transplantation into mice. PDLOs are generated from hPSCs inducibly expressing oncogenic GNAS, KRAS, or KRAS with genetic covariance of lost CDKN2A and from induced hPSCs derived from a McCune-Albright patient. Each oncogene causes a specific growth, structural, and molecular phenotype *in vitro*. While transplanted PDLOs with oncogenic KRAS alone form heterogenous dysplastic lesions or cancer, KRAS with CDKN2A loss develop dedifferentiated pancreatic ductal adenocarcinomas. In contrast, transplanted PDLOs with mutant GNAS lead to intraductal papillary mucinous neoplasia-like structures. Conclusively, PDLOs enable *in vitro* and *in vivo* studies of pancreatic plasticity, dysplasia, and cancer formation from a genetically defined background.

Please cite this article in press as: Breunig et al., Modeling plasticity and dysplasia of pancreatic ductal organoids derived from human pluripotent stem cells, Cell Stem Cell (2021), https://doi.org/10.1016/j.stem.2021.03.005

INTRODUCTION

The ductal compartment of the pancreas is the origin of various diseases. These range from common diseases, such as pancreatic ductal adenocarcinoma (PDAC) (Ferreira et al., 2017; Lee et al., 2019; Kopp et al., 2018), to rare diseases, such as the Alagille syndrome, which is characterized by ductal malfunction (Golson et al., 2009; Gliwicz et al., 2016). *In vitro* disease models for PDAC are of major clinical relevance (Boj et al., 2015; Frappart et al., 2020; Moreira et al., 2017), not least due to its dismal prognosis and recent predictions that PDAC will rank as the second most common cause of cancer-related deaths in the Western world by 2030 (Rahib et al., 2014).

Exploitation of self-renewing human pluripotent stem cells (hPSCs) and subsequent multi-lineage differentiation has led to the development of pre-clinical *in vitro* pancreatic disease models (Hohwieler et al., 2019; Rowe and Daley, 2019). Pancreatic exocrine and endocrine cells develop from a common precursor, the pancreatic progenitor (PP) cell. Developmentally, tripotent PPs restrict their lineage potential to a tip domain, giving rise to the acinar lineage, and to a bipotent trunk domain, forming the ductal lineage together with subsequently delaminating endocrine cell types (Zhou et al., 2007; Schaffer et al., 2010). While advances in PP differentiation enabled rapid success in generating endocrine pancreatic cells and respective disease models, approaches to guide hPSCs into the exocrine pancreas remained sparse up to the recently generated exocrine pancreatic organoids (exoPOs) (Hohwieler et al., 2017; Huang et al., 2015; Simsek et al., 2016; Tulpule et al., 2013). The resulting exoPOs are, however, heterogeneous, containing immature acinar, ductal, and non-pancreatic cell types. Although exocrine pancreatic development is neither in mice nor in humans fully understood, the initial induction of a tip- or trunk-like domain may be of central importance for the successful *in vitro* derivation and the subsequent compartment-specific disease modeling of functional acinar or ductal cells from human PSCs.

PDACs can develop from both acini and ducts. While PDACs evolving from acinar cells frequently traverse pancreatic intraepithelial neoplasia (low-grade and high-grade PanIN), ductal cells appear more refractory to developing PanIN lesions, but instead rapidly progress to aggressive cancers (Ferreira et al., 2017; Lee et al., 2019). As an additional route of PDAC development, ductal cells can form cystic IPMN (intraductal papillary mucinous neoplasia) lesions, which can also further progress to PDAC (Patra et al., 2017). Such differences in the pathophysiology of PDAC cannot be explained solely by the affected cell type. Instead, various combinations of oncogenes and tumor suppressors contribute in a probably cellular context-specific manner to define plasticity and cancer progression in the pancreas (Reichert et al., 2016). Oncogenic *KRAS* mutations regulate diverse phenotypes in sporadic and inherited PDAC, leading to different routes of tumorigenesis permitted by the loss of distinct tumor suppressor genes (e.g., *TP53*, *CDKN2A*, *BRCA1/2*). A subset of ~10% of PDAC patients show an inheritable predisposition with mutations in the mentioned tumor suppressors also occurring in the germline (Roberts et al., 2016). Somatic *GNAS* (guanine nucleotide binding protein, alpha stimulating) mutations are more prevalent in IPMNs (Springer et al., 2015), and vice versa, post-zygotic, mosaic mutations can cause McCune-Albright syndrome (MAS) associated with an increased risk of developing IMPNs (Gaujoux et al., 2014; Wood et al., 2017).

To establish *in vitro*-generated pancreatic ductal organoids as a pathophysiological model, the organoid cultures should be (1) of high purity, (2) structurally and functionally comparable to *in vivo* ducts, (3) provide access to disease progression intermediate cell types, (4) reflect the mutation-triggered pathophysiology, (5) recapitulate germline features, and (6) provide access to arising mutation dynamics. Such a disease model would allow studying initiation and progression of pancreatic cancer as well as the mimicry of genetic predisposition syndromes. The present study establishes such a hPSC-based pancreatic ductal differentiation platform to model dysplasia and cancer progression in a genetically and cellularly defined background.

RESULTS

Engineering pancreatic duct-like organoids from human pluripotent stem cells

Our first goal was to develop a protocol giving rise to a homogeneous population of pancreatic duct-like organoids (PDLOs) from hPSCs by recapitulating pancreatic lineage commitment *in vitro*. We selected 30 compounds based on the literature and previous results (Hohwieler et al., 2017; Huang et al., 2015). Compounds were screened in a 2-phase protocol over 17 days on PPs derived from human embryonic stem cells (hESC, HUES8) (Figure 1A). Within the first phase, we aimed to mimic the segregation of trunk cells, presumed bipotent progenitors, expressing *SOX9* and *PDX1*. The simultaneous decrease in *PTF1A*, *NKX6-1*, *INS*, *GCG*, and *ALB* was assessed to ensure the suppression of a pancreatic tip/acinar domain as well as an endocrine or hepatic fate. The second phase was designed to allow pancreatic trunk-like organoids (PTrLOs) to develop a duct-like expression profile indicated by the upregulation of *KRT19* (Figure 1B). Tubulogenesis, a morphological event important for maturation *in vivo*, is mediated by epithelial stratification, acquisition of cell polarity, and microlumen formation (Villasenor et al., 2010; Kesavan et al., 2009). Accordingly, we aimed for a homogeneous culture of one-layered ring-like epithelial organoids (Figure 1B). In phase I, 7/20 tested compounds improved ductal differentiation based on marker expression and organoid morphology on day 30; in phase II, 4/28 fulfilled this requirement (Figures S1A–S1D). Exemplarily, nicotinamide was a prerequisite for the formation of ring-like organoids (Figure 1C). Fibroblast growth factor 10 (FGF10) and epidermal growth factor (EGF) caused a strong upregulation of the ductal marker *KRT19* (Figures 1D, 1E, and S1E), an observation previously reported in murine pancreatic explants (Rhodes et al., 2012). After EGF addition, we observed a tendency for higher PDLO formation capacity and proliferation rate, thereby significantly increasing PDLO size (Figures 1E and 1F). Zinc sulfate ($ZnSO_4$), in phase I+II, and keratinocyte growth factor (KGF) in phase I, supported ductal specification by upregulating *KRT19* and increasing culture homogeneity (Figures S1E–S1G). The putative NOTCH activator and WNT inhibitor MSC2530818 increased cystic fibrosis transmembrane conductance regulator (*CFTR)* expression at a concentration of 0.05 μM (Czodrowski et al., 2016; Fryer et al., 2004). At higher MSC2530818 concentrations, organoid morphology was disrupted (Figure 1G). RNA sequencing (RNA-

Please cite this article in press as: Breunig et al., Modeling plasticity and dysplasia of pancreatic ductal organoids derived from human pluripotent stem cells, Cell Stem Cell (2021), https://doi.org/10.1016/j.stem.2021.03.005

CellPress

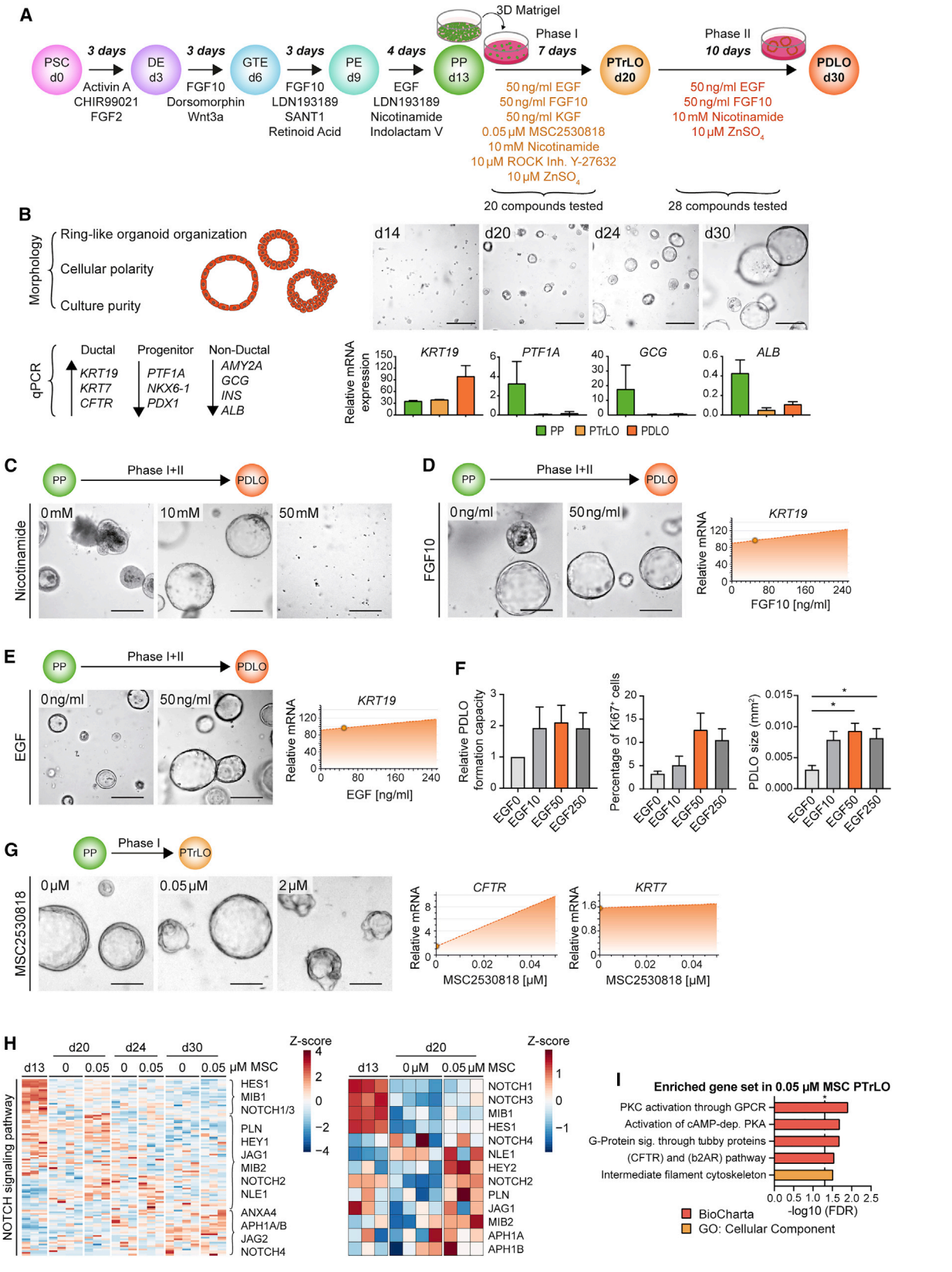

(legend on next page)

Please cite this article in press as: Breunig et al., Modeling plasticity and dysplasia of pancreatic ductal organoids derived from human pluripotent stem cells, Cell Stem Cell (2021), https://doi.org/10.1016/j.stem.2021.03.005

seq) analysis revealed a strongly dynamic expression pattern of NOTCH signaling genes during ductal differentiation, indicative of a phase-dependent role of different NOTCH mediators. The addition of MSC2530818 during phase I augmented the expression of respective NOTCH-associated genes that were activated at the expected trunk-like stage at day 20 (Figure 1H). In contrast, no clear inhibition of WNT target genes was found after MSC2530818 stimulation (Figure S1H), while, importantly, a CFTR-related gene set was enriched (Figure 1I). Thus, our final induction medium for PDLO generation consisted in phase I of KGF, MSC2530818, ROCK inhibitor, EGF, FGF10, nicotinamide, and $ZnSO_4$, and in phase II of EGF, FGF10, nicotinamide, and $ZnSO_4$ (Figure 1A).

PDLOs recapitulate cell-type-specific features

Next, we characterized the hESC-derived PDLOs for cell-type-specific markers and conducted functional assays. PDLOs homogeneously expressed duct-specific proteins (e.g., KRT19, E-CAD, SOX9, HNF1B) with corresponding gene expression patterns (Figures 2A–2C and S2A). While progenitor markers (NKX6-1, PDX1) decreased during ductal differentiation, non-ductal markers (e.g., GCG, C-pep, AMY2A) were absent (Figures 2B–2D and S2B–S2D). Conclusively, immunofluorescence (IF) analysis confirmed the formation of a polarized ductal epithelium with highly organized expression of E-CAD, KRT19, KRT8, and tight junction-associated proteins CLDN1, OCLN, and apical ZO-1 (Figures 2E and 2F). Complex structural organization was seen in both primary cilia staining (acTUB; Figure 2F) and transmission electron microscopy (microvilli margin, tight junctions; Figure 2G). Late ductal maturity markers (e.g., KRT7, CFTR) were present only in a subset of PDLOs (Figures 2E, 2F, and S2A).

To test PDLO functionality, we compared the activity of carbonic anhydrase (CA), a key enzyme expressed in pancreatic ducts to catalyze bicarbonate (HCO_3^-) production to PPs and PDAC organoids (Panc163) (Wilschanski and Novak, 2013). CA activity was significantly higher in PDLOs than in PPs, confirming the upregulation of CA2 during ductal maturation (Figure 2H). CFTR mediates HCO_3^- secretion and subsequent osmosis-mediated water influx into the ductal lumen (Dekkers et al., 2013). Accordingly, stimulation with forskolin (FSK) led to a significant swelling of PDLOs indicative of CFTR ion channel activity (Figure 2I). Ki-67 was stained to exclude differential proliferation as a cause for the increase in organoid size (Figure S2I). The measurement of intracellular pH with the fluorescent indicator BCECF-AM demonstrated comparable apical Cl^-/HCO_3^- exchange and basolateral Na^{2+}-dependent HCO_3^- uptake activities in PDLOs and adult human organ donor-derived pancreatic organoids (Figures 2J and 2K). To demonstrate the broad applicability of our protocol, we differentiated a control human induced PSC (hiPSC) line (co-iPSC) and the hESC line H1 into PDLOs. Both PDLO cultures showed comparable mRNA and protein marker expression to HUES8-derived PDLOs (Figures 2L, 2M, S2E, and S2F). The activity assays remained reproducible across multiple lines, which suggested the presence of functional CA enzyme and HCO_3^- secretion activity in all hPSC-derived PDLOs (Figures S2G–SI). Still, the protocol performed best in HUES8 cells, and further cell line tailored fine tuning will be necessary as described, for example, for PP differentiation (Nostro et al., 2015).

Global transcriptomic and proteomic analyses confirm ductal identity

To validate the specificity, maturity, and developmental trajectories of PDLOs, we analyzed time-resolved transcriptomes in comparison to non-transformed human pancreatic ductal organoid controls derived from a resection specimen. Stage-specific clustering of differentially regulated genes revealed a closer proximity of PDLOs to primary organoids than to PPs (Figure 3A). Accordingly, progenitor genes were gradually lost during differentiation, and duct-related genes (VI–VIII), including several claudins, annexins, and mucosal barrier-related genes (*MUC13*, *TFF1/2*), together with ion/water secretion-related genes such as *AQP3*, were upregulated (Figures 3B and 3C; Tables S1 and S2). The time-resolved dynamics of pancreatic ductal maturation and PP genes further validated the acquisition of a duct-like transcriptome in PDLOs, albeit the degree of maturation from primary adult ductal organoids could not be fully met (Figure 3C). Gene set enrichment analysis (GSEA) confirmed the loss of PP identity in PDLOs (Figure 3D; Gerrard et al., 2016; Xie et al., 2013). To probe the transient acquisition of a trunk-like domain upon differentiation, trunk-specific gene sets derived from $HES1^+$ $NGN3^-$ DBA^+ embryonic day (E)15.5 mouse pancreata (De Lichtenberg et al., 2018) and a single-cell RNA-seq (scRNA-seq) set from E15.5–E18.5 mice (Krentz et al., 2018) were used. The transcriptomes of day 20/24 organoids were enriched for trunk-specific genes (Figure 3E), and trunk-specific markers such as *ID2*, *ST3GAL6*, or *CXCL12* peaked at those time points (clusters IV and V; Figure 3B; Table S1; Methods

Figure 1. Engineering pancreatic duct-like organoids (PDLOs) from human pluripotent stem cells (hPSCs)

(A) Schematic overview of the 2-phase screening approach. DE, definitive endoderm; GTE, gut tube endoderm; PE, pancreatic endoderm; PTrLO, pancreatic trunk-like organoid.

(B) Left: morphological criteria and marker for evaluation of duct formation. Right: bright-field (BF) images and marker profiles obtained from PP, PTrLOs, and PDLOs during differentiation; day (d).

(C–E and G) BF images and dynamic marker profiles of PDLOs/PTrLOs. Compounds and screening phase as indicated. Dynamic marker profiles were interpolated from qPCR data using MODDE software, and small circles indicate the applied concentration of the protocol version at the time point of testing. (C) Nicotinamide, (D) FGF10, (E) EGF, and (G) MSC2530818 titration.

(F) Titration of EGF concentration in PDLO medium (0–250 ng/ml) and its effect on organoid growth characteristics (means ± SEMs; n = 3; in duplicate, ordinary 1-way ANOVA followed by Tukey's multiple comparison test).

(H and I) RNA-seq analysis of PPs, PTrLOs, and PDLOs with or without 0.05 μM MSC2530818 during phase I (0.00 μM: n = 4, 0.05 μM: n = 3).

(H) Left: plotting all identified genes from the GO term "NOTCH signaling pathway" (GO: 0007219) over time. Right: selection of genes at PP and PTrLO stages.

(I) RNA-seq overrepresentation analysis of PTrLOs (day 20) with 0.05 μM MSC2530818 treatment against PTrLOs (day 20) without MSC. Scale bars: 100 μm. PDLO cultures were analyzed at day 30, if not stated otherwise.

(C)–(E) and (G) show data from 1 representative experiment in duplicate.

Please cite this article in press as: Breunig et al., Modeling plasticity and dysplasia of pancreatic ductal organoids derived from human pluripotent stem cells, Cell Stem Cell (2021), https://doi.org/10.1016/j.stem.2021.03.005

CellPress

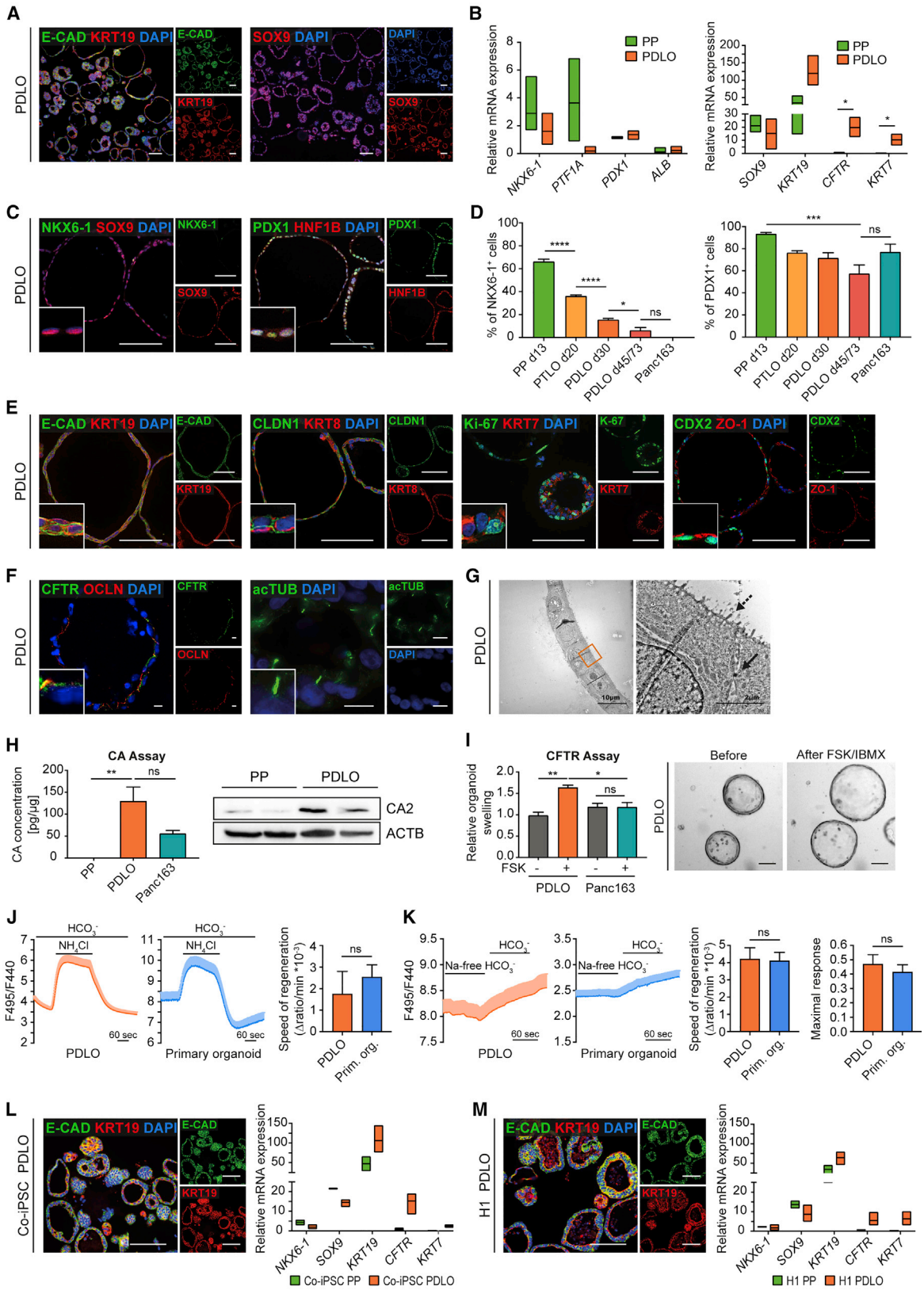

(legend on next page)

Please cite this article in press as: Breunig et al., Modeling plasticity and dysplasia of pancreatic ductal organoids derived from human pluripotent stem cells, Cell Stem Cell (2021), https://doi.org/10.1016/j.stem.2021.03.005

S5). Likewise, a ductal program was already initiated in PTrLOs, as suggested by the upregulation of ductal markers such as *SCTR* and *CFTR*. At day 30, PDLOs were significantly enriched for ductal gene sets from two scRNA-seq studies (Baron et al., 2016; Enge et al., 2017; Figure 3F). A recently developed cell population-mapping algorithm for cell-type deconvolution (Frishberg et al., 2019) was additionally applied and assigned PDLOs among the different pancreatic cell types closest to ductal cells (Figure S3A). Furthermore, GSEA from the hallmark database and Gene Ontology (GO) term analysis indicated an acquisition of maturity in PDLOs, as proliferative and early developmental terms were depleted in exchange with enriched metabolic terms (Figures S3B–S3D).

Two studies indicate that *in vivo* ductal cells may be either predominantly important for water secretion to allow the flow of zymogens (expression of CFTR) or specialized to protect pancreatic tissue against digestive enzymes in the pancreatic juice (expression of MUC1) (Burghardt et al., 2003; Baron et al., 2016). PDLO transcriptomes were only enriched for a *MUC1*$^{+}$ signature, indicating the formation of ductal subpopulations *in vitro* (Figure 3G). Similarly, Qadir et al. (2020) identified five ductal subpopulations, from which four were enriched in PDLOs (Figure S3E). GO terms for keratinocyte differentiation and receptors for advanced glycation end product (RAGE) receptor binding, possibly linked to mucin production (Xiong et al., 2017), were enriched at later PDLO stages, supporting a MUC1-dominant subtype (Figure S3F).

To validate transcriptomic data, we measured the global proteomes of hPSC-derived PPs and PDLOs at the endpoint of differentiation, with >6,000 proteins detected in both samples (Figure 3H). The analysis revealed an overall high correlation of protein and RNA levels (Figures 3I and S3H), mirrored by an upregulation of ductal maturity proteins (e.g., MUC1/13, TFF2) in PDLOs (Figures 3J and 3K; Table S3). Increased protein expression of all detected members of the oxidative phosphorylation complex in PDLOs (Figure 3L) further suggests an increased metabolic turnover. In addition to similar GO term enrichment/depletion patterns in transcriptomes and proteomes (Figures 3M, S3B, S3I, and S3J), terms such as retinoic acid signaling, EGF receptor (EGFR) signaling, and pancreatic secretion were enriched in PDLOs at the protein level (Figures 3M and 3N). These terms were previously assigned to primary ductal organoids (Figure S3G) and further support the maturity of PDLOs.

Development of human duct-like tissue after xenotransplantation of PDLOs

Transplantation of *in vitro* differentiated cells into a suitable host site can support further maturation by mimicking a physiological niche (Rezania et al., 2012). To test this, we transplanted PDLOs or three-dimensional (3D)-aggregated PPs into the anterior chamber of the mouse eye (ACE) (Figures 4A and S4A), as previously described (Cohrs et al., 2020). Tripotent PPs mainly formed compact structures *in vivo* containing all pancreatic lineages, mainly chymotrypsin C-positive (CTRC^{+}) acinar, but also ductal and endocrine (GCG, C-pep) cells (Figures 4B–4D). In contrast, PDLO grafts formed complex ring-like structures (Figures 4B and 4C) that expressed the ductal markers KRT7, KRT8, and KRT19 (Figure 4D). PDLO *in vivo* imaging allowed us to monitor engraftment on the iris, subsequent lumen formation, and emergence of large duct-like tissue likely supported by vascularization (Figures S4B and S4C).

While kidney capsule transplantation is commonly used for endocrine engraftments (Hogrebe et al., 2020; Rezania et al., 2012), we and others have shown that the pancreatic niche is particularly suitable for exocrine engraftments (Hohwieler et al., 2017; Georgakopoulos et al., 2020). Orthotopic PDLO transplantation into immunocompromised mice led to the formation of tubularly organized structures, as demonstrated by consecutive sections (Figure 4E). The human tissue (identified by H-NUCL staining) within the transplantation site homogeneously expressed the ductal markers KRT8, KRT19, E-CAD, CLDN1, and SOX9 (Figures 4E and 4F). In agreement with the *in vitro* transcriptomic analysis, the majority of PDLOs *in vivo* developed duct-like tissue expressing MUC1 (Figures 4E and 4F). MUC1^{-} duct-like tissue revealed in selected grafts CFTR expression, emphasizing the potential of our protocol to generate distinct

Figure 2. PDLOs recapitulate cell-type-specific features

(A) Representative overview IF images of HUES8-derived PDLOs.

(B) Downregulation of PP and upregulation of ductal markers in PDLOs in qPCR experiments (PTF1A, PDX1, KRT7, CFTR: n = 3; NKX6-1, ALB, SOX9, KRT19: n = 6; in duplicate).

(C) Representative IF images of individual PDLOs.

(D) Time-resolved downregulation of PP markers measured by flow cytometry (FC) in comparison with patient-derived human PDAC organoids (Panc163) (n = 4; days 45/73: n = 3; Panc163: n = 2; in duplicate).

(E) IF images of PDLOs stained for ductal, epithelial, proliferation, and polarity markers.

(F) IF staining for CFTR, tight junction protein Occludin (OCLN), and primary cilia (acTUB, acetylated tubulin). Scale bar: 10 μm.

(G) Transmission electron microscopy images of a PDLO. Arrow marks a desmosome; dashed arrow marks microvilli.

(H) Carbonic anhydrase (CA) activity assay (n = 3; in duplicate, 3 blinded measurements for each replicate). Right: higher CA2 level in PDLOs than in PPs on western blot (WB) (n = 2; in duplicate).

(I) PDLO swelling within the CFTR assay upon stimulation with 20 μM forskolin (FSK) and 100 μM isobutylmethylxanthine (IBMX) for 18 h (n = 3; in duplicate). Right: BF images of PDLOs (day 44/45).

(J and K) Confirmation of the functional similarity in ion secretion of PDLOs and adult primary tissue-derived ductal organoids by intracellular pH measurement.

(J) Apical Cl^{-}/HCO_3^{-} exchange activity (PDLOs: n = 28; primary organoids: n = 12) (Maléth et al., 2015).

(K) Basolateral Na^{+}-dependent HCO_3^{-} uptake (PDLOs: n = 15; primary organoids: n = 13; n = number of organoids) (Molnár et al., 2020) were estimated (means ± SEMs; analysis of variance/Mann-Whitney test).

(L and M) IF images of KRT19 and E-CAD in PDLOs derived from Co-iPSCs or H1 together with progenitor and ductal mRNA marker expression (n = 3; in duplicate). Scale bars: 100 μm, if not stated otherwise. Insets in the corners are 4× enlarged. PDLOs represent day 30 of the protocol.

(B), (L), and (M) Floating bars spanning minimal and maximal values; multiple t tests via the Holm-Sidak method; only significant comparisons are depicted. (D), (H), and (I) Means ± SEMs; ordinary 1-way ANOVA followed by Tukey's multiple comparison test.

Please cite this article in press as: Breunig et al., Modeling plasticity and dysplasia of pancreatic ductal organoids derived from human pluripotent stem cells, Cell Stem Cell (2021), https://doi.org/10.1016/j.stem.2021.03.005

CellPress

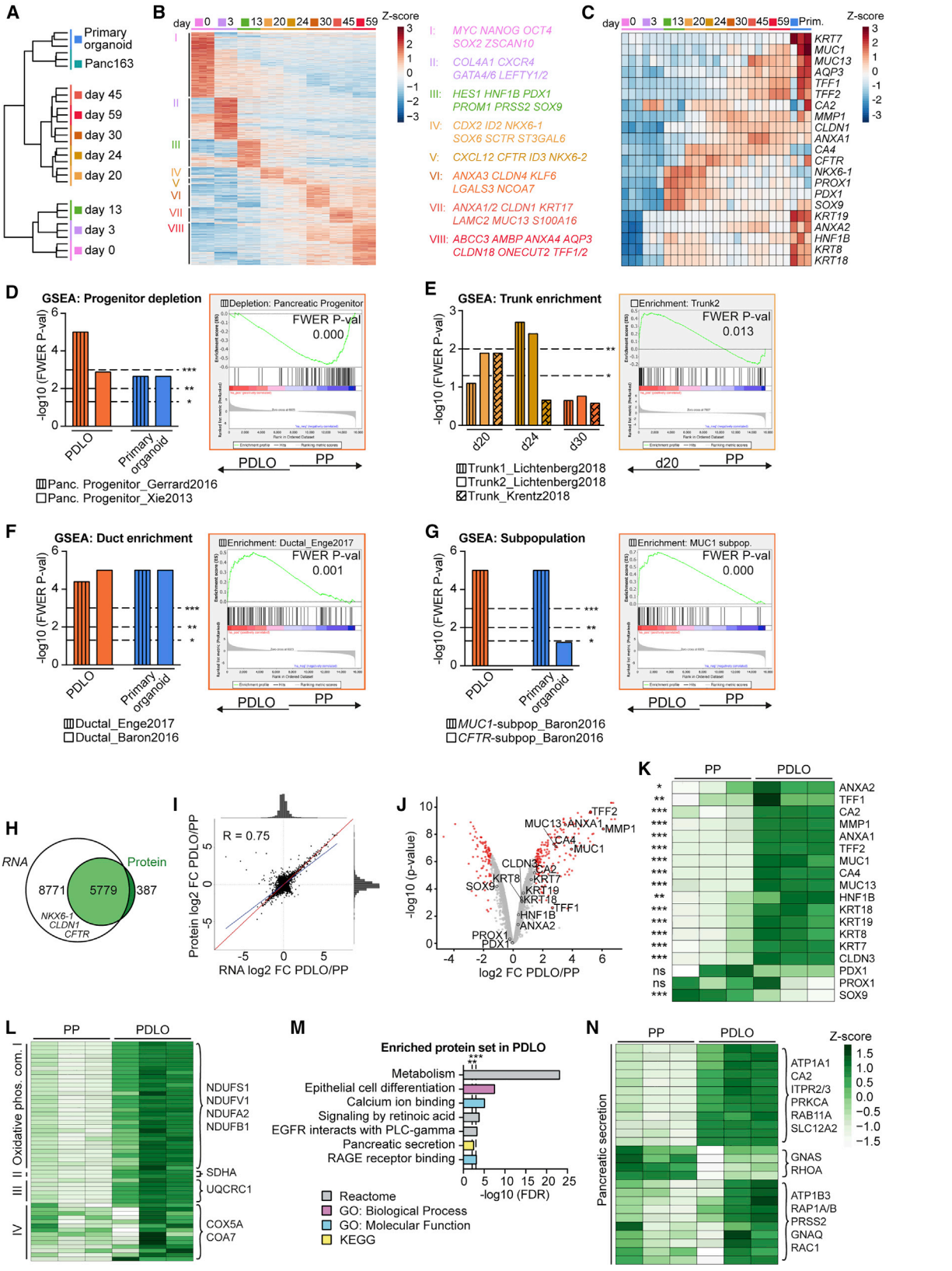

(legend on next page)

Please cite this article in press as: Breunig et al., Modeling plasticity and dysplasia of pancreatic ductal organoids derived from human pluripotent stem cells, Cell Stem Cell (2021), https://doi.org/10.1016/j.stem.2021.03.005

ductal subpopulations of the pancreas (Figure S4D). Besides tubular organization of the graft and homogeneous MUC1 or CFTR expression, maturation upon transplantation was observed via the downregulation of Ki-67, PDX1, and CDX2. Dysplasia-indicating proteins were absent and respective checkpoints remained intact (Figures 4F and 4G). To validate marker expression, healthy human pancreatic tissue was stained with the same antibodies, further corroborating our results (Figure S4E).

KRAS^{G12D} expression induces lumen-filling and EMT in PDLOs

To establish PDLOs as a potential model for dysplasia and cancer, we investigated whether oncogenic *KRAS* or *CDKN2A* loss evoked specific phenotypes *in vitro*. For this, we used *piggyBac* transposon-based vectors (Kim et al., 2016) to conditionally express mutant KRAS^{G12D} and CRISPR/Cas9 to knock out *CDKN2A* in HUES8 cells (Figures 5A, S5A, and S5B). All of the engineered cell lines efficiently formed PPs and PDLOs, and expression of the hemagglutinin (HA)-tagged KRAS^{G12D} construct was dose-dependently induced by doxycycline (Dox) (Figure S5C). Pull-down assays of active KRAS and increased expression of phosphorylated ERK (pERK) levels validated KRAS^{G12D} activity (Figures S5D and S5E). Expression of KRAS^{G12D} in PDLOs of CDKN2A-deficient or -proficient background caused a lumen-filling and size reduction in PDLOs (Figures 5B and S5F). KRAS^{G12D} induction significantly reduced proliferation depending on the Dox dosage as assessed by Ki-67 staining and cell-cycle analysis (Figures 5C, 5D, S5G, and S5H).

One explanation of the growth reduction could be oncogenic KRAS-provoked replication stress (Di Micco et al., 2006). KRAS^{G12D}-induced cells upregulated the phosphorylated histone variant H2AX (γH2AX), which is indicative of DNA damage foci (Zeman and Cimprich, 2014; Figure 5E). Checkpoints limiting cell growth in response to DNA damage and replicative stress can contribute to cancer protection (Bartek et al., 2007). Accordingly, we observed a KRAS^{G12D}-driven induction of P16 on the CDKN2A-proficient background, while P21 was particularly upregulated in Dox-treated CDKN2A$^{KO/KO}$ PDLOs (Figures 5F, 5G, and S5I). This suggests a functional P21 checkpoint to induce cell-cycle arrest even in the absence of P16 (Takeuchi et al., 2010). Upregulation of the nuclear factor κB (NF-κB) subunit *RELA* in CDKN2A-deficient PDLOs after KRAS^{G12D} induction supports this hypothesis (Figure 5H), as RELA can operate as a mediator of oncogene-induced senescence (OIS) (Lesina et al., 2016). As an additional putative mechanism of cell-cycle inhibition in CDKN2A$^{KO/KO}$ cells, we detected increased levels of P15 (CDKN2B) after KRAS^{G12D} induction, which can replace P16 to inhibit CDK4/6, thus preventing the inactivation of retinoblastoma protein (RB), a major G1/S checkpoint regulator (Tu et al., 2018; Kuilman et al., 2008; Figures 5G, S5I, and S5J). KRAS^{G12D} expression reduced phosphorylated RB (pRB) levels (Figures 5G and S5J), while active (not hyperphosphorylated) RB prevents cells from entering S phase. We conclude that ablation of P16 alone was not sufficient to prevent KRAS-induced cell-cycle arrest in PDLOs. These observations pointed toward OIS culminating in a tendency for increased senescence-associated β-galactosidase activity upon KRAS^{G12D} induction, independent of the genetic CDKN2A status (Figure 5I). Furthermore, the pro-apoptotic marker *BAX* was upregulated in CDKN2A$^{KO/KO}$ PDLOs, as was cleaved poly (ADP-ribose) polymerase (PARP) after KRAS^{G12D} induction (Figures S5K and S5L). Intriguingly, senescence and apoptosis can operate as a tumorigenic roadblock in pre-neoplastic lesions (Lee and Schmitt, 2019). Epithelial-to-mesenchymal transition (EMT) has been described to potentially bypass such roadblocks during carcinogenesis (Ansieau et al., 2008; Song and Shi, 2018). Therefore, we analyzed EMT-related markers, revealing differential and KRAS^{G12D} dose-dependent upregulation in the PDLO system on mRNA and protein level (Figures 5J–5L and S5M–S5P). Furthermore, cellular changes resembling the EMT-like character were detected by real-time imaging of CDKN2A$^{KO/KO}$ KRAS^{G12D} PDLOs, including the outgrowth of single spindle-shaped cells from PDLOs, followed by cell flattening of migrating cells (Figure 5M; Videos S1 and S2). Since a reduction of the E-CAD protein level could not be observed (Figures 5K and S5N–S5P), we assume that the transcriptional and phenotypic pattern displays a partially initiated EMT program (Grigore et al., 2016; Aiello et al., 2018).

MAS-derived and GNAS^{R201H}-overexpressing PDLOs form large cysts

Somatic activating *GNAS* mutations, most frequently p.R201C or p.R201H, are major drivers of dysplastic growth in IPMNs (Tan et al., 2015; Wu et al., 2011). Postzygotic mosaic *GNAS* mutations cause fibrous dysplasia (FD), a rare disorder characterized by abnormal bone. MAS is associated with FD, café-au-lait macules, and endocrinopathies. Notably, several studies

Figure 3. Global transcriptomic and proteomic analyses confirm ductal identity

(A) Global RNA-seq data during PDLO differentiation and of patient-derived human ductal organoids (Prim.) (n = 3). Ward clustering was performed with all of the processed genes.

(B) Heatmap of stage-specific significant genes.

(C) Temporally resolved heatmap of key progenitor and ductal genes.

(D–G) Gene set enrichment analysis (GSEA) of day 20, day 24, PDLOs (day 30), and primary ductal organoids against PPs (day 13) for distinct reference gene sets. Exemplary GSEA plots are highlighted in respective sample colors.

(H) Venn diagram representing the overlap of transcripts measured by RNA-seq with proteins detected by mass spectrometry (n = 3).

(I) Pearson correlation of RNA-seq and proteome $\log_2$ fold change of PDLOs (day 59) versus PPs (day 13). The blue line indicates actual correlation, the red line indicates ideal correlation of all 5,779 shared genes/proteins.

(J) Volcano plot of protein mass spectrometry data of PDLOs and PPs. Differentially regulated proteins in red ($P \leq 0.01$ and fold change $\geq |1.5|$).

(K) Heatmap of key progenitor and ductal proteins in PPs and PDLOs.

(L and N) Heatmap illustration of proteins (L) from the four "oxidative phosphorylation" complexes and (N) the Kyoto Encyclopedia of Genes and Genomes (KEGG) term "Pancreatic Secretion."

(M) Enriched protein sets in PDLOs over PPs.

Please cite this article in press as: Breunig et al., Modeling plasticity and dysplasia of pancreatic ductal organoids derived from human pluripotent stem cells, Cell Stem Cell (2021), https://doi.org/10.1016/j.stem.2021.03.005

CellPress

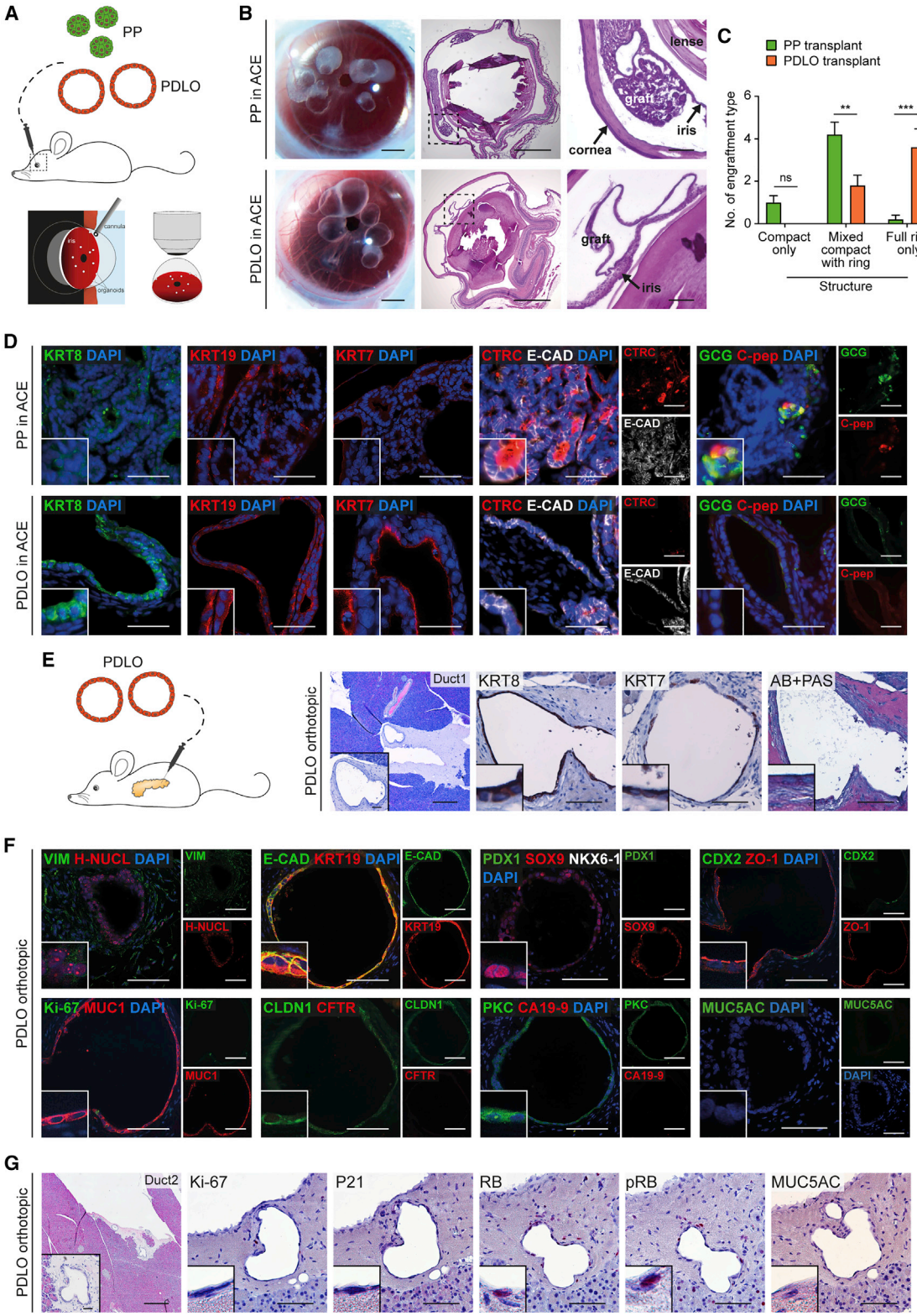

Figure 4. Development of human duct-like tissue after xenotransplantation of PDLOs

(A) Scheme of transplantation into the anterior chamber of the mouse eye (ACE).

(B) Growth of grafted organoids on the iris 5 weeks after transplantation. Left panel: image of eyes transplanted with PPs or PDLOs. Right panels: H&E staining of sagittal section of explanted eyes with PDLO graft on the iris.

(legend continued on next page)

Please cite this article in press as: Breunig et al., Modeling plasticity and dysplasia of pancreatic ductal organoids derived from human pluripotent stem cells, Cell Stem Cell (2021), https://doi.org/10.1016/j.stem.2021.03.005

report pancreatic cysts in MAS patients accompanied by an increased PDAC risk (Robinson et al., 2018; Wood et al., 2017). To derive an *in vitro* model to explore disease pathogenesis driven by *GNAS* mutations, a genetically mosaic culture of MAS-patient bone marrow stromal cells was reprogrammed to generate clonal isogenic iPSC lines with either heterozygous p.R201C or wild-type (WT) *GNAS* genotype (Figures 6A, 6B, and S6A). MAS-iPSC lines were pluripotent and efficiently differentiated into PPs and PDLOs, irrespective of their *GNAS* status (Figures 6C–6F and S6B–S6D). While $GNAS^{WT/WT}$ PDLOs resembled PDLOs derived from WT hESCs, $GNAS^{WT/R201C}$ MAS-iPSCs formed large cystic PDLOs (Figures 6D, 6E, and S6D). Cystic growth can be explained by the increased proliferation of $GNAS^{WT/R201C}$ cells in the PDLOs, indicated by Ki-67 expression and flow cytometry-based quantification of 5-ethynyl-2′-deoxyuridine (EdU) incorporation (Figures 6F and S6E). Next, we investigated downstream effectors of the *GNAS*-encoded protein $G_{\alpha s}$, which mediates cyclic AMP (cAMP) generation via the adenylyl cyclase. *GNAS* mutations lead to a constitutively active signaling axis upon the stabilization of guanosine triphosphate (GTP)-bound $G_{\alpha s}$ (Rosenbaum et al., 2009). Consistently, intracellular cAMP levels were elevated in both $GNAS^{WT/R201C}$ iPSCs and PDLOs (Figure 6G). In line with this, $GNAS^{WT/R201C}$ PDLOs displayed hyperactive protein kinase A (PKA) signaling shown by the phosphorylation of target proteins, including vasodilator-stimulated phosphoprotein (VASP). Inhibition of PKA reduced cyst size (Figures 6H and 6I). Of note, sustained PKA activation was reported to mediate $G_{\alpha s}$ signaling in the context of cystic pancreas tumorigenesis in mice (Patra et al., 2018).

To confirm the results from MAS-iPSCs, we engineered hESCs with the inducible GNAS variant (p.R201H) using the *piggyBac* system (Figure 6J). The overexpression of $GNAS^{R201H}$ within hESC-derived PDLOs led to cystic growth and cAMP-PKA-VASP signaling (Figures 6K, 6L, and S6F–S6H), which recapitulated MAS patient data. Thus, we present a patient-specific and an engineered *in vitro* model for activating GNAS mutations in human ductal organoids to study this oncogene as a driver of pancreatic cyst growth in humans.

Mutation-dependent heterogeneity of $KRAS^{G12D}$-driven PDAC formation in PDLO grafts

To corroborate *in vitro* PDLO alterations in xenograft experiments, we orthotopically transplanted 51 mice with the previously described transgenic PDLOs. We induced $KRAS^{G12D}$ alone or in genetic covariance of CDKN2A loss ($CDKN2A^{KO/KO}$) as well as $GNAS^{R201H}$ over 8 weeks *in vivo* (Figures 7A, 7G, and S7A). The average engraftment rate across all of the genotypes was ~75%, with the highest rates (100%) in $CDKN2A^{KO/KO}$ PDLOs. The reporter (HA-tag, mCherry) signal of PDLO cells was robustly detected in the grafts (Figure S7A). Notably, the four PDLO grafts arising from $KRAS^{G12D}$ PDLOs showed a substantial degree of dysplastic heterogeneity, resulting in one small glandular PDAC-like lesion forming a tumor mass with cells invading the murine host (PDAC 1). The second and third engraftments resembled high-grade preneoplastic lesions, smaller in size as PDAC 1, without invasion in the murine host (Figure 7B, upper row), but with very strong MUC5AC and CA19-9 expression (Figure S7A, staining not shown). A fourth graft showed only moderate signs of dysplasia in line with less CA19-9 and MUC5AC expression (data not shown). In contrast to the heterogeneous dysplastic lesions in $KRAS^{G12D}$ grafts, all of the $CDKN2A^{KO/KO}$ $KRAS^{G12D}$ PDLO grafts with robust transgene expression formed large, dedifferentiated, polymorphic PDAC-like lesions and invaded the mouse host (Figures 7B, lower row, and S7A). All $KRAS^{G12D}$ grafts homogeneously expressed epithelial (e.g., KRT19) and partially mesenchymal markers (N-CAD, VIM) (Figures 7C, upper row, and S7B, upper row). To contrast, only a few single tumor cells retained an epithelial phenotype in $CDKN2A^{KO/KO}$ $KRAS^{G12D}$ tumors. Here, most of the tumor cells acquired a mesenchymal marker pattern when compared with $CDKN2A^{KO/KO}$ engraftments from the same organoid preparation lacking $KRAS^{G12D}$ induction (Figure 7C, lower row, and Figure S7B, lower row; compare to Figure S7C). To directly link $KRAS^{G12D}$ dosage with EMT in the $CDKN2A^{KO/KO}$ genotype, we focused our analysis on areas with heterogeneous $KRAS^{G12D}$ induction. We observed the spatial concordance of HA-tag expression and the occurrence of putative disseminating cells from the ductal epithelial layer expressing mesenchymal markers (Figure 7D). Notably, the $CDKN2A^{KO/KO}$ grafts formed well-differentiated pancreatic ducts with moderately increased proliferation compared to WT ducts (Figure S7C, compare to Figure 4G and Figure S7A). Likewise, we found signs of cellular atypia and dysplasia accompanied by the PDAC markers MUC5AC and/or CA19-9 in 3 of 6 grafts without additional KRAS induction (Figures S7A and S7C).

Oncogenic roadblocks are released in PDLO grafts

Next, we dissected the cell-cycle roadblocks upon *in vivo* tumor formation in $KRAS^{G12D}$-driven tumorigenesis on a CDKN2A-proficient or -deficient background. Histopathological alterations and strongly increased proliferation in $KRAS^{G12D}$ plus $CDKN2A^{KO/KO}$ were accompanied by attenuated P53 expression and an almost complete absence of $P21^{+}$ cells (Figures 7E, lower row, and S7A). Similarly, the RB checkpoint was overcome either through increased phosphorylation of RB, indicative

(C) Quantification of observed engraftment types (means ± SEMs; n = 5 mice per group; ordinary 2-way ANOVA with Sidak's multiple comparison test).
(D) IF staining of PP-derived grafts revealed acinar, ductal, and endocrine cells in the ACE, while marker expression of PDLO-derived grafts was restricted to the ductal pancreatic lineage. CTRC, chymotrypsin C; C-pep, C-peptide.
(E) Orthotopic transplantation scheme and H&E/immunohistochemistry (IHC) images demonstrating engraftment site 8 weeks after transplantation (n = 5 mice).
(F) PDLO transplants expressed ductal epithelium-specific proteins MUC1, E-CAD, KRT19, and CLDN1, lost transcription factors PDX1 and CDX2, but lacked CFTR and CA19-9 expression.
(G) WT PDLO transplant stained for proliferation- and cell-cycle-related proteins and the dysplastic marker MUC5AC. pRB, phosphorylated RB; RB, retinoblastoma protein.
(B) and (E–G) Scale bars: 100 μm. Insets in the corners are 4× enlarged. Except in overview staining, here, scale bars: 500 μm, and 50 μm in insets. (D) Scale bar: 50 μm, insets are 2× enlarged.

Please cite this article in press as: Breunig et al., Modeling plasticity and dysplasia of pancreatic ductal organoids derived from human pluripotent stem cells, Cell Stem Cell (2021), https://doi.org/10.1016/j.stem.2021.03.005

CellPress

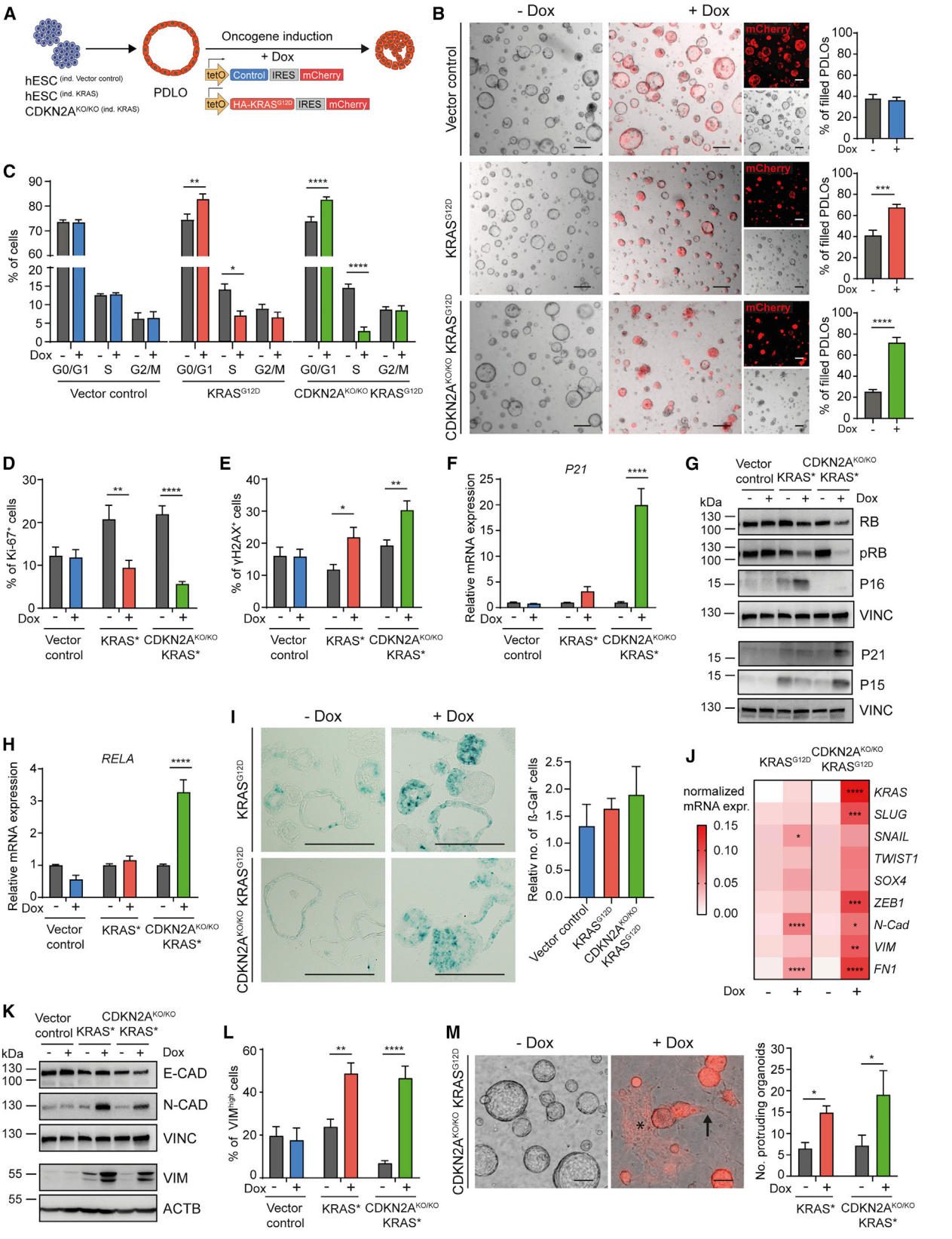

(legend on next page)

Please cite this article in press as: Breunig et al., Modeling plasticity and dysplasia of pancreatic ductal organoids derived from human pluripotent stem cells, Cell Stem Cell (2021), https://doi.org/10.1016/j.stem.2021.03.005

of its inactivation, or directly through the reduced expression of RB (Figures 7E, lower row, and S7D, lower row). To interrelate checkpoint loss with structural aberrations, we performed low-coverage whole-genome sequencing (lcWGS) of two $KRAS^{G12D}$ $CDKN2A^{KO/KO}$ tumors (PDAC I and III), but neither of them demonstrated substantial chromosomal rearrangements, indicating low strains in this genotype to overcome the threshold of cancerous growth (Figure 7F, lower panel; Table S4). Accordingly, panel sequencing of PDAC II identified a $P53^{S94P}$ mutation with a variant allele frequency of 25% among other single-nucleotide variants (SNVs) (Figure S7E; Table S5).

In contrast, only $KRAS^{G12D}$-induced tumors with an intact CDKN2A/P16 checkpoint revealed a higher intra- and inter-tumoral heterogeneity than their CDKN2A-deficient counterparts, mirrored also in various degrees of proliferation (Figures 7E, upper row, and S7D, upper row). While P21 was expressed in only a few cells of PDAC 1, the RB/pRB checkpoint appeared intact (Figure 7E, upper row). Similarly, an intact RB and P53/P21 checkpoint correlated with the lack of proliferation in regions of high-grade lesion 1 where increased tissue dysplasia was observed (Figure S7D, dashed arrows in upper row). lcWGS from $KRAS^{G12D}$-driven PDAC 1 graft revealed broader chromosomal rearrangements than in the $KRAS^{G12D}$ $CDKN2A^{KO/KO}$ tumors (Figure 7F; Table S4). Interestingly, displayed copy-number variants (CNVs) in this tumor included previously reported regions of recurrent alterations such as arm-level gains of chromosomes 1, 6, 12, and 20 (Shain et al., 2012; Notta et al., 2016). To conclude, despite the possibility of tumor formation from $KRAS^{G12D}$ induction only, CDKN2A operated as a roadblock to pancreatic ductal dysplasia and proliferation, and, in concert with $KRAS^{G12D}$, to EMT.

PDLOs expressing mutant GNAS can form IPMN-like lesions *in vivo*

Finally, we assessed the *in vivo* growth pattern of PDLOs exhibiting the inducible $GNAS^{R201H}$ expression cassette (Figure 7G). $GNAS^{R201H}$ PDLO engraftment occurred in 70% of the animals, independent of Dox induction. In 8/9 $GNAS^{R201H}$ PDLO engraftments, we detected the mCherry reporter (Figure S7A), from which 6 formed well-differentiated cystic ducts resembling human IPMNs with low-grade cellular atypia and tissue dysplasia (Figures 7G–7J, S7A, and S7F). In line with our *in vitro* data, such $GNAS^{R201H}$ grafts showed moderate proliferation (Figures 7I, S7A, and S7F), leading to branched structures with a variable degree of MUC1, MUC5AC, and CA19-9 expression (Figures 7J, S7A, and S7F). The expression of MUC1 and MUC5AC, without detection of MUC2 (data not shown), indicated a pancreatobiliary or gastric IPMN-like type (Furukawa et al., 2005; Klausen et al., 2019).

DISCUSSION

We establish a scalable PDLO differentiation tool to model pancreatic dysplasia *in vitro* and pancreatic cancer development upon transplantation *in vivo*. In contrast to the available cancer models derived from mice or fully developed PDAC tissue, PDLOs provide a defined and untransformed human genetic background with access to developmental intermediates. Complemented by gene editing, PDLOs enable studying the impact of specific genetic mutations as the starting point of dysplasia and cancer formation from a ductal origin.

Homogeneous cell fate commitment from the PP stage to ductal cells was validated by comprehensive tests, including ultrastructural and functional analyses. Temporally resolved RNA-seq complemented by mass spectrometry-based proteomics completed our in-depth characterization of PDLOs. Importantly, the PP signature was mainly lost in exchange with a ductal identity during differentiation, a hallmark segregating our PDLOs from previous progenitor or mixed exocrine organoids. In addition, PDLO transplantation into distinct *in vivo* niches such as the ACE and the pancreas allowed the formation of more complex organized ductal structures. Transplantation studies using the ACE as a niche for ductal pancreatic tissue could enable the longitudinal tracking of early human dysplasia and carcinogenesis in a living organism.

To establish PDLOs as a disease model, we asked whether common PDAC driver mutations induce an *in vitro* phenotype and distinguishable cancer types within an *in vivo*

Figure 5. $KRAS^{G12D}$ expression induces lumen-filling and EMT in PDLOs

(A) Timed induction of a *piggyBac* $KRAS^{G12D}$ transposon construct in engineered HUES8.

(B) BF PDLO images after induction of the vector control in $CDKN2A^{WT/WT}$ cells or the $KRAS^{G12D}$ expression cassette in $CDKN2A^{WT/WT}$ and $CDKN2A^{KO/KO}$ cells. Formation of lumen-filled PDLOs was quantified (n = 3; in triplicate). Scale bar: 200 μm.

(C) Cell-cycle analysis in PDLOs ± Dox (n = 3; in duplicate).

(D and E) FC quantification of proliferation marker Ki-67 and DNA-damage marker γH2AX (n = 3; in duplicate).

(F) qPCR analysis of *P21* (n = 3; in duplicate).

(G) Genotype-dependent differential regulation of cell-cycle regulators and checkpoint proteins. See Figures S5I and S5J for respective quantification of WB analysis.

(H) qPCR analysis of senescence marker *RELA* (n = 3; in duplicate).

(I) Histological sections of PDLOs stained for senescence-associated β-galactosidase activity (dark cyan color) and respective quantification (vector control, $CDKN2A^{KO/KO}$ $KRAS^{G12D}$ n = 3; $KRAS^{G12D}$ n = 5).

(J) Marker panel revealing increased EMT on mRNA level (n = 3; in duplicate).

(K) Regulation of EMT-related proteins after oncogene induction. E-CAD and N-CAD were detected on the same membrane as RB, pRB, and P16 in (G), therefore the same loading control (VINC) is shown. See Figure S5O for respective quantification.

(L) FC analysis of PDLO cells with high VIM expression (vector control, $CDKN2A^{KO/KO}$ $KRAS^{G12D}$ n = 4; $KRAS^{G12D}$ n = 3; in duplicate).

(M) BF PDLO images reveal how cells adopt morphological features of EMT in response to KRAS activation. Arrow: single cells disseminating from a PDLO, asterisk: area of mesenchymal-like cells (red, mCherry). Right: phenotype quantification (n = 4; in duplicate). Refer to Videos S1 and S2 for respective live-cell imaging. All of the data were acquired in PDLOs at day 38, 9 days after Dox induction. Scale bar: 100 μm, if not stated otherwise.

All panels: means ± SEMs; only significant comparisons are depicted. (B–F), (H), (J), (L), and (M): ordinary 2-way ANOVA with Sidak's multiple comparison test. (I) Ordinary 1-way ANOVA with Tukey's multiple comparison test.

Please cite this article in press as: Breunig et al., Modeling plasticity and dysplasia of pancreatic ductal organoids derived from human pluripotent stem cells, Cell Stem Cell (2021), https://doi.org/10.1016/j.stem.2021.03.005

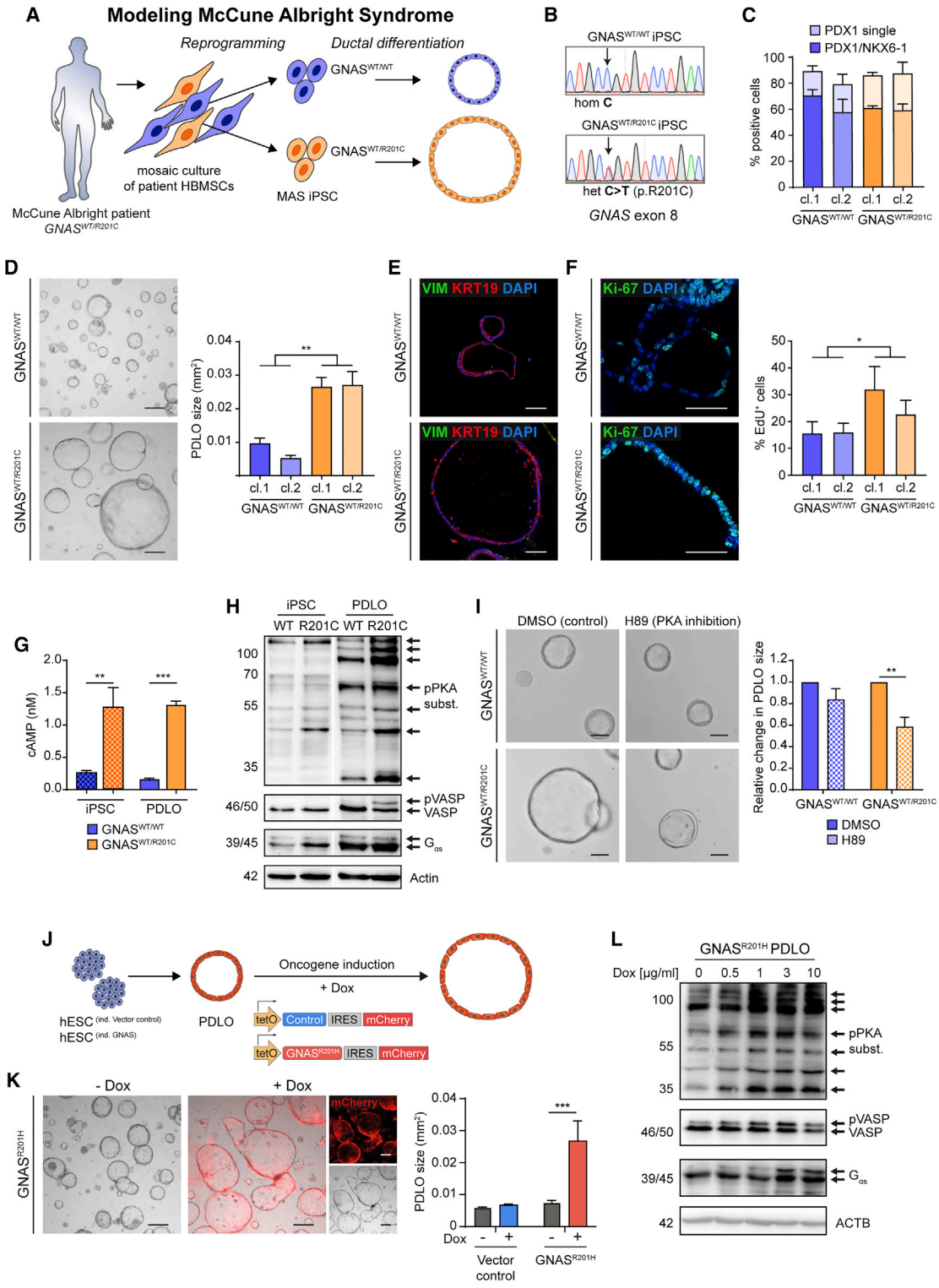

Figure 6. McCune-Albright syndrome (MAS)-derived and GNAS^{R201H}-overexpressing PDLOs form large cysts

(A) Scheme of generating isogenic iPSC lines from a MAS patient carrying a mosaic GNAS$^{WT/R201C}$ mutation followed by PDLO formation.

(B) Sequencing results of selected iPSC clones.

(C) FC-based PP quantification after differentiation of GNAS$^{WT/WT}$ and GNAS$^{WT/R201C}$ MAS-iPSCs (n = 3; cl., clonally derived iPSC line).

(D) BF PDLO images from MAS-iPSCs. Right: size comparison.

(E) VIM and KRT19 IF staining of MAS-PDLOs.

(legend continued on next page)

Please cite this article in press as: Breunig et al., Modeling plasticity and dysplasia of pancreatic ductal organoids derived from human pluripotent stem cells, Cell Stem Cell (2021), https://doi.org/10.1016/j.stem.2021.03.005

microenvironment. PDLOs generated via (1) GNAS$^{WT/R201C}$ iPSCs derived from an MAS patient or (2) hESCs carrying an inducible GNAS^{R201H} formed large cystic structures compared to respective control counterparts. We confirmed that the $G_{\alpha s}$-PKA-VASP signaling axis was important for the cystic growth of GNAS$^{WT/R201C}$ PDLOs. GNAS^{R201H}-expressing PDLOs formed IPMN-like structures after orthotopic transplantation, thus underpinning the role of mutant GNAS as the main driver of cystic neoplastic growth in pancreatic ducts (Ideno et al., 2018; Patra et al., 2018).

In PDLOs overexpressing KRAS^{G12D}, we observed a specific morphological lumen-filling phenotype, a characteristic previously reported to indicate dysplastic growth from KRAS mutant organoids (Seino et al., 2018). On a molecular level, pro-apoptotic as well as features indicating OIS were upregulated upon KRAS^{G12D} induction. OIS has been established as a cancer progression roadblock, particularly in precursor lesions of various cancers, including prostate and pancreas (Chen et al., 2005; Morton et al., 2010). As senescence-associated β-galactosidase activity cannot be assessed on formalin-fixed paraffin-embedded (FFPE) tissue (Caldwell et al., 2012), OIS effectors, including P53, P21, and RB were investigated in PDLO grafts instead. Orthotopic PDLO engraftment was sufficient to partially trigger checkpoint evasion, licensing various routes to cancerous growth and subsequent heterogeneity. Future studies need to clarify KRAS^{G12D}-driven cancer progression and metastatic traits by allowing graft development beyond the 8-week time point chosen in the present study.

While apoptosis and OIS counteract tumorigenesis, EMT is considered to be a crucial driving process for cancer plasticity and invasion into local tissue. EMT-associated transcription factors can mediate a switch to bypass senescence and activate EMT by oncogenic stimuli such as high-dose KRAS (Ansieau et al., 2008; Ohashi et al., 2010). The combination of unleashed KRAS^{G12D} and lost CDKN2A again triggered EMT gene expression, accompanied by cells disseminating from the organoid body. Dissemination and EMT marker expression in PDLO grafts *in vivo* were spatially concordant with high levels of KRAS^{G12D}, an observation facilitated by the heterogeneous expression of the inducible transgene. This is intriguing, as PDAC appears to implement various routes to intrinsically amplify *KRAS* gene dosage (Mueller et al., 2018; Chan-Seng-Yue et al., 2020). Accordingly, large-scale sequencing of multiple established PDAC genomes identified *CDKN2A* as well as major allelic imbalance in mutant *KRAS* to mark a switch from a classical to a basal-like subtype, characterized by high EMT scores and frequently observed in stage IV disease (Moffitt et al., 2015; Chan-Seng-Yue et al., 2020; Puleo et al., 2018). However, neither of the aforementioned studies started from a genetically defined untransformed pancreatic background. Thus, our PDAC modeling efforts that combine different oncogenic events in PDLOs are in line with the current picture of PDAC evolution, underpinning the value of the model.

Conclusions

Our PSC-derived PDLOs, together with reprogramming technologies and advances in gene editing, allow the customized design of a disease initiation and progression landscape. We hereby leverage opportunities for longitudinal studies alongside material access for distinct multi-dimensional analytics *in vitro* and *in vivo*. As an example, a head-to-head comparison of oncogene expression in ducts and in acini engineered from human pluripotent stem cells will help to answer unresolved questions during pancreatic carcinogenesis: how does the cell type of origin affect human PDAC biology, and why are ductal cells more refractory to developing PanIN lesions, but progress faster to PDACs (Lee et al., 2019; Ferreira et al., 2017)? As low-grade preneoplastic lesions were rare in our 8-week grafts and appeared to progress rapidly to cancer, transplanted PDLOs have the capacity to provide answers for the duct-specific pathomechanisms of PDAC development. Our results are consistent with a parallel study from Muthuswamy and colleagues (Huang et al., 2021) reporting the development of conditions for generation of human acinar and ductal organoids from stem cells and using them to model exocrine development and early stages of pancreas cancer. In summary, our robust PSC differentiation matrix opens a variety of different applications in pancreatic development and cancer research and fuels a versatile human research hub to gain access into the spatiotemporally resolved evolution of dysplasia and plasticity in pancreatic cancer.

Limitations of study

The aim of our study was to derive ductal cells from human PPs. Acinar cells generated from the same PP ancestors would be desirable to study oncogene and tumor suppressor gene function in a lineage-dependent manner. A long-term PDLO culture format has yet not been fully established, thus requiring transplantation studies for further investigation of tumor progression. Also, the microenvironment *in vivo* is incomplete due to the use of immunocompromised mice.

STAR★METHODS

Detailed methods are provided in the online version of this paper and include the following:

- KEY RESOURCES TABLE

(F) Ki-67 IF staining (left images) and FC analysis after EdU treatment (right) showed increased proliferation of GNAS$^{WT/R201C}$ PDLOs.
(G) Analysis of cAMP levels in MAS-iPSC and PDLO cells (n = 1; in triplicate).
(H) WB showing increased PKA signaling in GNAS$^{WT/R201C}$ PDLOs. iPSC and PDLO samples shown separately were detected on the same blot; image was cropped due to additional loaded samples (n = 1).
(I) Representative BF images of MAS-iPSC-derived PDLOs treated with PKA inhibitor H89 or DMSO for 9 days. Right: size quantification of PDLOs upon inhibition of PKA signaling (n = 3).
(J) Timed induction of a *piggyBac* GNAS^{R201H} transposon construct in engineered HUES8.
(K) BF images of GNAS^{R201H} PDLO cultures after 7 days on Dox (red: mCherry signal). Right: PDLO size quantification (n = 3; in triplicate).
(L) Dox concentration-dependent increase of PKA signaling in PDLOs after Dox treatment for 3 days. Scale bar: 200 μm, if not stated otherwise.
Means ± SEMs. (D and F) n = 6 experiments per group (3 per individual clone), Mann-Whitney test. (G) Ordinary 1-way ANOVA with Tukey's multiple comparison test. (I and K) Ordinary 2-way ANOVA with Sidak's multiple comparison test; only significant comparisons are depicted.

Please cite this article in press as: Breunig et al., Modeling plasticity and dysplasia of pancreatic ductal organoids derived from human pluripotent stem cells, Cell Stem Cell (2021), https://doi.org/10.1016/j.stem.2021.03.005

CellPress

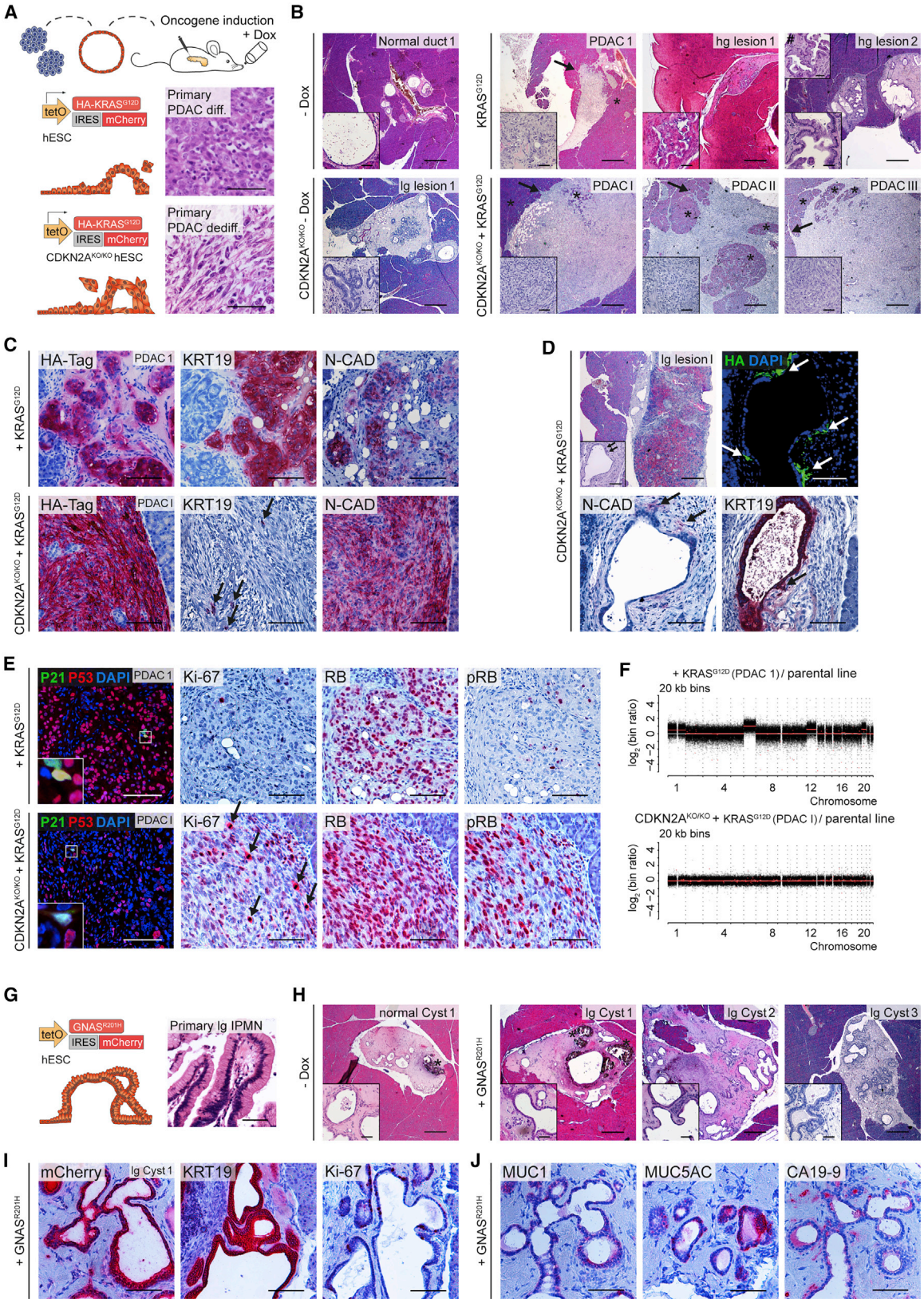

(legend on next page)

SUPPLEMENTAL INFORMATION

Supplemental information can be found online at https://doi.org/10.1016/j.stem.2021.03.005.

ACKNOWLEDGMENTS

The authors thank Katrin Köhn, Aref Saed, Ulrike Mayr-Beyrle, Juliane Nell, Rashmi Bijegatte, Claudia Ruhland, and Ralf Köhntop for excellent technical assistance and Franz Oswald, Barbara Möpps, Johann Gout, Elodie Roger, Frank Arnold, Tim Eiseler, Florian Weeber, Karolin Walter, and Kanishka Tiwary for helpful discussions. They acknowledge Rupert Öllinger for performing the RNA-seq experiments and Olga Baranov and Sebastian Lange for assisting with the lcWGS analysis. We also want to thank Ivan Costa and Julia Gehrmann for providing input on the RNA-seq data evaluation and Ralf Marienfeld for performing the panel sequencing. They also thank Paul Walther and the Electron Microscopy Group and Inken Beck and the team of the "Tierforschungszentrum" at Ulm University. The authors acknowledge O.D. Madsen and the Developmental Studies Hybridoma Bank (DSHB) for providing the NKX6-1 antibody. The main funding was provided by the Deutsche Forschungsgemeinschaft (DFG) "Sachbeihilfe" KL 2544/7-1 and "Heisenberg-Programm" KL 2544/6-1 as well as the Baden-Württemberg-Foundation ExPoChip. A.K. and T.S. are PIs in the HEIST RTG funded by the DFG GRK 2254/1. Additional funding came from the German Cancer Aid grant to A.K. (111879), the DFG (K.L. 2544/1-1, 1-2, and 5-1), the INDIMED-Verbund PancChip, and the Else Kröner-Fresenius-Stiftung supporting A.K. with an Excellence grant and M.H. with a First Application grant. L.P. received funding by the DFG (PE 3337/1-1). M.H., L.P., and S.H. received supportive funds from the Bausteinprogramm of Ulm University. P.G.R. was supported by the DIR of the NIDCR, a part of the IRP, NIH, DHHS. M.R. was supported by the German

Figure 7. Mutation-dependent PDAC- or IPMN-like tumor formation from PDLO grafts

(A) Schema of orthotopic PDLO transplantations. Oncogene expression was induced *in vivo* for 8 weeks. Reference images of H&E staining of primary PDAC patient tissue are depicted for illustration.

(B) H&E overview images of grafts that developed from $KRAS^{G12D}$ and $CDKN2A^{KO/KO}$ $KRAS^{G12D}$ PDLOs with and without oncogene induction (lg/hg lesion, low-grade/high-grade preneoplastic lesion). Asterisks label murine pancreas tissue, arrows indicate invasive tumor growth, and pound sign marks a second inset from a different section of the same graft, demonstrating a higher grade of cellular atypia. See Figure S7A for the number of transplanted mice.

(C) IHC staining showing that $KRAS^{G12D}$ induction (reflected by HA-tag) alone led to differentiated PDAC, and $CDKN2A^{KO/KO}$ $KRAS^{G12D}$ led to dedifferentiated PDAC. Arrows highlight single epithelial cells in the $CDKN2A^{KO/KO}$ $KRAS^{G12D}$ graft.

(D) One specific $CDKN2A^{KO/KO}$ $KRAS^{G12D}$ graft with heterogenous transgene induction. Sites of dissemination and EMT correlate with HA-tag expression (indicated by arrows).

(E) Staining of cell-cycle-associated proteins. Few $P21^{+}$ cells. RB/pRB staining indicated an intact checkpoint control in $KRAS^{G12D}$ tumors, but nearly complete loss of active RB in $CDKN2A^{KO/KO}$ $KRAS^{G12D}$ grafts, resulting in increased proliferation (Ki-67) in $CDKN2A^{KO/KO}$ $KRAS^{G12D}$ grafts. Arrows highlight several mitoses in the $CDKN2A^{KO/KO}$ $KRAS^{G12D}$ graft.

(F) lcWGS of PDLO-derived tumors.

(G) Schema and reference H&E image of primary patient IPMN tissue.

(H) IPMN-like lesion formation observed after $GNAS^{R201H}$ induction *in vivo*. H&E overview of low-grade cystic $GNAS^{R201H}$ grafts and control without Dox treatment. Asterisks label disrupted Matrigel, observed in few grafts. See Figure S7A for the number of transplanted mice.

(I and J) IHC staining indicating IPMN formation after $GNAS^{R201H}$ induction (confirmed by mCherry expression).

Scale bar: 100 μm, except for H&E staining in (B), (D), and (H) (500 μm); in insets: 50 μm.

Cancer Aid (Max Eder Program, Deutsche Krebshilfe 111273) and the DFG (SFB1321 Modeling and Targeting Pancreatic Cancer INST 95/1470-1 and INST 95/1461-1, as well as RE 3723/4-1). C.M.C. and S.S. received supportive funds from the DFG (SFB TRR 127 Biology of Xenogeneic Cell and Organ Transplantation) and the Paul Langerhans Institute Dresden (PLID) of Helmholtz Zentrum München at the University Clinic Carl Gustav Carus of Technische Universität Dresden. The research was supported by the Hungarian Academy of Sciences (LP2017–18/2017) and the EU's Horizon 2020 (739593). R.R. was supported by the DFG (SFB1321) and the European Research Council (Consolidator Grant 819642 PACA- MET and MSCA- ITN-ETN 861196).

AUTHOR CONTRIBUTIONS

Conceptualization, M.B., M. Meier, M.H., and A.K.; methodology, M.B., J.M., M.W., T.F.E.B., T.E., J. Krumm, S.W., C.M.C., L.P., G.J., T.M., O.W., P.C.H., S.H., M.R., C.G., B.S., M. Meier, and M.H.; software, M.B., T.E., J. Krumm, S.W., G.J., O.W., B.K., and R.R.; validation, M.B., J.M., M.W., T.F.E.B., M.K.M., B.S., M. Meier, M.H., and A.K.; formal analysis, M.B., J.M., M.W., T.E., M.K.M., J. Krumm, T.M., Á.V., and M.H.; investigation, M.B., J.M., M.W., T.F.E.B., T.E., M.K.M, J. Krumm, S.W., C.M.C., L.P., J. Krüger, M.S., T.M., Á.V., J.G., N.A., M. Müller, P.C.H., M. Meier, and M.H.; resources, M.W., T.F.E.B., C.M.C., M. Müller, P.G.R., Z.D., M.R., C.G., C.B., J. Maléth, S.S., T.S., B.S., M. Meier, and A.K.; data curation, M.B., M.W., T.E., J. Krumm, G.J., T.M., J. Maléth, B.K., and R.R.; writing – original draft, M.B., J.M., M. Meier, M.H., and A.K.; writing – review & editing, M.B., J.M., M.W., T.E., M.K.M., J. Krumm, S.W., C.M.C., G.J., P.C.H., T.M., Á.V., P.G.R., S.H., M.R., J. Maléth, T.S., S.L., M. Meier, M.H., and A.K.; visualization, M.B., J.M., M.W., T.F.E.B., T.E., M.K.M., J. Krumm, C.M.C., G.J., T.M., Á.V., M. Meier, M.H., and A.K.; supervision, M. Meier, M.H., and A.K.; project administration, M.B., J.M., M.H., and A.K.; funding acquisition, C.M.C., L.P., S.H., M.R., C.B., F.K., S.S., T.S., M.H., M. Meier, and A.K.

DECLARATION OF INTERESTS

The authors declare no competing interests.

Received: May 1, 2020
Revised: December 22, 2020
Accepted: March 9, 2021
Published: April 28, 2021

REFERENCES

Aiello, N.M., Maddipati, R., Norgard, R.J., Balli, D., Li, J., Yuan, S., Yamazoe, T., Black, T., Sahmoud, A., Furth, E.E., et al. (2018). EMT Subtype Influences Epithelial Plasticity and Mode of Cell Migration. Dev. Cell *45*, 681–695.e4.

Ansieau, S., Bastid, J., Doreau, A., Morel, A.P., Bouchet, B.P., Thomas, C., Fauvet, F., Puisieux, I., Doglioni, C., Piccinin, S., et al. (2008). Induction of EMT by twist proteins as a collateral effect of tumor-promoting inactivation of premature senescence. Cancer Cell *14*, 79–89.

Baron, M., Veres, A., Wolock, S.L., Faust, A.L., Gaujoux, R., Vetere, A., Ryu, J.H., Wagner, B.K., Shen-Orr, S.S., Klein, A.M., et al. (2016). A Single-Cell Transcriptomic Map of the Human and Mouse Pancreas Reveals Inter- and Intra-cell Population Structure. Cell Syst. *3*, 346–360.e4.

Bartek, J., Bartkova, J., and Lukas, J. (2007). DNA damage signalling guards against activated oncogenes and tumour progression. Oncogene *26*, 7773–7779.

Benjamini, Y., and Hochberg, Y. (1995). Controlling the false discovery rate: a practical and powerful approach to multiple testing. J. R. Stat. Soc. B *57*, 289–300.

Bianco, P., Kuznetsov, S.A., Riminucci, M., Fisher, L.W., Spiegel, A.M., and Robey, P.G. (1998). Reproduction of human fibrous dysplasia of bone in immunocompromised mice by transplanted mosaics of normal and Gsalpha-mutated skeletal progenitor cells. J. Clin. Invest. *101*, 1737–1744.

Biederstädt, A., Hassan, Z., Schneeweis, C., Schick, M., Schneider, L., Muckenhuber, A., Hong, Y., Siegers, G., Nilsson, L., Wirth, M., et al. (2020). SUMO pathway inhibition targets an aggressive pancreatic cancer subtype. Gut *69*, 1472–1482.

Blondel, V.D., Guillaume, J.-L., Lambiotte, R., and Lefebvre, E. (2008). Fast unfolding of communities in large networks. J. Stat. Mech. *2008*, P10008.

Boj, S.F., Hwang, C.I., Baker, L.A., Chio, I.I., Engle, D.D., Corbo, V., Jager, M., Ponz-Sarvise, M., Tiriac, H., Spector, M.S., et al. (2015). Organoid models of human and mouse ductal pancreatic cancer. Cell *160*, 324–338.

Bolger, A.M., Lohse, M., and Usadel, B. (2014). Trimmomatic: a flexible trimmer for Illumina sequence data. Bioinformatics *30*, 2114–2120.

Brion, L.P., Schwartz, J.H., Zavilowitz, B.J., and Schwartz, G.J. (1988). Micromethod for the measurement of carbonic anhydrase activity in cellular homogenates. Anal. Biochem. *175*, 289–297.

Burghardt, B., Elkaer, M.L., Kwon, T.H., Rácz, G.Z., Varga, G., Steward, M.C., and Nielsen, S. (2003). Distribution of aquaporin water channels AQP1 and AQP5 in the ductal system of the human pancreas. Gut *52*, 1008–1016.

Caldwell, M.E., DeNicola, G.M., Martins, C.P., Jacobetz, M.A., Maitra, A., Hruban, R.H., and Tuveson, D.A. (2012). Cellular features of senescence during the evolution of human and murine ductal pancreatic cancer. Oncogene *31*, 1599–1608.

Chan-Seng-Yue, M., Kim, J.C., Wilson, G.W., Ng, K., Figueroa, E.F., O'Kane, G.M., Connor, A.A., Denroche, R.E., Grant, R.C., McLeod, J., et al. (2020). Transcription phenotypes of pancreatic cancer are driven by genomic events during tumor evolution. Nat. Genet. *52*, 231–240.

Chen, Z., Trotman, L.C., Shaffer, D., Lin, H.K., Dotan, Z.A., Niki, M., Koutcher, J.A., Scher, H.I., Ludwig, T., Gerald, W., et al. (2005). Crucial role of p53-dependent cellular senescence in suppression of Pten-deficient tumorigenesis. Nature *436*, 725–730.

Chmelova, H., Cohrs, C.M., Chouinard, J.A., Petzold, C., Kuhn, M., Chen, C., Roeder, I., Kretschmer, K., and Speier, S. (2015). Distinct roles of β-cell mass and function during type 1 diabetes onset and remission. Diabetes *64*, 2148–2160.

Cho, C.H., Hannan, N.R., Docherty, F.M., Docherty, H.M., João Lima, M., Trotter, M.W., Docherty, K., and Vallier, L. (2012). Inhibition of activin/nodal signalling is necessary for pancreatic differentiation of human pluripotent stem cells. Diabetologia *55*, 3284–3295.

Cogger, K.F., Sinha, A., Sarangi, F., McGaugh, E.C., Saunders, D., Dorrell, C., Mejia-Guerrero, S., Aghazadeh, Y., Rourke, J.L., Screaton, R.A., et al. (2017). Glycoprotein 2 is a specific cell surface marker of human pancreatic progenitors. Nat. Commun. *8*, 331.

Cohrs, C.M., Chen, C., and Speier, S. (2020). Transplantation of Islets of Langerhans into the Anterior Chamber of the Eye for Longitudinal In Vivo Imaging. Methods Mol. Biol. *2128*, 149–157.

Cox, J., and Mann, M. (2008). MaxQuant enables high peptide identification rates, individualized p.p.b.-range mass accuracies and proteome-wide protein quantification. Nat. Biotechnol. *26*, 1367–1372.

Czodrowski, P., Mallinger, A., Wienke, D., Esdar, C., Pöschke, O., Busch, M., Rohdich, F., Eccles, S.A., Ortiz-Ruiz, M.J., Schneider, R., et al. (2016). Structure-Based Optimization of Potent, Selective, and Orally Bioavailable CDK8 Inhibitors Discovered by High-Throughput Screening. J. Med. Chem. *59*, 9337–9349.

Dantes, Z., Yen, H.Y., Pfarr, N., Winter, C., Steiger, K., Muckenhuber, A., Hennig, A., Lange, S., Engleitner, T., Öllinger, R., et al. (2020). Implementing cell-free DNA of pancreatic cancer patient-derived organoids for personalized oncology. JCI Insight *5*, e137809.

De Lichtenberg, K.H., Seymour, P.A., Jørgensen, M.C., Kim, Y.-H., Grapin-Botton, A., Magnuson, M.A., Nakic, N., Ferrer, J., and Serup, P. (2018). Notch Controls Multiple Pancreatic Cell Fate Regulators Through Direct Hes1-mediated Repression. BioRxiv. https://doi.org/10.1101/336305.

Dekkers, J.F., Wiegerinck, C.L., de Jonge, H.R., Bronsveld, I., Janssens, H.M., de Winter-de Groot, K.M., Brandsma, A.M., de Jong, N.W., Bijvelds, M.J., Scholte, B.J., et al. (2013). A functional CFTR assay using primary cystic fibrosis intestinal organoids. Nat. Med. *19*, 939–945.

Di Micco, R., Fumagalli, M., Cicalese, A., Piccinin, S., Gasparini, P., Luise, C., Schurra, C., Garre', M., Nuciforo, P.G., Bensimon, A., et al. (2006). Oncogene-

induced senescence is a DNA damage response triggered by DNA hyper-replication. Nature *444*, 638–642.

Ding, Q., Regan, S.N., Xia, Y., Oostrom, L.A., Cowan, C.A., and Musunuru, K. (2013). Enhanced efficiency of human pluripotent stem cell genome editing through replacing TALENs with CRISPRs. Cell Stem Cell *12*, 393–394.

Dobin, A., Davis, C.A., Schlesinger, F., Drenkow, J., Zaleski, C., Jha, S., Batut, P., Chaisson, M., and Gingeras, T.R. (2013). STAR: ultrafast universal RNA-seq aligner. Bioinformatics *29*, 15–21.

Enge, M., Arda, H.E., Mignardi, M., Beausang, J., Bottino, R., Kim, S.K., and Quake, S.R. (2017). Single-Cell Analysis of Human Pancreas Reveals Transcriptional Signatures of Aging and Somatic Mutation Patterns. Cell *171*, 321–330.e14.

Ferreira, R.M.M., Sancho, R., Messal, H.A., Nye, E., Spencer-Dene, B., Stone, R.K., Stamp, G., Rosewell, I., Quaglia, A., and Behrens, A. (2017). Duct- and Acinar-Derived Pancreatic Ductal Adenocarcinomas Show Distinct Tumor Progression and Marker Expression. Cell Rep. *21*, 966–978.

Frappart, P.O., Walter, K., Gout, J., Beutel, A.K., Morawe, M., Arnold, F., Breunig, M., Barth, T.F., Marienfeld, R., Schulte, L., et al. (2020). Pancreatic cancer-derived organoids – a disease modeling tool to predict drug response. United European Gastroenterol. J. *8*, 594–606.

Frejno, M., Zenezini Chiozzi, R., Wilhelm, M., Koch, H., Zheng, R., Klaeger, S., Ruprecht, B., Meng, C., Kramer, K., Jarzab, A., et al. (2017). Pharmacoproteomic characterisation of human colon and rectal cancer. Mol. Syst. Biol. *13*, 951.

Frishberg, A., Peshes-Yaloz, N., Cohn, O., Rosentul, D., Steuerman, Y., Valadarsky, L., Yankovitz, G., Mandelboim, M., Iraqi, F.A., Amit, I., et al. (2019). Cell composition analysis of bulk genomics using single-cell data. Nat. Methods *16*, 327–332.

Fryer, C.J., White, J.B., and Jones, K.A. (2004). Mastermind recruits CycC:CDK8 to phosphorylate the Notch ICD and coordinate activation with turnover. Mol. Cell *16*, 509–520.

Furukawa, T., Klöppel, G., Volkan Adsay, N., Albores-Saavedra, J., Fukushima, N., Horii, A., Hruban, R.H., Kato, Y., Klimstra, D.S., Longnecker, D.S., et al. (2005). Classification of types of intraductal papillary-mucinous neoplasm of the pancreas: a consensus study. Virchows Arch. *447*, 794–799.

Gaujoux, S., Salenave, S., Ronot, M., Rangheard, A.S., Cros, J., Belghiti, J., Sauvanet, A., Ruszniewski, P., and Chanson, P. (2014). Hepatobiliary and Pancreatic neoplasms in patients with McCune-Albright syndrome. J. Clin. Endocrinol. Metab. *99*, E97–E101.

Georgakopoulos, N., Prior, N., Angres, B., Mastrogiovanni, G., Cagan, A., Harrison, D., Hindley, C.J., Arnes-Benito, R., Liau, S.S., Curd, A., et al. (2020). Long-term expansion, genomic stability and in vivo safety of adult human pancreas organoids. BMC Dev. Biol. *20*, 4.

Gerrard, D.T., Berry, A.A., Jennings, R.E., Piper Hanley, K., Bobola, N., and Hanley, N.A. (2016). An integrative transcriptomic atlas of organogenesis in human embryos. eLife *5*, e15657.

Gliwicz, D., Jankowska, I., Wierzbicka, A., Miśkiewicz-Chotnicka, A., Lisowska, A., and Walkowiak, J. (2016). Exocrine pancreatic function in children with Alagille syndrome. Sci. Rep. *6*, 35229.

Gloeckner, C.J., Boldt, K., Schumacher, A., and Ueffing, M. (2009). Tandem affinity purification of protein complexes from mammalian cells by the Strep/FLAG (SF)-TAP tag. Methods Mol. Biol. *564*, 359–372.

Golson, M.L., Loomes, K.M., Oakey, R., and Kaestner, K.H. (2009). Ductal malformation and pancreatitis in mice caused by conditional Jag1 deletion. Gastroenterology *136*, 1761–17671.e1.

Grigore, A.D., Jolly, M.K., Jia, D., Farach-Carson, M.C., and Levine, H. (2016). Tumor Budding: The Name is EMT. Partial EMT. J. Clin. Med. *5*, 51.

Haeussler, M., Schönig, K., Eckert, H., Eschstruth, A., Mianné, J., Renaud, J.B., Schneider-Maunoury, S., Shkumatava, A., Teboul, L., Kent, J., et al. (2016). Evaluation of off-target and on-target scoring algorithms and integration into the guide RNA selection tool CRISPOR. Genome Biol. *17*, 148.

Heng, L. (2013). Aligning sequence reads, clone sequences and assembly contigs with BWA-MEM. arXiv, 1303.3997v2 https://arxiv.org/abs/1303.3997.

Hogrebe, N.J., Augsornworawat, P., Maxwell, K.G., Velazco-Cruz, L., and Millman, J.R. (2020). Targeting the cytoskeleton to direct pancreatic differentiation of human pluripotent stem cells. Nat. Biotechnol. *38*, 460–470.

Hohwieler, M., Illing, A., Hermann, P.C., Mayer, T., Stockmann, M., Perkhofer, L., Eiseler, T., Antony, J.S., Müller, M., Renz, S., et al. (2017). Human pluripotent stem cell-derived acinar/ductal organoids generate human pancreas upon orthotopic transplantation and allow disease modelling. Gut *66*, 473–486.

Hohwieler, M., Müller, M., Frappart, P.O., and Heller, S. (2019). Pancreatic Progenitors and Organoids as a Prerequisite to Model Pancreatic Diseases and Cancer. Stem Cells Int. *2019*, 9301382.

Huang, L., Desai, R., Conrad, D.N., Carvalho Leite, N., Akshinthala, D., Lim, C.M., Gonzalez, R., Muthuswamy, L.B., Gartner, Z., and Muthuswamy, S.K. (2021). Commitment and oncogene-induced plasticity of human stem cell-derived pancreatic acinar and ductal organoids. Cell Stem Cell *28*. Published online April 28, 2021. https://doi.org/10.1016/j.stem.2021.03.022.

Huang, L., Holtzinger, A., Jagan, I., BeGora, M., Lohse, I., Ngai, N., Nostro, C., Wang, R., Muthuswamy, L.B., Crawford, H.C., et al. (2015). Ductal pancreatic cancer modeling and drug screening using human pluripotent stem cell- and patient-derived tumor organoids. Nature medicine *21*, 1364–1371.

Ideno, N., Yamaguchi, H., Ghosh, B., Gupta, S., Okumura, T., Steffen, D.J., Fisher, C.G., Wood, L.D., Singhi, A.D., Nakamura, M., et al. (2018). $GNAS^{R201C}$ Induces Pancreatic Cystic Neoplasms in Mice That Express Activated KRAS by Inhibiting YAP1 Signaling. Gastroenterology *155*, 1593–1607.e12.

Illing, A., Stockmann, M., Swamy Telugu, N., Linta, L., Russell, R., Müller, M., Seufferlein, T., Liebau, S., and Kleger, A. (2013). Definitive Endoderm Formation from Plucked Human Hair-Derived Induced Pluripotent Stem Cells and SK Channel Regulation. Stem Cells Int. *2013*, 360573.

Johnson, W.E., Li, C., and Rabinovic, A. (2007). Adjusting batch effects in microarray expression data using empirical Bayes methods. Biostatistics *8*, 118–127.

Kesavan, G., Sand, F.W., Greiner, T.U., Johansson, J.K., Kobberup, S., Wu, X., Brakebusch, C., and Semb, H. (2009). Cdc42-mediated tubulogenesis controls cell specification. Cell *139*, 791–801.

Kim, S.I., Oceguera-Yanez, F., Sakurai, C., Nakagawa, M., Yamanaka, S., and Woltjen, K. (2016). Inducible Transgene Expression in Human iPS Cells Using Versatile All-in-One piggyBac Transposons. Methods Mol. Biol. *1357*, 111–131.

Klausen, P., Kovacevic, B., Toxvaerd, A., Kalaitzakis, E., Karstensen, J.G., Rift, C.V., Hansen, C.P., Storkholm, J., Vilmann, P., and Hasselby, J.P. (2019). Subtyping of intraductal papillary mucinous neoplasms - pitfalls of MUC1 immunohistochemistry. APMIS *127*, 27–32.

Kopp, J.L., Dubois, C.L., Schaeffer, D.F., Samani, A., Taghizadeh, F., Cowan, R.W., Rhim, A.D., Stiles, B.L., Valasek, M., and Sander, M. (2018). Loss of Pten and Activation of Kras Synergistically Induce Formation of Intraductal Papillary Mucinous Neoplasia From Pancreatic Ductal Cells in Mice. Gastroenterology *154*, 1509–1523.e5.

Krentz, N.A.J., Lee, M.Y.Y., Xu, E.E., Sproul, S.L.J., Maslova, A., Sasaki, S., and Lynn, F.C. (2018). Single-Cell Transcriptome Profiling of Mouse and hESC-Derived Pancreatic Progenitors. Stem Cell Reports *11*, 1551–1564.

Kuilman, T. (2020). CopywriteR: Copy number information from targeted sequencing using off-target reads. https://github.com/PeeperLab/CopywriteR.

Kuilman, T., Michaloglou, C., Vredeveld, L.C., Douma, S., van Doorn, R., Desmet, C.J., Aarden, L.A., Mooi, W.J., and Peeper, D.S. (2008). Oncogene-induced senescence relayed by an interleukin-dependent inflammatory network. Cell *133*, 1019–1031.

Kuleshov, M.V., Jones, M.R., Rouillard, A.D., Fernandez, N.F., Duan, Q., Wang, Z., Koplev, S., Jenkins, S.L., Jagodnik, K.M., Lachmann, A., et al. (2016). Enrichr: a comprehensive gene set enrichment analysis web server 2016 update. Nucleic Acids Res. *44* (W1), W90–W97.

Lee, S., and Schmitt, C.A. (2019). The dynamic nature of senescence in cancer. Nat. Cell Biol. *21*, 94–101.

Lee, A.Y.L., Dubois, C.L., Sarai, K., Zarei, S., Schaeffer, D.F., Sander, M., and Kopp, J.L. (2019). Cell of origin affects tumour development and phenotype in pancreatic ductal adenocarcinoma. Gut *68*, 487–498.

Leek, J.T., Johnson, W.E., Parker, H.S., Jaffe, A.E., and Storey, J.D. (2012). The sva package for removing batch effects and other unwanted variation in high-throughput experiments. Bioinformatics *28*, 882–883.

Lesina, M., Wörmann, S.M., Morton, J., Diakopoulos, K.N., Korneeva, O., Wimmer, M., Einwächter, H., Sperveslage, J., Demir, I.E., Kehl, T., et al. (2016). RelA regulates CXCL1/CXCR2-dependent oncogene-induced senescence in murine Kras-driven pancreatic carcinogenesis. J. Clin. Invest. *126*, 2919–2932.

Levine, J.H., Simonds, E.F., Bendall, S.C., Davis, K.L., Amir, A.D., Tadmor, M.D., Litvin, O., Fienberg, H.G., Jager, A., Zunder, E.R., et al. (2015). Data-Driven Phenotypic Dissection of AML Reveals Progenitor-like Cells that Correlate with Prognosis. Cell *162*, 184–197.

Liao, Y., Smyth, G.K., and Shi, W. (2019). The R package Rsubread is easier, faster, cheaper and better for alignment and quantification of RNA sequencing reads. Nucleic Acids Res. *47*, e47.

Linta, L., Stockmann, M., Kleinhans, K.N., Böckers, A., Storch, A., Zaehres, H., Lin, Q., Barbi, G., Böckers, T.M., Kleger, A., and Liebau, S. (2012). Rat embryonic fibroblasts improve reprogramming of human keratinocytes into induced pluripotent stem cells. Stem Cells Dev. *21*, 965–976.

Love, M.I., Huber, W., and Anders, S. (2014). Moderated estimation of fold change and dispersion for RNA-seq data with DESeq2. Genome Biol. *15*, 550.

Lun, A.T., McCarthy, D.J., and Marioni, J.C. (2016). A step-by-step workflow for low-level analysis of single-cell RNA-seq data with Bioconductor. F1000Res. *5*, 2122.

Macosko, E.Z., Basu, A., Satija, R., Nemesh, J., Shekhar, K., Goldman, M., Tirosh, I., Bialas, A.R., Kamitaki, N., Martersteck, E.M., et al. (2015). Highly parallel genome-wide expression profiling of individual cells using nanoliter droplets. Cell *161*, 1202–1214.

Maléth, J., Balázs, A., Pallagi, P., Balla, Z., Kui, B., Katona, M., Judák, L., Németh, I., Kemény, L.V., Rakonczay, Z., Jr., et al. (2015). Alcohol disrupts levels and function of the cystic fibrosis transmembrane conductance regulator to promote development of pancreatitis. Gastroenterology *148*, 427–439.e16.

Mali, P., Yang, L., Esvelt, K.M., Aach, J., Guell, M., DiCarlo, J.E., Norville, J.E., and Church, G.M. (2013). RNA-guided human genome engineering via Cas9. Science *339*, 823–826.

Mcinnes, L., Healy, J., and Melville, J. (2018). Umap: Uniform manifold approximation and projection for dimension reduction. arXiv, 1802.03426v3 https://arxiv.org/abs/1802.03426.

Moffitt, R.A., Marayati, R., Flate, E.L., Volmar, K.E., Loeza, S.G., Hoadley, K.A., Rashid, N.U., Williams, L.A., Eaton, S.C., Chung, A.H., et al. (2015). Virtual microdissection identifies distinct tumor- and stroma-specific subtypes of pancreatic ductal adenocarcinoma. Nat. Genet. *47*, 1168–1178.

Molnár, R., Madácsy, T., Varga, Á., Németh, M., Katona, X., Görög, M., Molnár, B., Fanczal, J., Rakonczay, Z., Jr., Hegyi, P., et al. (2020). Mouse pancreatic ductal organoid culture as a relevant model to study exocrine pancreatic ion secretion. Lab. Invest. *100*, 84–97.

Moreira, L., Bakir, B., Chatterji, P., Dantes, Z., Reichert, M., and Rustgi, A.K. (2017). Pancreas 3D Organoids: Current and Future Aspects as a Research Platform for Personalized Medicine in Pancreatic Cancer. Cell. Mol. Gastroenterol. Hepatol. *5*, 289–298.

Morton, J.P., Timpson, P., Karim, S.A., Ridgway, R.A., Athineos, D., Doyle, B., Jamieson, N.B., Oien, K.A., Lowy, A.M., Brunton, V.G., et al. (2010). Mutant p53 drives metastasis and overcomes growth arrest/senescence in pancreatic cancer. Proc. Natl. Acad. Sci. USA *107*, 246–251.

Mueller, S., Engleitner, T., Maresch, R., Zukowska, M., Lange, S., Kaltenbacher, T., Konukiewitz, B., Öllinger, R., Zwiebel, M., Strong, A., et al. (2018). Evolutionary routes and KRAS dosage define pancreatic cancer phenotypes. Nature *554*, 62–68.

Nostro, M.C., Sarangi, F., Yang, C., Holland, A., Elefanty, A.G., Stanley, E.G., Greiner, D.L., and Keller, G. (2015). Efficient generation of NKX6-1+ pancreatic progenitors from multiple human pluripotent stem cell lines. Stem Cell Reports *4*, 591–604.

Notta, F., Chan-Seng-Yue, M., Lemire, M., Li, Y., Wilson, G.W., Connor, A.A., Denroche, R.E., Liang, S.B., Brown, A.M., Kim, J.C., et al. (2016). A renewed model of pancreatic cancer evolution based on genomic rearrangement patterns. Nature *538*, 378–382.

Ohashi, S., Natsuizaka, M., Wong, G.S., Michaylira, C.Z., Grugan, K.D., Stairs, D.B., Kalabis, J., Vega, M.E., Kalman, R.A., Nakagawa, M., et al. (2010). Epidermal growth factor receptor and mutant p53 expand an esophageal cellular subpopulation capable of epithelial-to-mesenchymal transition through ZEB transcription factors. Cancer Res. *70*, 4174–4184.

Parekh, S., Ziegenhain, C., Vieth, B., Enard, W., and Hellmann, I. (2016). The impact of amplification on differential expression analyses by RNA-seq. Sci. Rep. *6*, 25533.

Patra, K.C., Bardeesy, N., and Mizukami, Y. (2017). Diversity of Precursor Lesions For Pancreatic Cancer: The Genetics and Biology of Intraductal Papillary Mucinous Neoplasm. Clin. Transl. Gastroenterol. *8*, e86.

Patra, K.C., Kato, Y., Mizukami, Y., Widholz, S., Boukhali, M., Revenco, I., Grossman, E.A., Ji, F., Sadreyev, R.I., Liss, A.S., et al. (2018). Mutant GNAS drives pancreatic tumourigenesis by inducing PKA-mediated SIK suppression and reprogramming lipid metabolism. Nat. Cell Biol. *20*, 811–822.

Perez-Riverol, Y., Csordas, A., Bai, J., Bernal-Llinares, M., Hewapathirana, S., Kundu, D.J., Inuganti, A., Griss, J., Mayer, G., Eisenacher, M., et al. (2019). The PRIDE database and related tools and resources in 2019: improving support for quantification data. Nucleic Acids Res. *47* (D1), D442–D450.

Poplin, R., Ruano-Rubio, V., Depristo, M.A., Fennell, T.J., Carneiro, M.O., Van Der Auwera, G.A., Kling, D.E., Gauthier, L.D., Levy-Moonshine, A., Roazen, D., et al. (2018). Scaling accurate genetic variant discovery to tens of thousands of samples. bioRxiv. https://doi.org/10.1101/201178.

Puleo, F., Nicolle, R., Blum, Y., Cros, J., Marisa, L., Demetter, P., Quertinmont, E., Svrcek, M., Elarouci, N., Iovanna, J., et al. (2018). Stratification of Pancreatic Ductal Adenocarcinomas Based on Tumor and Microenvironment Features. Gastroenterology *155*, 1999–2013.e3.

Qadir, M.M.F., Álvarez-Cubela, S., Klein, D., van Dijk, J., Muñiz-Anquela, R., Moreno-Hernández, Y.B., Lanzoni, G., Sadiq, S., Navarro-Rubio, B., García, M.T., et al. (2020). Single-cell resolution analysis of the human pancreatic ductal progenitor cell niche. Proc. Natl. Acad. Sci. USA *117*, 10876–10887.

Rahib, L., Smith, B.D., Aizenberg, R., Rosenzweig, A.B., Fleshman, J.M., and Matrisian, L.M. (2014). Projecting cancer incidence and deaths to 2030: the unexpected burden of thyroid, liver, and pancreas cancers in the United States. Cancer Res. *74*, 2913–2921.

Rao, J., Pfeiffer, M.J., Frank, S., Adachi, K., Piccini, I., Quaranta, R., Araúzo-Bravo, M., Schwarz, J., Schade, D., Leidel, S., et al. (2016). Stepwise clearance of repressive roadblocks drives cardiac induction in human ESCs. Cell Stem Cell *18*, 341–353.

Reichert, M., Blume, K., Kleger, A., Hartmann, D., and von Figura, G. (2016). Developmental Pathways Direct Pancreatic Cancer Initiation from Its Cellular Origin. Stem Cells Int. *2016*, 9298535.

Rezania, A., Bruin, J.E., Riedel, M.J., Mojibian, M., Asadi, A., Xu, J., Gauvin, R., Narayan, K., Karanu, F., O'Neil, J.J., et al. (2012). Maturation of human embryonic stem cell-derived pancreatic progenitors into functional islets capable of treating pre-existing diabetes in mice. Diabetes *61*, 2016–2029.

Rhodes, J.A., Criscimanna, A., and Esni, F. (2012). Induction of mouse pancreatic ductal differentiation, an in vitro assay. In Vitro Cell. Dev. Biol. Anim. *48*, 641–649.

Ritchie, M.E., Phipson, B., Wu, D., Hu, Y., Law, C.W., Shi, W., and Smyth, G.K. (2015). limma powers differential expression analyses for RNA-sequencing and microarray studies. Nucleic Acids Res. *43*, e47.

Roberts, N.J., Norris, A.L., Petersen, G.M., Bondy, M.L., Brand, R., Gallinger, S., Kurtz, R.C., Olson, S.H., Rustgi, A.K., Schwartz, A.G., et al. (2016). Whole Genome Sequencing Defines the Genetic Heterogeneity of Familial Pancreatic Cancer. Cancer Discov. *6*, 166–175.

Robinson, J.T., Thorvaldsdóttir, H., Winckler, W., Guttman, M., Lander, E.S., Getz, G., and Mesirov, J.P. (2011). Integrative genomics viewer. Nat. Biotechnol. *29*, 24–26.

Robinson, C., Estrada, A., Zaheer, A., Singh, V.K., Wolfgang, C.L., Goggins, M.G., Hruban, R.H., Wood, L.D., Noë, M., Montgomery, E.A., et al. (2018). Clinical and Radiographic Gastrointestinal Abnormalities in McCune-Albright Syndrome. J. Clin. Endocrinol. Metab. *103*, 4293–4303.

Rosenbaum, D.M., Rasmussen, S.G., and Kobilka, B.K. (2009). The structure and function of G-protein-coupled receptors. Nature *459*, 356–363.

Rowe, R.G., and Daley, G.Q. (2019). Induced pluripotent stem cells in disease modelling and drug discovery. Nat. Rev. Genet. *20*, 377–388.

Rubio-Viqueira, B., Jimeno, A., Cusatis, G., Zhang, X., Iacobuzio-Donahue, C., Karikari, C., Shi, C., Danenberg, K., Danenberg, P.V., Kuramochi, H., et al. (2006). An in vivo platform for translational drug development in pancreatic cancer. Clin. Cancer Res. *12*, 4652–4661.

Salinas-Souza, C., De Andrea, C., Bihl, M., Kovac, M., Pillay, N., Forshew, T., Gutteridge, A., Ye, H., Amary, M.F., Tirabosco, R., et al. (2015). GNAS mutations are not detected in parosteal and low-grade central osteosarcomas. Mod. Pathol. *28*, 1336–1342.

Schaffer, A.E., Freude, K.K., Nelson, S.B., and Sander, M. (2010). Nkx6 transcription factors and Ptf1a function as antagonistic lineage determinants in multipotent pancreatic progenitors. Dev. Cell *18*, 1022–1029.

Schindelin, J., Arganda-Carreras, I., Frise, E., Kaynig, V., Longair, M., Pietzsch, T., Preibisch, S., Rueden, C., Saalfeld, S., Schmid, B., et al. (2012). Fiji: an open-source platform for biological-image analysis. Nat. Methods *9*, 676–682.

Seino, T., Kawasaki, S., Shimokawa, M., Tamagawa, H., Toshimitsu, K., Fujii, M., Ohta, Y., Matano, M., Nanki, K., Kawasaki, K., et al. (2018). Human Pancreatic Tumor Organoids Reveal Loss of Stem Cell Niche Factor Dependence during Disease Progression. Cell Stem Cell *22*, 454–467.e6.

Shain, A.H., Giacomini, C.P., Matsukuma, K., Karikari, C.A., Bashyam, M.D., Hidalgo, M., Maitra, A., and Pollack, J.R. (2012). Convergent structural alterations define SWItch/Sucrose NonFermentable (SWI/SNF) chromatin remodeler as a central tumor suppressive complex in pancreatic cancer. Proc. Natl. Acad. Sci. USA *109*, E252–E259.

Simsek, S., Zhou, T., Robinson, C.L., Tsai, S.Y., Crespo, M., Amin, S., Lin, X., Hon, J., Evans, T., and Chen, S. (2016). Modeling Cystic Fibrosis Using Pluripotent Stem Cell-Derived Human Pancreatic Ductal Epithelial Cells. Stem Cells Transl. Med. *5*, 572–579.

Song, J., and Shi, W. (2018). The concomitant apoptosis and EMT underlie the fundamental functions of TGF-β. Acta Biochim. Biophys. Sin. (Shanghai) *50*, 91–97.

Springer, S., Wang, Y., Dal Molin, M., Masica, D.L., Jiao, Y., Kinde, I., Blackford, A., Raman, S.P., Wolfgang, C.L., Tomita, T., et al. (2015). A combination of molecular markers and clinical features improve the classification of pancreatic cysts. Gastroenterology *149*, 1501–1510.

Subramanian, A., Tamayo, P., Mootha, V.K., Mukherjee, S., Ebert, B.L., Gillette, M.A., Paulovich, A., Pomeroy, S.L., Golub, T.R., Lander, E.S., and Mesirov, J.P. (2005). Gene set enrichment analysis: a knowledge-based approach for interpreting genome-wide expression profiles. Proc. Natl. Acad. Sci. USA *102*, 15545–15550.

Takeuchi, S., Takahashi, A., Motoi, N., Yoshimoto, S., Tajima, T., Yamakoshi, K., Hirao, A., Yanagi, S., Fukami, K., Ishikawa, Y., et al. (2010). Intrinsic cooperation between p16INK4a and p21Waf1/Cip1 in the onset of cellular senescence and tumor suppression in vivo. Cancer Res. *70*, 9381–9390.

Tan, M.C., Basturk, O., Brannon, A.R., Bhanot, U., Scott, S.N., Bouvier, N., LaFemina, J., Jarnagin, W.R., Berger, M.F., Klimstra, D., and Allen, P.J. (2015). GNAS and KRAS Mutations Define Separate Progression Pathways in Intraductal Papillary Mucinous Neoplasm-Associated Carcinoma. J. Am. Coll. Surg. *220*, 845–854.e1.

Tarasov, A., Vilella, A.J., Cuppen, E., Nijman, I.J., and Prins, P. (2015). Sambamba: fast processing of NGS alignment formats. Bioinformatics *31*, 2032–2034.

Tiriac, H., Bucobo, J.C., Tzimas, D., Grewel, S., Lacomb, J.F., Rowehl, L.M., Nagula, S., Wu, M., Kim, J., Sasson, A., et al. (2018). Successful creation of pancreatic cancer organoids by means of EUS-guided fine-needle biopsy sampling for personalized cancer treatment. Gastrointest. Endosc. *87*, 1474–1480.

Traag, V. (2015). louvain-igraph: v0.5.3. https://zenodo.org/record/35117#.YAoEuy337BI.

Tu, Q., Hao, J., Zhou, X., Yan, L., Dai, H., Sun, B., Yang, D., An, S., Lv, L., Jiao, B., et al. (2018). CDKN2B deletion is essential for pancreatic cancer development instead of unmeaningful co-deletion due to juxtaposition to CDKN2A. Oncogene *37*, 128–138.

Tulpule, A., Kelley, J.M., Lensch, M.W., McPherson, J., Park, I.H., Hartung, O., Nakamura, T., Schlaeger, T.M., Shimamura, A., and Daley, G.Q. (2013). Pluripotent stem cell models of Shwachman-Diamond syndrome reveal a common mechanism for pancreatic and hematopoietic dysfunction. Stem Cells Transl Med *8*, 1249–1264.

Villasenor, A., Chong, D.C., Henkemeyer, M., and Cleaver, O. (2010). Epithelial dynamics of pancreatic branching morphogenesis. Development *137*, 4295–4305.

Warlich, E., Kuehle, J., Cantz, T., Brugman, M.H., Maetzig, T., Galla, M., Filipczyk, A.A., Halle, S., Klump, H., Schöler, H.R., et al. (2011). Lentiviral vector design and imaging approaches to visualize the early stages of cellular reprogramming. Mol. Ther. *19*, 782–789.

Wilschanski, M., and Novak, I. (2013). The cystic fibrosis of exocrine pancreas. Cold Spring Harb. Perspect. Med. *3*, a009746.

Wolf, F.A., Angerer, P., and Theis, F.J. (2018). SCANPY: large-scale single-cell gene expression data analysis. Genome Biol. *19*, 15.

Wolf, F.A., Angerer, P., Ramirez, F., Virshup, I., Rybakov, S., Eraslan, G., White, T., Luecken, M., Cittaro, D., Callies, T., et al. (2020). scanpy.tl.rank_genes_groups function. https://github.com/theislab/scanpy/blob/099be48b860388cf6b8b0aa6006311f6f39de712/scanpy/tools/_rank_genes_groups.py#L416-L628.

Wood, L.D., Noë, M., Hackeng, W., Brosens, L.A., Bhaijee, F., Debeljak, M., Yu, J., Suenaga, M., Singhi, A.D., Zaheer, A., et al. (2017). Patients with McCune-Albright syndrome have a broad spectrum of abnormalities in the gastrointestinal tract and pancreas. Virchows Arch. *470*, 391–400.

Wu, J., Matthaei, H., Maitra, A., Dal Molin, M., Wood, L.D., Eshleman, J.R., Goggins, M., Canto, M.I., Schulick, R.D., Edil, B.H., et al. (2011). Recurrent GNAS mutations define an unexpected pathway for pancreatic cyst development. Sci. Transl. Med. *3*, 92ra66.

Xiang, B., and Muthuswamy, S.K. (2006). Using three-dimensional acinar structures for molecular and cell biological assays. Methods Enzymol. *406*, 692–701.

Xie, R., Everett, L.J., Lim, H.W., Patel, N.A., Schug, J., Kroon, E., Kelly, O.G., Wang, A., D'Amour, K.A., Robins, A.J., et al. (2013). Dynamic chromatin remodeling mediated by polycomb proteins orchestrates pancreatic differentiation of human embryonic stem cells. Cell Stem Cell *12*, 224–237.

Xiong, J., Zhao, W.Q., Huang, G.H., Yao, L.H., Dong, H.M., Yu, C.H., Zhao, H.J., and Cai, S.X. (2017). [Receptor for advanced glycation end products upregulates MUC5AC expression and promotes mucus overproduction in mice with toluene diisocyanate-induced asthma]. Nan Fang Yi Ke Da Xue Xue Bao *37*, 1301–1307.

Zecha, J., Satpathy, S., Kanashova, T., Avanessian, S.C., Kane, M.H., Clauser, K.R., Mertins, P., Carr, S.A., and Kuster, B. (2019). TMT Labeling for the Masses: A Robust and Cost-efficient, In-solution Labeling Approach. Mol. Cell. Proteomics *18*, 1468–1478.

Zeman, M.K., and Cimprich, K.A. (2014). Causes and consequences of replication stress. Nat. Cell Biol. *16*, 2–9.

Zhou, Q., Law, A.C., Rajagopal, J., Anderson, W.J., Gray, P.A., and Melton, D.A. (2007). A multipotent progenitor domain guides pancreatic organogenesis. Dev. Cell *13*, 103–114.

Please cite this article in press as: Breunig et al., Modeling plasticity and dysplasia of pancreatic ductal organoids derived from human pluripotent stem cells, Cell Stem Cell (2021), https://doi.org/10.1016/j.stem.2021.03.005

STAR★METHODS

KEY RESOURCES TABLE

REAGENT or RESOURCE	SOURCE	IDENTIFIER
Antibodies		
Secondary antibody anti-mouse-HRP	GE Healthcare	Cat# NA931; RRID:AB_772210
Secondary antibody anti-rabbit-HRP	GE Healthcare	Cat# NA934; RRID:AB_772206
anti-mouse IgG MicroBeads	Miltenyi	Cat# 130-048-402; RRID:AB_244361
Rabbit monoclonal AcTUB	Abcam	Cat# ab179484
Rabbit polyclonal AMY2A	SIGMA	Cat# A8273; RRID:AB_258380
Mouse monoclonal anti-ACTB	Sigma	Cat# A5316; RRID:AB_476743
Rabbit polyclonal C-peptide	Cell Signaling	Cat# 4593; RRID:AB_10691857
Mouse monoclonal CA19-9	Thermo	Cat# CA1003-200UL; RRID:AB_212741
Rabbit monoclonal anti-CA2	Abcam	Cat# ab124687; RRID:AB_10972000
Rat monoclonal CD31	BD Bioscience	Cat# 557355; RRID:AB_396660
Rabbit monoclonal CDX2	Cell Marque - RabMab	Cat# MU392-UC; RRID:AB_2335627
Mouse monoclonal CFTR	R&D	Cat# MAB1660; RRID:AB_2260674
Rabbit polyclonal CLDN1	Abcam	Cat# ab15098; RRID:AB_301644
Mouse monoclonal CTRC	Millipore	Cat# MAB1476; RRID:AB_2261190
Mouse monoclonal PE-conjugated CXCR4 antibody	Life Technologies	Cat# MHCXCR404; RRID:AB_10373097
Mouse monoclonal APC-conjugated c-Kit antibody	Thermo	Cat# CD11705; RRID:AB_2536476
Mouse monoclonal E-CAD	Dako/ Agilent	Cat# M3612; RRID:AB_2341210
Mouse monoclonal E-CAD	BD Bioscience	Cat# 610182; RRID:AB_397581
Rabbit monoclonal E-CAD	Cell Signaling	Cat# 3195; RRID:AB_2291471
Rabbit polyclonal ERK	Cell Signaling	Cat# 9102; RRID:AB_330744
Mouse monoclonal $G\alpha_{s/olf}$ (G-10)	Santa Cruz	Cat# sc-365855; RRID:AB_10842167
Mouse monoclonal GCG	SIGMA	Cat# G2654; RRID:AB_259852
Rabbit polyclonal GFP	Thermo	Cat# A-6455; RRID: AB_221570
Mouse monoclonal GP2	MBL International	Cat# D277-3; RRID:AB_10598500
Mouse monoclonal H-NUCL	Abcam	Cat# ab190710
Mouse monoclonal H2AX (pS139) Clone N1-431-APC	BD	Cat# 560447; RRID:AB_1645414
Rabbit monoclonal HA	Cell Signaling	Cat# 3724; RRID:AB_1549585
Mouse monoclonal HNF1B	Abcam	Cat# ab236759
Rabbit monoclonal Ki67	Thermo	Cat# MA5-14520; RRID:AB_10979488
Mouse monoclonal Ki67	Dako/ Agilent	Cat# M7240; RRID:AB_2142367
Mouse monoclonal KRT7	Dako/ Agilent	Cat# M7018; RRID:AB_2134589
Mouse monoclonal KRT8	BD Bioscience	Cat# 345779; RRID:AB_2800363
Mouse monoclonal KRT19	Dako/ Agilent	Cat# M0888; RRID:AB_2234418
Rabbit polyclonal mCherry	Abcam	Cat# ab167453; RRID:AB_2571870
Mouse monoclonal MUC1	Santa Cruz	Cat# sc-7313; RRID:AB_626983
Mouse monoclonal MUC5AC	Santa Cruz	Cat# sc-33667; RRID:AB_627973
Rabbit monoclonal N-CAD	Cell Signaling	Cat# 13116; RRID:AB_2687616
Rabbit polyclonal NANOG	Cell Signaling	Cat# 3580; RRID:AB_2150399
Mouse monoclonal NKX6-1	Developmental Studies Hybridoma Bank (DSHB)	Cat# F55A12; RRID:AB_532379
Mouse monoclonal NKX6-1-APC	BD	Cat# 563338; RRID:AB_2738144

(*Continued on next page*)

Please cite this article in press as: Breunig et al., Modeling plasticity and dysplasia of pancreatic ductal organoids derived from human pluripotent stem cells, Cell Stem Cell (2021), https://doi.org/10.1016/j.stem.2021.03.005

Continued

REAGENT or RESOURCE	SOURCE	IDENTIFIER
Mouse monoclonal OCT4	Santa Cruz	Cat# sc-5279; RRID:AB_628051
Mouse monoclonal P15	Santa Cruz	Cat# sc-271791; RRID:AB_10709436
Rabbit monoclonal P16	Cell Signaling	Cat# 80772; RRID:AB_2799960
Rabbit monoclonal P21	Abcam	Cat# ab109520; RRID:AB_10860537
Mouse monoclonal P53	Santa Cruz	Cat# sc-47698; RRID:AB_628083
Rabbit monoclonal pERK	Cell Signaling	Cat# 4377; RRID:AB_331775
Rabbit polyclonal PARP	Cell Signaling	Cat# 9542; RRID:AB_2160739
Goat polyclonal PDX1	R&D	Cat# AF2419; RRID:AB_355257
Mouse monoclonal PDX1-PE	BD	Cat# 562161; RRID:AB_10893589
Rabbit polyclonal PKC	Abcam	Cat# ab59364; RRID:AB_944858
Rabbit monoclonal p-PKA substrates (RRXS*/T*)	Cell Signaling	Cat# 9624; RRID:AB_331817
Rabbit monoclonal pRB	Cell Signaling	Cat# 8516; RRID:AB_11178658
Mouse monoclonal RB	Cell Signaling	Cat# 9309; RRID:AB_823629
Rabbit polyclonal SOX9	Millipore	Cat# AB5535; RRID:AB_2239761
Mouse monoclonal SSEA4	Cell Signaling	Cat# 4755; RRID:AB_1264259
Rabbit polyclonal Turbo GFP	Thermo	Cat# PA5-22688 RRID: AB_2540616
Rabbit monoclonal VASP	Cell Signaling	Cat# 3132; RRID:AB_2213393
Rabbit monoclonal VIM	Cell Signaling	Cat# 5741; RRID:AB_10695459
Mouse monoclonal VINC	Sigma	Cat# V9264; RRID:AB_10603627
Rabbit polyclonal Zeb1	Santa Cruz	Cat# sc-25388; RRID:AB_2217979
Mouse monoclonal ZO1	Thermo	Cat# 33-9100; RRID:AB_2533147
Antibody conditions for IHC/IF are listed in Methods S4	This paper	N/A
Bacterial and virus strains		
Lentivirus hOKSM-dTomato	Warlich et al., 2011	N/A
Non-integrating Sendai virus (CytoTuneTM-iPS 2.0 Sendai Reprogramming Kit)	Thermo	Cat# A16517
One Shot ccdB Survival 2 T1R Competent Cells	Thermo	Cat# A10460
Subcloning Efficiency DH5α Competent Cells	Thermo	Cat# 18265017
Biological samples		
Human pancreatic ductal organoids from cadaveric organ donors	Tamara Madácsy, József Maléth (based on Boj et al., 2015)	N/A
FPC patient keratinocytes	This paper	N/A
Human bone marrow stromal cells (HBMSCs)	Natasha Cherman (Pamela G. Robey)	N/A
Transformed human patient-derived organoids (Panc163)	Bruno Sainz, Patrick Hermann (Rubio-Viqueira et al., 2006)	N/A
Untransformed human patient-derived organoids from resection specimen	Maximilian Reichert, Zahra Dantes (Dantes et al., 2020)	N/A
Chemicals, peptides, and recombinant proteins		
3,3,5-Triiodo-L-thyronine	Sigma	Cat# T0281; CAS: 5817-39-0
A-83-01	Tocris	Cat# 2939; CAS: 909910-43-6
Activin A	PeproTech	Cat# 120-14; SDS: 25-120-14
Carbonic anhydrase II from bovine erythrocytes	Sigma	Cat# C2273; CAS: 9001-03-0
CHIR99021	Axon MedChem	Cat# 1386; CAS: 252917-06-9
Choleratoxin	Sigma	Cat# C9903; CAS: 131096-89-4

(*Continued on next page*)

Please cite this article in press as: Breunig et al., Modeling plasticity and dysplasia of pancreatic ductal organoids derived from human pluripotent stem cells, Cell Stem Cell (2021), https://doi.org/10.1016/j.stem.2021.03.005

Continued

REAGENT or RESOURCE	SOURCE	IDENTIFIER
Collagenase/Dispase	Roche	Cat# 11097113001
Collagenase II	Life Technologies	Cat# 17101015
Collagenase IV	Worthington	Cat# LS0004186; CAS: 9007-34-5
Dexamethasone	Sigma	Cat# D1756; CAS: 50-02-2
Dextran, Fluorescein 500,000 MW	Thermo	Cat# D7136
Dispase	Sigma	Cat# D4693; CAS: 42613-33-2
Dorsomorphin	Sigma	Cat# P5499; CAS: 866405-64-3
Doxycycline hyclate (Dox)	Sigma	Cat# D9891; CAS: 24390-14-5
EGF human	R&D	Cat# 236-EG-200
Fatty acid free BSA	Proliant	Cat# 68700; CAS: 9048-46-8
FGF2	Novoprotein	Cat# C046
FGF10	R&D	Cat# 345-FG-250
FGF-Basic	Thermo	Cat# PHG0360
Forskolin (FSK)	Sigma	Cat# F 3917; CAS: 66575-29-9
Gastrin I	Sigma	Cat# G9020; CAS: 10047-33-3
KGF	PeproTech	Cat# 100-19; SDS: 25-100-19
LDN-193189 (= DM3189)	Sigma	Cat# SML0559; CAS: 1062368-24-4
MSC2530818	Selleckchem	Cat# S8387; CAS: 1883423-59-3
Matrigel Basement Membrane Matrix	Corning	Cat# 354234
Matrigel Basement Membrane Matrix Growth Factor Reduced (GFR)	Corning	Cat# 354230
Matrigel hESC-qualified Matrix	Corning	Cat# 354277
N-acetyl-L-cysteine	Sigma	Cat# A7250; CAS: 616-91-1
Nicotinamide (NA)	Sigma	Cat# N0636; CAS: 98-92-0
Noggin murine	PeproTech	Cat# 250-38; SDS: 25-250-38
Nu-Serum IV	Corning	Cat# 355104;
PKA inhibitor H 89 2HCl	Selleckchem	Cat# S1582; CAS: 130964-39-5
Prostaglandin E2	Tocris	Cat# 2296; CAS: 363-24-6
R-Spondin 1 protein	R&D	Cat# 4645-RS
Retinoic acid (RA)	Sigma	Cat# R2625; CAS: 302-79-4
ROCK inhibitor (Y-27632)	Abcam	ab120129; CAS: 129830-38-2
SANT1	Sigma	Cat# S4572; CAS: 304909-07-7
TMT 10-plex	Thermo	Cat# A37725
Wnt3a mouse	PeproTech	Cat# 315-20; SDS: 25-315-20
XtremeGene 9 DNA transfection reagent	Roche	Cat# 6365787001
ZnSO4	Sigma	Cat# Z0251; CAS: 7446-20-0
(-)-Indolactam V	STEMCELL Technologies	Cat# 72312; CAS: 90365-57-4
3-isobutyl-1-methylxanthine (IBMX)	Sigma	Cat# I5879; CAS: 28822-58-4
Critical commercial assays		
Active Ras Pull-Down and Detection Kit	Thermo	Cat# 16117
AllPrep DNA/RNA/miRNA Universial Kit	QIAGEN	Cat# 80224
BCECF, AM	Thermo	Cat# B1170
BP Clonase II enzyme mix	Life Technologies	Cat# 11789020
cAMP-Gs HiRange Kit	Cisbio	Cat# 62AM6PEB
Click-iT EdU Alexa Fluor 647 Assay Kit	Life Technologies	Cat# C10635
Gibson Assembly® Master Mix	New England BioLabs	Cat# E2611
Human Comprehensive Cancer Panel	QIAGEN	Cat# DHS-3501Z
LR Clonase II enzyme mix	Life Technologies	Cat# 11791100
Maxwell RSC Blood Kit	Promega	Cat# AS1400

(*Continued on next page*)

Please cite this article in press as: Breunig et al., Modeling plasticity and dysplasia of pancreatic ductal organoids derived from human pluripotent stem cells, Cell Stem Cell (2021), https://doi.org/10.1016/j.stem.2021.03.005

Continued

REAGENT or RESOURCE	SOURCE	IDENTIFIER
Nextera XT Kit	Illumina	Cat# FC-131-1096
NEBNext Ultra II FS DNA Library Prep Kit	NEB	Cat# E6177
P3 primary cell 4D Nucleofector X Kit S	Lonza	Cat# V4XP-3032
Senescence β-Galactosidase Staining Kit	Cell Signaling	Cat#9860S
SuperSignal West Dura Kit	Thermo	Cat# 34076
Tissue Genomic DNA Purification Mini Prep Kit	Genaxxon	Cat# S5378.0050
Qubit dsDNA HS reagents	Thermo	Cat# Q32851
Deposited data		
lcWGS data	This paper (ENA at EMBL-EBI)	ENA: PRJEB42190
Protein mass spectrometry data	This Paper (PRIDE)	PRIDE: PXD018785
RNA-seq data	This paper (ENA at EMBL-EBI)	ENA: PRJEB38015
Experimental models: cell lines		
Human: HUES8 hESC line (NIH approval number NIHhESC-10-0021)	HSCI iPS Core, Harvard University, Cambridge, MA, USA	hES Cell Line: HUES-8; RRID:CVCL_B207
HUES8-CDKN2A$^{KO/KO}$ (+/− KRAS^{G12D})	This paper	N/A
HUES8-KRAS^{G12D} line	This paper	N/A
HUES8-GNAS^{R201H} line	This paper	N/A
HUES8-Luciferase line (Vector control)	This paper	N/A
Human: H1 ES cells	Wicell Research Institute, Madison, WI, USA	https://www.wicell.org/
CoiPSC (Control iPSC)	This paper	N/A
MAS-GNAS$^{WT/R201C}$ iPSCs	This paper	N/A
MAS-GNAS$^{WT/WT}$ iPSCs	This paper	N/A
Rat embryonic fibroblast (REF)	This paper	N/A
Experimental models: organisms/strains		
NSG mice (strain: NOD.Cg-Prkdc < scid < tm1Wjl > /SzJ GVO)	Charles River	RRID:BCBC_4142
Nod *scid* mice (strain: NOD.Cg-*Prkdc*^{scid}/J)	The Jackson Laboratory	RRID:IMSR_JAX:001303
Oligonucleotides		
Primers for cloning and sequencing are listed in Methods S1	This paper (unless otherwise stated)	N/A
Primers for qPCR are listed in Methods S3	This paper	N/A or QIAGEN Cat#
Recombinant DNA		
pCAS9_GFP plasmid	Kiran Musunuru (Ding et al., 2013)	Addgene plasmid #44719
gRNA cloning vector	George Church (Mali et al., 2013)	Addgene plasmid #41824
pBabe-KRASG12D	Channing Der	Addgene plasmid # 58902
pcDNA3.1+hsGNAS_EE(long)R201H	Franz. Oswald	N/A
pGL4.10[luc2]	Franz Oswald	N/A
pDONR201	Thermo	Cat# 11798-014
Destination vector PB-TAC-ERP2	Kim et al., 2016	Addgene plasmid #80478
PB-TAC-ERP2-(N-HA)KRAS_G12D	This paper	N/A
PB-TAC-ERP2-KRAS_G12D (w/o HA)	This paper	N/A
PB-TAC-ERP2-GNAS_R201H(EE)	This paper	N/A
PB-TAC-ERP2-Luc2	This paper	N/A
Transposase-encoding vector	SBI Biosciences (Rao et al., 2016)	#PB200PA-1
Software and algorithms		
Adobe Illustrator	Adobe	Creative Cloud
Adobe Photoshop	Adobe	Creative Cloud

(*Continued on next page*)

Please cite this article in press as: Breunig et al., Modeling plasticity and dysplasia of pancreatic ductal organoids derived from human pluripotent stem cells, Cell Stem Cell (2021), https://doi.org/10.1016/j.stem.2021.03.005

Continued

REAGENT or RESOURCE	SOURCE	IDENTIFIER
AxioVision software	ZEISS	https://www.micro-shop.zeiss.com/de/de/system/software+axiovision-axiovision+basissoftware-axiovision+software/10221/
"bwa mem"	Heng, 2013	Version 0.7.17
CLC Genomic Workbench	QIAGEN	Version 20.0.3; https://digitalinsights.qiagen.com/products-overview/discovery-insights-portfolio/analysis-and-visualization/qiagen-clc-genomics-workbench/
CRISPOR sgRNA prediction and designing platform	Haeussler et al., 2016	http://crispor.tefor.net/
EnrichR webtool	Ma'ayan lab (Kuleshov et al., 2016)	https://maayanlab.cloud/Enrichr/
Fiji	Schindelin et al., 2012	https://imagej.net/Fiji
"GATK" toolkit	Poplin et al., 2018	Version 4.1.4.1
GraphPad Prism 8	GraphPad Software, San Diego, California USA	https://www.graphpad.com
GSEA software	Broad Institute (Subramanian et al., 2005)	Version 4.0.3; https://www.gsea-msigdb.org/gsea/index.jsp
Imaris 8.1 software	Bitplane AG	https://imaris.oxinst.com/downloads
Interactive Genome Viewer (IGV)	Broad Institute (Robinson et al., 2011)	https://software.broadinstitute.org/software/igv/
Maxquant software	Cox and Mann, 2008	Version v.1.5.7.4; https://www.maxquant.org/
Modde	Umetrics, Sartorius	https://www.sartorius.com/en/products/process-analytical-technology/data-analytics-software/doe-software/modde
Olympus excellence software	Olympus	N/A
Phyton	Python Software Foundation	https://www.python.org/psf/
Python package "scanpy"	Wolf et al., 2018	N/A
Python package "scran"	Lun et al., 2016	N/A
R	The R Project	Version 6.1.7601 https://cran.r-project.org/mirrors.html
R package "CopywriteR"	Kuilman, 2020	Version 2.16.0
R package "DESeq2"	Love et al., 2014	Version 1.18.1
R package "Limma"	Ritchie et al., 2015	https://www.bioconductor.org/packages/release/bioc/html/limma.html
R package "scBio" for Cell population mapping	Frishberg et al., 2019	https://github.com/amitfrish/scBio
R package "sva"	Johnson et al., 2007, Leek et al., 2012	Version 3.34.0
"Sambamba"	Tarasov et al., 2015	Version 0.7.0
Star aligner	Dobin et al., 2013	Version 2.6.1.c; https://github.com/alexdobin/STAR
Trimmomatic	Bolger et al., 2014	Version 0.36 / 0.39; http://www.usadellab.org/cms/index.php?page=trimmomatic
ZEN 3.1 imaging software (blue edition)	Zeiss	N/A
Other		
Biozero BZ-9000 microscope	Keyence	N/A
Dionex Ultimate 3000 HPLC system	Thermo	Cat# 6130-7-Sys-004
Zeiss Axioscope2	Zeiss	N/A
Ibidi-ibiTreat-precoated glass-bottom 24-well μ-plates	IBIDI	Cat# 82406

(*Continued on next page*)

Continued

REAGENT or RESOURCE	SOURCE	IDENTIFIER
Ibidi-ibiTreat-precoated 15-well polymer coverslip bottom μ slides	IBIDI	Cat# 81506
Infinite M1000 pro	Tecan	N/A
Fusion SL system	VILBER	N/A
Human reference proteome	UniProt	UP000005640 (downloaded 22.07.2013); https://www.uniprot.org/proteomes/UP000005640
Human reference genome GRCh38.p13	EMBL-EBI	GCF_000001405.39; https://www.ncbi.nlm.nih.gov/assembly/GCF_000001405.39/
LSM780 NLO confocal microscope	Zeiss	N/A
LSM880 confocal microscope	Zeiss	N/A
LSR II flow cytometer	BD	N/A
NextSeq 500 Sequencing System	Illumina	Cat# 770-2013-053-F
Olympus CKX41	Olympus	N/A
Olympus Cool LED PE-4000 illumination system	Olympus	N/A
Olympus IX73	Olympus	N/A
Orbitrap Fusion Lumos Tribrid mass spectrometer	Thermo	Cat# IQLAAEGAAPFADBMBHQ
Pancreatic progenitor first gene set	Xie et al., 2013	https://doi.org/10.1016/j.stem.2012.11.023
Pancreatic progenitor second gene set	Gerrard et al., 2016	E-MTAB-3928
scRNA-seq data (first ductal gene set)	Enge et al., 2017	GEO: GSE81547
scRNA-seq data (second ductal gene set and ductal subpopulations)	Baron et al., 2016	GEO: GSE84133
scRNA-seq data (ductal subpopulations)	Qadir et al., 2020	https://doi.org/10.1073/pnas.1918314117/-/DCSupplemental.
SteREO Discovery.V12	Zeiss	N/A
Trunk domain gene sets Trunk1/Trunk2	De Lichtenberg et al., 2018	https://doi.org/10.1101/336305
Trunk third gene set	Krentz et al., 2018	https://doi.org/10.1016/j.stemcr.2018.11.008
4D Nucleofector Core Unit	Lonza	Cat# AAF-1002B
4D Nucleofector X Unit	Lonza	Cat# AAF-1002X

RESOURCE AVAILABILITY

Lead contact

Further information and requests for resources and reagents should be directed to the lead contact Alexander Kleger (alexander.kleger@uni-ulm.de).

Materials availability

Plasmids and cell lines generated in this study are available from the lead contact with some restrictions. *piggyBac* expression plasmids can only be provided with a completed Materials Transfer Agreement and the permission of Knut Woltjen, the provider of the original *piggyBac* plasmids. Transfer of hESCs can only be granted if permissions for the intended use are in place according to respective National Authorities and in compliance with the German "Stammzellgesetz." Panc163 cells cannot be further distributed and requests have to be directly addressed to Bruno Sainz.

Data and code availability

The RNA-seq data for this study have been deposited in the European Nucleotide Archive (ENA) at EMBL-EBI under accession number PRJEB38015, and the lcWGS data under PRJEB42190. The mass spectrometry proteomics data have been deposited to the ProteomeXchange Consortium via the PRIDE (Perez-Riverol et al., 2019) partner repository with the dataset identifier PXD018785. The codes supporting the current study are available from the corresponding author on request.

Please cite this article in press as: Breunig et al., Modeling plasticity and dysplasia of pancreatic ductal organoids derived from human pluripotent stem cells, Cell Stem Cell (2021), https://doi.org/10.1016/j.stem.2021.03.005

EXPERIMENTAL MODEL AND SUBJECT DETAILS

Human bone marrow stromal cells

Human bone marrow stromal cells (HBMSCs, a gift from Natasha Cherman) were derived from a female patient with McCune-Albright syndrome. Cells were isolated elsewhere as described in Bianco et al. (1998), and were used to establish *GNAS*$^{WT/WT}$ and *GNAS*$^{WT/R201C}$ induced pluripotent stem cell (iPSC) lines. HBMSCs were cultured in growth medium consisting of α-Minimum Essential Medium (Thermo) supplemented with 20% non-heat inactivated, lot-selected fetal calf serum (FCS, Biochrom), 2 mM L-Glutamine, 1% Penicillin-Streptomycin (P/S), 10 nM Dexamethasone (Sigma) and 100 μM L-Ascorbic acid phosphate magnesium salt n-hydrate (AscP; Wako chemicals) at 37°C and 5% CO_2. Cells were split using 0.05% Trypsin-EDTA (Sigma).

Embryonic and induced pluripotent stem cells

In this study, the human embryonic stem cell (hESC) lines HUES8 (Harvard University; RRID:CVCL_B207) and H1 (Wicell Research Institute) were used. Culture and differentiation of hESCs toward the pancreatic lineage were performed with permission from the Robert Koch Institute according to the "79. Genehmigung nach dem Stammzellgesetz, AZ 3.04.02/0084." HUES8 cell authentication was conducted with a DNA profile using nonaplex PCR of Short Tandem Repeats done by the Leibniz Institute DSMZ. The human control iPSC line Co-iPSC was established in-house from a healthy male donor.

Human ESCs and iPSCs were cultured on hESC Matrigel (Corning) coated plates (according to manufacturer's recommendations) in mTesR1 medium (STEMCELL Technologies) at 5% CO_2, 5% O_2, and 37°C with daily media change. Splitting was done twice a week in a 1:4 – 1:6 ratio. Cells were washed with PBS, incubated with TrypLE (Thermo) for 3-5 min at 37°C for detachment and carefully collected in DMEM-F12+GlutaMAX (GIBCO). After centrifugation at 200 x g for 5 min cells were resuspended in mTesR1 supplemented with 10 μM ROCK inhibitor (Y-27632; Abcam) and seeded again on hESC-qualified Matrigel.

Panc163

Panc163 cells have been previously established from a primary human PDAC xenograft model and were a generous gift from Bruno Sainz (Rubio-Viqueira et al., 2006). Cells were maintained as organoids in a Matrigel-based culture, medium was changed twice a week, and organoids were split every 10 days using Collagenase/Dispase (Roche) and Accutase (Sigma) as described in more detail in the PDLO culture section. For cultivating PDAC organoids, the medium described by Tiriac et al. (2018) was used: DMEM/F12 medium was supplemented with 1x HEPES, 1x GlutaMAX, 1x P/S, 1x B27, 100 μg/ml Primocin (all Thermo), 1.25 mM N-acetyl-L-cysteine (Sigma), 50% Wnt3a-conditioned medium, 10% RSPO1-conditioned medium, 100 ng/ml recombinant Noggin (PeproTech), 50 ng/ml EGF (R&D), 10 nM Gastrin I (Sigma), 100 ng/ml FGF10 (R&D), 10 mM nicotinamide (Sigma), and 500 nM A83-01 (Tocris). Panc163 were used in qPCR, IF and FC analysis, CFTR and CA assay and RNA-seq experiments as control to PDLOs.

Human patient-derived organoids (PDO) from resection specimen

All patients were recruited, enrolled, and consented based on the institutional review board (IRB) project-number 207/15 and 1946/07 of the Technical University Munich. The isolation protocol is detailed in Dantes et al. (2020) and was based on previously described protocols (Moreira et al., 2017; Boj et al., 2015; Biederstädt et al., 2020). To ensure a high take-rate of PDOs, the sample preparation was started within 15 min after receiving the biopsy. Samples were washed (splitting/washing media: Advanced DMEM/F12 with 1x GlutaMAX, 10 mM HEPES and 100 μg/ml Primocin (InvivoGen)) and centrifuged (5 min, 4°C, 1000 rpm). The supernatant was discarded, and the tissue sample was cut into small pieces followed by red blood cell lysis using ACK lysis buffer (Life Technologies) for 10-15 min at RT. The sample was then digested using 5 mg/ml collagenase type II (Life Technologies) for 1-2 h followed by enzymatic digestion (optional) with TrypLE (Life Technologies) for 5-10 min at 37°C. After one washing step, the pellet was mixed with Growth Factor Reduced (GFR)-Matrigel (Corning) and plated as 50 μl Matrigel domes in each well of a prewarmed 24-well plate. After incubation for 20 min at 37°C, 500 μl feeding media was added to each well. Normal feeding media (NFM) contained splitting media supplemented with 1x B27 (Life Technologies), 100 ng/ml recombinant human Wnt3a protein (R&D) or 50% Wnt3a-conditioned medium, 10% R-Spondin 1-conditioned medium or 500 ng/ml recombinant human R-Spondin 1 protein (R&D), 1.25 mM N-acetyl-L-cysteine, 100 ng/ml mNoggin (PeproTech), 100 ng/ml FGF10, 10 nM Gastrin I, 50 ng/ml EGF (Life Technologies), 10 μM ROCK inhibitor (Sigma), 10 mM nicotinamide, 0.5 μM A83-01 (Tocris) and 1 μM prostaglandin E2 (Tocris).

To ensure a non-transformed state of these normal PDOs, whole exome sequencing was performed showing no copy number variants as well as no single nucleotide variants. Due to limited material only RNA could be isolated from three different individuals with a non-transformed state. Such material was used in RNA-seq experiments as control to PDLOs.

Establishment of human ductal organoid cultures derived from organ donors

Isolation and culturing of human ductal organoids was based on Boj et al. (2015): Pancreatic tissue samples from human cadaver donors were transferred in splitting media, composed of Advanced DMEM/F12 with 1x GlutaMAX, 10 mM HEPES and 1x Primocin. Minced tissue pieces were incubated in digestion media (splitting media supplemented with 1250 U/ml collagenase IV (Worthington), 0.5 U/ml dispase (Sigma), 2.5% v/v FBS, and 1 mg/ml trypsin inhibitor (Sigma)) at 37°C in a vertical shaker for approximately 30 min, depending on tissue density. Digestion of the tissue was verified by stereo microscopy every 5 min. Cells were collected by centrifugation in a 15 ml centrifuge tube (750 rpm, 10 min, 4°C). Collected cells were washed by wash media (splitting media with 2.5% v/v FBS, 1x Antibiotic-Antimycotic solution (Sigma), 1x kanamycin (GIBCO) and 2 μg/ml voriconazole (Tocris) two times. The pellet was

Please cite this article in press as: Breunig et al., Modeling plasticity and dysplasia of pancreatic ductal organoids derived from human pluripotent stem cells, Cell Stem Cell (2021), https://doi.org/10.1016/j.stem.2021.03.005

resuspended in washing media and Matrigel in a ratio of 1:5. Matrigel domes (10 μl) were placed in one well of a 24-well cell culture plate and after 10 min of solidification at 37°C, 500 μl feeding media were applied in each well. Feeding media was composed of splitting media supplemented with 50% L-WRN conditioned media, 500 nM A-83-01, 50 ng/ml EGF, 100 ng/ml FGF2 (Thermo), 0.01 μM Gastrin I, 1.25 mM N-acetyl-L-cysteine, 10 mM nicotinamide, 1x B27, 10.5 μM Y-27632, 1 μM prostaglandin E2, 1x Antibiotic-Antimycotic, 1x kanamycin and 2 μg/ml voriconazole. Media change was performed every second day. Domes were pooled and collected by centrifugation (750 rpm, 10 min, 4°C) for passaging during which Matrigel removal and cell separation were performed simultaneously by TrypLE at 37°C for 15 min in a vertical shaker followed by plating the cells in Matrigel as described above. Human pancreatic tissue samples were collected from transplantation donors (Ethical approval No.: 37/2017-SZTE). The herein described human primary organoids were used as controls for intracellular pH measurements as additional confirmation of PDLO functionality.

Mouse model

NOD *scid* gamma (NSG) mice (NOD.Cg-Prkdc^{scid} Il2rgtm1Wjl/SzJ strain (Charles River); RRID:BCBC_4142) were used for xenotransplantation of PDLOs into the pancreas with permission of the "Regierungspräsidium Tübingen" (TVA1406). For xenotransplantation of PDLOs into the ACE, male NOD *scid* mice (NOD.Cg-Prkdc^{scid}/J strain (The Jackson Laboratory); RRID:IMSR_JAX:001303) were used with approval by the Committee on the Ethics of Animal Experiments of the State Directory of Saxony and the Ethics Committee of the Technische Universität Dresden (TVV57/2016). Husbandry was performed in standardized hygiene barrier rooms with reduced pathogen microorganism burden. Animals had an age between 6 to 12 weeks before experiments were started and male and female individuals were distributed equally to the different groups, although gender-specific effects were not expected. Housing was performed in groups of two to four mice per cage.

METHOD DETAILS

Generation of iPSCs by reprogramming

For the generation of MAS-iPSCs, a mixed population of mosaic *GNAS*$^{WT/WT}$/*GNAS*$^{WT/R201C}$ HBMSCs were split using 0.05% Trypsin-EDTA to reach 50%–60% confluency for viral infection after two days. Reprogramming with hOKSM-dTomato lentivirus (Warlich et al., 2011) was performed as previously described (Hohwieler et al., 2017): When 75% confluency was reached on a 6-well, HBMSCs were infected once with 1 × 10^8 viral genome copies of hOKSM-dTomato lentivirus in growth medium supplemented with 8 μg/ml polybrene (Sigma). The next day, cells were detached using TrypLE and transferred in a 1:3 or 1:4 ratio to 6-wells covered with a feeder layer of 3.5 × 10^8 inactivated rat embryonic fibroblast (REF), which were gamma-irradiated with 30 Gy one day before (Linta et al., 2012). After that, cells were further cultured in hiPSC medium containing Knockout DMEM (GIBCO), 20% knockout serum replacement (GIBCO), 100 μM NEAA (Sigma), 2 mM L-Glutamine (GIBCO), 1% Antibiotic-Antimycotic, 100 μM β-Mercaptoethanol (Merck Millipore), 50 μg/ml L-Ascorbic acid (Sigma), 10 ng/ml FGF2 (Novoprotein) and 10 μM ROCK inhibitor with daily media change at 5% CO_2 and 5% O_2. About 14 days later, iPSC colonies with appropriate size were manually picked on irradiated REFs to further expand cells. In the next step, colonies were again manually picked and plated onto Matrigel-coated dishes for feeder-free culture (Illing et al., 2013; Linta et al., 2012). Besides infection with the hOKSM-dTomato virus, in a different approach, HBMSCs were infected by using the CytoTune^{TM}-iPS 2.0 Sendai Reprogramming Kit (Thermo). CytoTune 2.0 KOS (hKlf4, hOct3/4, hSox2, MOI 1), hc-Myc (MOI 1) and CytoTune 2.0 hKlf4 (MOI 0.6) vectors were mixed with 10 μM ROCK inhibitor and 8 μg/ml polybrene in HBMSC medium and added to the cells. The subsequent reprogramming procedure was performed as described above. Generated MAS-iPSC clones were checked for p.R201C mutations by PCR amplification and sequencing (*GNAS*-exon8-fwd, CCAGACCTTTGCTTTAGATTGG (Salinas-Souza et al., 2015); *GNAS*-exon9-rev, CACAGCATCCTACCGTTGAAG) (Wood et al., 2017). Products were sent for Sanger sequencing (Eurofins Genomics).

Genome editing by CRISPR/Cas9 in hESCs

A large deletion in *CDKN2A* was created in the hESC line HUES8 by CRISPR/Cas9 gene editing by induction of two distinct double strand breaks (DSBs) flanking exon 2 and 3 of the *CDKN2A* gene. crRNAs were designed with an open-access online tool (http://crispor.tefor.net; Haeussler et al., 2016: crRNA-*CDKN2A*-exon2, GTAGGGGTAATTAGACACCT; crRNA-*CDKN2A*-exon3, GTCTCGAGTCTATCGATATG. Construct generation of the plasmid-based CRISPR/Cas9 approach was performed as described in Mali et al. (2013): For each target site, respective custom DNA oligonucleotides with complementary sequences were annealed to double stranded oligos using the Phusion Polymerase Reaction Kit (NEB). The gel purified fragment and the AflII-digested gRNA cloning vector (Addgene plasmid # 41824, a gift from George Church; Mali et al., 2013) were combined by Gibson Assembly according to manufacturer's instructions. Competent *E. coli* cells were transformed with the resulting construct, plasmid DNA was purified and checked by PCR and sequencing. The final gRNA expression plasmids for both gRNAs together with a Cas9 nuclease expression plasmid (Addgene plasmid #44719, a gift from Kiran Musunuru; Ding et al., 2013) were used for transfection of HUES8 cells. Therefore, 200,000 cells were seeded on Matrigel-coated 6-wells and after 16 h the transfection mix consisting of 2 μg pCAS9_GFP vector, 2 μg gRNA 1 plasmid, 2 μg gRNA 2 plasmid and 18 μl XtremeGene 9 DNA transfection reagent (Roche) (3:1 ratio) was added dropwise to the cells (see also manufacture's protocol). 48 h post transfection, GFP-positive cells were sorted by FACS and plated at low density (500 cells/10 cm dish) for clonal expansion in media supplemented with 10 μM ROCK inhibitor and 0.5 μM Thiazovivin (Calbiochem). Multiple single cell-derived colonies were picked manually after 10-12 days for screening of gene edited clones.

Please cite this article in press as: Breunig et al., Modeling plasticity and dysplasia of pancreatic ductal organoids derived from human pluripotent stem cells, Cell Stem Cell (2021), https://doi.org/10.1016/j.stem.2021.03.005

Screening of edited clones: DNA isolation and PCR reaction

Clonal colonies were manually dissociated, and one half of the cells was further cultivated and expanded while the other half was used for genotyping. DNA was isolated using the Tissue Genomic DNA Purification Mini Prep Kit (Genaxxon) according to manufacturer's instructions and amplified by RedMastermix (2x) Taq PCR Mastermix (Genaxxon). PCR screening was based on internal and external primer pairs detecting either the WT or mutated target region. An external PCR product from primers flanking the site of deletion was only obtained if the KO occurred (*CDKN2A*KO-external-fwd, GCGCTTGGATATACAGCAGTG; *CDKN2A*KO-external-rev, ACAGGAGCATCTCCCAACC). Internal primers are located within the deleted region and a product indicated the wild-type allele (*CDKN2A*KO-internal-fwd, GGCATTGTGAGCAACCACTG; *CDKN2A*KO-internal-rev, CCTGTAGGACCTTCGGTGAC). PCR products were sent for Sanger sequencing (Eurofins Genomics) for validation of clonal genotypes.

All-in-One piggyBac-system and nucleofection

Dox-inducible $KRAS^{G12D}$, $GNAS^{R201H}$, and vector control overexpression lines were generated using a *piggyBac* (PB) transposon system. For the vector control, a Luciferase (Luc2) construct was introduced. We modified an *All-in-One*-vector previously described by Kim et al. (2016) and introduced cDNA sequences of the target genes, that were amplified by PCR from the plasmids pBabe-KRAS G12D (Addgene plasmid #58902, a gift from Channing Der), pcDNA3.1+hsGNAS_EE(long) R201H and pGL4.10[luc2] (both kindly provided by Franz Oswald). A 2-step PCR approach was performed by first using the following gene-specific primers: for $KRAS^{G12D}$ (attB1-SpeI-HindIII-(N-HA)KRAS_G12D-fwd; attB2-KRAS_G12D-rev), for $GNAS^{R201H}$ (attB1-SpeI-HindIII-GNAS(EE)_R201H-fwd_new; attB2-GNAS_R201H-rev_new), for Luciferase (attB1-Luc2-for; attB2-Luc2-rev). In the second step the generated PCR products were further amplified with attB1/attB2 adaptor primer (Gloeckner et al., 2009) to add the respective sequences necessary for the gateway cloning system. All corresponding sequences are listed in Methods S1. PCR-products were purified with the Wizard SV Gel and PCR Clean-Up System (Promega).

In the next step, PCR fragments were inserted into the pDONR201 vector (Thermo) and finally into the Destination vector PB-TAC-ERP2 (Addgene plasmid #80478, a gift from Knut Woltjen; Kim et al., 2016) by gateway cloning (BP Clonase II/LR Clonase II enzyme mix, Life Technologies) as described by Gloeckner et al. (2009). Correct sequences of the generated plasmids PB-TAC-ERP2-(N-HA) KRAS_G12D, PB-TAC-ERP2-GNAS_R201H(EE) and PB-TAC-ERP2-Luc2 were confirmed by Sanger sequencing (PB-seq-fwd sequencing; PB-seq-rev sequencing; GNAS_AS189-fwd; Luc2_AS215-fwd; Methods S1).

For integration of the transposon elements into the genomic DNA, HUES8 cells were co-transfected with the transposase-expression vector (SBI Biosciences #PB200PA-1; Rao et al., 2016) and the respective targeting vector, either PB-KRAS, PB-GNAS, and PB-Luc2. Nucleofection of HUES8 cells was performed using the 4D Nucleofector (Lonza) and the P3 primary cell 4D Nucleofector X Kit S (Lonza) according to the manufacturer's protocol. In brief, at 70%–80% confluency, cells were harvested using TrypLE and 200,000 cells per reaction were centrifuged at 130 x g for 3 min. Cells were resuspended in P3-solution and plasmids were added in a 3.3:1 ratio of PB- to transposase plasmid with a total amount of 0.5-1 μg DNA. The reaction mix was transferred to the wells of a 16-well Nucleocuvette strip and pulsed with CA-137. mTesR1 with 10 μM ROCK inhibitor was added to the cells and after 3-5 min incubation at 37°C nucleofected cells were transferred to Matrigel-coated 96-wells. Cells with stable integration of the PB expression cassette were enriched by addition of 1 μg/ml puromycin (Sigma) to the media, starting after 24 h.

Pancreatic differentiation

Differentiation of hPSCs into PPs was performed based on previously published protocols (Nostro et al., 2015; Hohwieler et al., 2017). Cells were cultured in basal media (i) BE1: MCDB131 (Thermo) with 2 mM L-Glutamine, 1.174 g/l Sodium bicarbonate (Sigma), 0.8 g/l cell culture tested glucose (Sigma) and fatty acid free BSA (Proliant) in a concentration of 0.1% (BE1a) for d0-d2 or 0.5% (BE1b) for d3-5. (ii) BE3 (from d6): MCDB131 with 2 mM L-Glutamine, 1.754 g/l Sodium bicarbonate, 0.44 g/l cell culture tested glucose (Sigma), 0.5% ITS-X (GIBCO), 44 mg/l L-Ascorbic acid and 2% fatty acid free BSA. 24-well cell culture plates were coated with GFR-Matrigel diluted 1:18 in DMEM-F12+GlutaMAX before 250,000-450,000 cells per well (depending on the cell line) were seeded in mTesR1 with 10 μM ROCK inhibitor. The day after seeding, differentiation was started with 80%–90% cell confluency by washing with PBS (GIBCO) and adding BE1a medium with 100 ng/ml Activin A (PeproTech) and 2 μM CHIR99021 (Axon MedChem). After 24 h cells were cultured in BE1a containing 100 ng/ml Activin A and 5 ng/ml FGF2 (Novoprotein) for 2 days. At d3 of differentiation cells reached DE stage and BE1b medium containing 50 ng/ml FGF10, 0.75 μM Dorsomorphin (Sigma), and 3 ng/ml Wnt3a (PeproTech) was added for three days. From d6 (GTE stage) on BE3 media supplemented with 50 ng/ml FGF10, 200 nM LDN-193189 (Sigma), 0.25 μM SANT-1 (Sigma), 2 μM Retinoic acid (RA; Sigma), and 16 mM glucose was added for 3 days. The last four days of differentiation (PE stage, d9-d13) cells were cultured in BE3 with 100 ng/ml EGF (R&D), 200 nM LDN-193189, 10 mM nicotinamide, 330 nM Indolactam V (STEMCELL Technologies), and 16 mM glucose. Differentiation was performed at 37°C with 5% CO_2 and medium was changed daily.

To standardize differentiation experiments we implemented purity thresholds of 95% CXCR4/cKIT double positive cells at DE stage and 60% of PDX1/NKX6-1 double positive cells at PP stage, measured by FC analysis. If the number of PDX1/NKX6-1 double positive cells at PP stage was less than 60%, Magnetic-Activated Cell Sorting (MACS) using glycoprotein 2 (GP2) as human pancreatic progenitor marker (Cogger et al., 2017) was implemented. In brief, cells were harvested and stained with anti-GP2-Antibody (MBL International, 1:5000) as outlined in the flow cytometry section for surface marker staining with the addition of 10 μM ROCK inhibitor to all buffers. After antibody incubation for 60 min at 4°C, cells were incubated another 15 min at 4°C with anti-mouse IgG MicroBeads (Miltenyi) and sorted according to manufacturer's instructions.

Please cite this article in press as: Breunig et al., Modeling plasticity and dysplasia of pancreatic ductal organoids derived from human pluripotent stem cells, Cell Stem Cell (2021), https://doi.org/10.1016/j.stem.2021.03.005

Compound screens for protocol development

In total, we performed more than ten rounds of compound screenings. Simplified, we applied morphological criteria (pure culture of ring-like organoids lined with one layered epithelium) together with mRNA expression criteria (increase of ductal markers and reduction of progenitor and non-pancreatic markers) as outlined in the results section. For experimental design and interpretation of qPCR data, we implemented a design of experiment approach to model, simulate, and analyze dependencies between the different biological compounds applied at various concentrations. The software tool MODDE was used to predict marker expression for different combinations of tested compounds, which allowed us to retrieve new recipe suggestions for subsequent compound screens. Promising compounds had been always tested in additional experiments and only compounds, which consistently improved morphology and marker expression, are applied in the current protocol. In this protocol 7 out of 20 compounds, tested in phase I, and 4 out of 28 compounds, tested in phase II, are implemented.

Most experiments were performed in duplicate (two wells per condition) and depending on the experiment intermediate stages (d20, d24) and/or the endpoint of differentiation (d30) was analyzed.

Following compounds were tested in phase I in at least one experiment in indicated concentrations: EGF (10-250 ng/ml), FGF10 (10-250 ng/ml), KGF (10-250 ng/ml), MSC2530818 (4 nM-1 μM), nicotinamide (2-50 mM), Y-27632 (10 μM), $ZnSO_4$ (2-50 μM), and ALK5i-II (10 μM), Avagacestat/BMS-708163 (0.1-10 μM), BMP-4 (10 ng/ml), DAPT (0.1-50 μM), FGF1 (20-500 ng/ml), FGF2 (10 ng/ml), IL-V (33-660 nM), LDN-193189 (0.2 μM), Na_2CO_3 (1.5 mg/ml), RA (10 μM), R-Spondin (10% conditioned medium and 500 ng/ml), SANT-1 (0.25 μM), TGF-β (1 ng/ml).

Following compounds were tested in phase II in at least one experiment in indicated concentrations: EGF (5-250 ng/ml), FGF10 (5-250 ng/ml), nicotinamide (2-50 mM), Y-27632 (10 μM), $ZnSO_4$ (0-50 μM), and Activin A (4-100 ng/ml), ALK5i-II (0.2-10 μM), Avagacestat (0.1-10 μM), Axitinib (0.1-10 μM), BMP-4 (0.2-100 ng/ml), BMP-7 (2-1000 ng/ml), CHIR99021 (0.4-10 μM), Dexamethasone (0.025-2.5 μM), FGF1 (12.5-500 ng/ml), FGF2 (10 ng/ml), Follistatin (20-5000 ng/ml), IL-V (66-1650 nM), IWP2 (0.4-10 μM), KGF (4-250 ng/ml), LDN (0.04-1 μM), MSC2530818 (0.05-10 μM), Na_2CO_3 (1.5 mg/ml), Neuregulin-4 (50-500 ng/ml), RA (0.1-100 μM), R-Spondin (10% conditioned medium and 500 ng/ml), Synthaxin/Epimorphin (20-1000 ng/ml), TGF-β (0.1-10 ng/ml), VEGF-164 (4-1000 ng/ml).

PDLO culture

Cell culture plates were coated with undiluted GFR-Matrigel using precooled tips and well plates, distributing the Matrigel in z-movements until the whole well was covered. Pancreatic progenitors on d13 of differentiation were harvested with TrypLE, washed in BE3, and resuspended in phase I differentiation media. 5% GFR was added additionally to the cold media directly before seeding 100,000 cells per 12-well. The above described Matrigel culture was based on Xiang and Muthuswamy (2006). The final PDLO culture medium consisted in phase I (d13-d19) of BE3 supplemented with 10 mM nicotinamide, 10 μM $ZnSO_4$ (Sigma), 10 μM ROCK inhibitor, 50 ng/ml EGF, 50 ng/ml FGF10, 50 ng/ml KGF (PeproTech), and 50 nM MSC2530818 (Selleckchem). In phase II (from d20) BE3 medium contained 10 mM nicotinamide, 10 μM $ZnSO_4$, 50 ng/ml EGF, 50 ng/ml FGF10. Media change was performed twice a week and media were supplemented with 5% GFR-Matrigel.

For splitting and harvesting organoids, cultures were washed with PBS and incubated with 1 mg/ml Collagenase/Dispase in DMEM-F12+GlutaMAX for 2-4 h at 37°C to degrade surrounding Matrigel. Enzymatic reaction was stopped by addition of equal amounts of neutralization solution (DMEM + 1% BSA + 1% P/S). After centrifugation (200 x g, 5 min) and PBS wash, recovered PDLOs were further processed to generate single cell suspensions or directly lysed for RNA or protein extraction. PDLOs were dissolved into single cells by treatment with Accutase (Sigma) for 30 min in a 37°C water bath and intermittent pipetting. Reaction was stopped again with neutralization solution followed by centrifugation. Finally, PDLO cells were resuspended in phase II medium with 10 μM ROCK inhibitor and seeded again as described above or used for FC analysis.

Analysis of phenotypic alterations upon oncogene induction including live-cell imaging

For experiments with inducible transgenic cell lines, PDLOs were split on d27 and treated for 9 days with 5 μg/ml Dox starting from d29. For titration experiments indicated Dox concentrations were applied. PDLOs were harvested on d38 for respective applications. PDLO cultures were imaged 2, 5, 7, and 9 days after Dox treatment on a Keyence Biozero BZ-9000 microscope. Swelling was quantified using the ImageJ-based software Fiji (Schindelin et al., 2012). Therefore, an automated analysis was applied that calculates the area of organoids within one overview bright field image. In addition, the percentage of filled PDLOs was assessed semi-automatically by applying a second algorithm in Fiji. Analysis was performed in three experiments (independently started differentiations) with each experiment performed in triplicate (three wells per condition). To determine the number of protruding organoids, PDLOs showing outgrowth of single cells and areas of mesenchymal-like cells were manually counted per image of an individual well (comprising 60-80 organoids). Four independent experiments performed at least in duplicate were quantified.

Time series of organoid growth to track these cellular changes was recorded with an epifluorescence microscope (Zeiss Axio Observer 7) over a time period of 4 days starting 2 days after Dox addition. Longitudinal imaging was achieved by maintaining the PDLO culture plate on the microscope under 5% CO_2, 85% humidity, and 37°C within a small incubation chamber (PeCon). Fluorescence and bright field images were taken every 3 h with a 5x Zeiss Neofluar objective. Media was replenished after one day. Images were analyzed and videos were compiled using Zeiss ZEN blue imaging software.

Please cite this article in press as: Breunig et al., Modeling plasticity and dysplasia of pancreatic ductal organoids derived from human pluripotent stem cells, Cell Stem Cell (2021), https://doi.org/10.1016/j.stem.2021.03.005

PKA inhibition in PDLOs

PKA inhibitor treatment was initiated two days after cell seeding. PDLO cultures were incubated with 20 μM H89 2HCl (S1582, Selleckchem) or DMSO (1:1250) as negative control for 12 days in ductal medium. Pictures were captured using a Keyence Biozero BZ-9000 microscope and analyzed as detailed above. The mean organoid size was calculated in duplicate (two wells per condition) of three experiments and the PDLO size decrease was estimated relative to the controls.

Preparation of cell extracts and western blot

For protein extraction, cell lysates were generated by incubating cell pellets in RIPA buffer (50 mM Tris pH 7.4 (AppliChem), 150 mM NaCl (Sigma), 1 mM EDTA (AppliChem), 1% NP40 (Fluka), 0.25% Sodium deoxycholate (Sigma), 0.1% SDS (Serva), supplemented with 1 mM PMSF (AppliChem), 1x phosphatase inhibitor and 1x EDTA-free protease inhibitor cocktail (cOmplete; both Roche) for 30 min on ice and vortexing every 10 min. After 8 min centrifugation at 10,600 x g, supernatant containing the protein fraction was collected. Protein concentration was determined using a Bradford reagent (Bio Rad) and equalized amounts of protein lysates were separated on a polyacrylamide gel (BioRad) in SDS-buffer followed by blotting to a methanol-activated Immobilon-P PVDF membrane (Millipore) by using transfer buffer (32 mM glycine, 44 mM Tris, and 20% methanol; Sigma) and the Transblot semidry transfer system (Bio-Rad). Effective protein transfer was confirmed by Ponceau staining (AppliChem) before membrane was blocked with 5% BSA (or 5% Milk) and 0.1% Tween20 (Sigma) in TBS for at least 1 h at RT. Membranes were incubated with primary antibodies diluted in blocking solution overnight (o/n) at 4°C. After washing three times with 0.1% Tween20 in TBS, incubation with secondary antibody anti-mouse-horseradish peroxidase (HRP) or anti-rabbit-HRP (ECL anti-rabbit or mouse IgG, GE Healthcare) was performed for 1 h at RT. For detection of HRP the SuperSignal West Dura Kit (Thermo) together with Chemiluminescence Imaging – Fusion SL system (VILBER) was applied. Quantification of western blot bands was done with the ImageJ-based software Fiji (Schindelin et al., 2012). The following primary antibodies were used: anti-ACTB (Sigma Cat#A5316, 1:5000), anti-CA2 (Abcam Cat#ab124687, 1:1000), anti-E-CAD (Cell Signaling Cat#3195, 1:1000), anti-ERK (Cell Signaling Cat#9102, 1:1000), anti-$G_{\alpha s/olf}$ (G-10) (Santa Cruz Cat#sc-365855, 1:1000), anti-HA (Cell Signaling Cat#3724, 1:1000), anti-N-CAD (Cell Signaling Cat#13116, 1:1000), anti-P15 (Santa Cruz Cat#sc-271791, 1:500), anti-P16 (Cell Signaling Cat#80772, 1:1000), anti-P21 (Abcam Cat#ab109520, 1:1000), anti-PARP (Cell Signaling Cat#9542, 1:1000), anti-pERK (Cell Signaling Cat#4377, 1:1000), anti-pRB (Cell Signaling Cat#8516, 1:1000), anti-p-PKA substrates (RRXS*/T*) (Cell Signaling Cat#9624, 1:1000), anti-RAS (Thermo, Active Ras Pull-Down and Detection Kit, 1:200), anti-RB (Cell Signaling Cat#9309, 1:1000), anti-VASP (Cell Signaling Cat#3132, 1:1000), anti-Vimentin (VIM, Cell Signaling Cat#5741, 1:1000) and Vinculin (Sigma, V9264, 1:1000).

Pull-down assay

Active Ras Pull-Down and Detection Kit (Thermo) was used according to manufacturer's instructions to verify functionality of the cloned $KRAS^{G12D}$ and (N-HA)$KRAS^{G12D}$ constructs based on KRAS GTPase activity. Briefly, transgenic hESC lines $KRAS^{G12D}$ HUES8 or (N-HA)$KRAS^{G12D}$HUES8 were cultured with or without Dox for 24 h, harvested and lysed with the provided lysis buffer supplemented with 1 mM PMSF, 1x phosphatase inhibitor and 1x EDTA-free protease inhibitor cocktail. As additional controls, equal amounts of the lysates (±Dox) were incubated with GTPγS (positive control activating Ras proteins) or GDP (negative control). Fusion protein of GST and Raf1-Ras-binding domain (RBD) linked to the glutathione agarose resin was prepared in spin cups. Then GTP- and GDP-pretreated as well as untreated lysates were added to such spin cups and incubated at 4°C for 1 h with gentle rocking. After washing three times with the included buffer, proteins were released from the resin by addition of 2x SDS sample buffer with β-Mercaptoethanol (Sigma). Samples were separated by SDS-PAGE and blotted on a PVDF membrane as described above. For KRAS protein detection the anti-Ras antibody provided within the kit was used.

cAMP assay

Cyclic AMP (cAMP) in PSCs or PDLOs was detected with the cAMP-Gs HiRange Kit (Cisbio) according to the manufacturer's protocol. HUES8 as well as PDLOs inducibly expressing $GNAS^{R201H}$ were pretreated with Dox (1 μg/ml for hESCs; 3 μg/ml for PDLOs) before performing the cAMP assay. $GNAS^{WT/WT}$ and $GNAS^{WT/R201C}$ iPSCs were used directly. 96-well low volume white microplates (Cisbio) were used and 20,000 cells were seeded per well in DMEM-F12+GlutaMAX. FRET-signal was measured in a homogeneous time resolved fluorescence (HTRF)-compatible plate reader (Infinite M1000 pro, Tecan). The "HTRF Europium cryptate donor/ Red acceptor readout" setup recommendations were used. The assay was performed in technical triplicate (three wells per condition).

Carbonic anhydrase assay

Carbonic anhydrase (CA) activity was measured by a colorimetric assay based on the imidazole-Tris method (Brion et al., 1988) including phenol red as a pH indicator. PDLOs at d30 were harvested with Collagenase/Dispase, washed with PBS, and lysed at 4°C for 30 min in an SDS-free lysis buffer composed of 150 mM NaCl, 50 mM Tris-HCl (Sigma), pH 7.2, 2 mM EDTA (AppliChem), 1% NP40, and protease inhibitors. Analysis was performed with 60 μg protein per sample. A standard curve was established using serial dilutions of carbonic anhydrase II purified from bovine erythrocytes (Sigma). Incubation buffer containing 60 mM imidazole (Sigma), 30 mM Tris base, 1 mM phenol red (Fluka), and 0.1% BSA (pH 9.6) was added to the samples which were then gassed with CO_2 at a constant flow rate. Time was measured until a colorimetric change was observed and CA concentrations were interpolated from the reference standard curve. The assay was performed blinded and each condition was analyzed in

Please cite this article in press as: Breunig et al., Modeling plasticity and dysplasia of pancreatic ductal organoids derived from human pluripotent stem cells, Cell Stem Cell (2021), https://doi.org/10.1016/j.stem.2021.03.005

duplicate (two wells per condition) with repeated-measurements (same lysate was measured twice or three times) in three independent experiments (independently started differentiations).

CFTR assay

The implemented CFTR assay was based on forskolin (FSK)-induced organoid swelling as described previously (Dekkers et al., 2013). PDLOs were split on day 30 and 100,000 cells were seeded per 12-well as described in the PDLO culture section. At d42-d44 PDLOs were incubated with 20 μM FSK and 100 μM 3-isobutyl-1-methylxanthine (IBMX; both Sigma) for 18 h at 37°C. As negative control DMSO (Roth) was added in respective dilution. Directly before and after incubation, pictures of the PDLOs were captured on a Keyence Biozero BZ-9000 microscope with standardized settings. Swelling was quantified with an ImageJ-based automated analysis based on the SIOX segmentation tool. Here, the area/lumen of all organoids within one overview bright field image was measured. The area of the same organoids was calculated at time point 0 h and at time point 18 h to quantify the relative increase of PDLO size. Each condition was analyzed in duplicate (two wells per condition) and at least 400 organoids per condition were included in each of the three independent experiments.

pH measurements via fluorescence microscopy

PDLOs or human primary organoids from cadaveric organ donors were attached to a poly-l-lysine coated cover glass and were incubated in standard HEPES solution with 1.5 μM BCECF-AM (Thermo), a fluorescent pH indicator, for 30 min at 37°C. Cover glasses were transferred to a perfusion chamber mounted on an Olympus IX73 inverted microscope. Dye loaded samples were excited with an Olympus CoolLED PE-4000 illumination system. For BCECF the filter combination was as follows: 434/17 nm and 497/16 nm single-band bandpass filters for excitation (Semrock; P/N: FF01-434/17-25 and FF01-497/16-25, respectively), 511 nm edge single-edge standard epi-fluorescence dichroic beamsplitter (Semrock; P/N: FF511-Di01-25 × 36) and 537/26 nm single-band bandpass filters for emission (Semrock; P/N: FF01-537/ 26-25). The fluorescent signal was captured by a Hamamatsu ORCA-FLASH 4.0 CCD camera trough a 20x water immersion objective (Olympus; NA: 0.8) with a temporal resolution of 1 s. Ratiometric image analysis was performed by Olympus excellence software. For solution composition see Methods S2.

Flow cytometry

Staining of surface marker

At definitive endoderm (DE) stage differentiation efficiency was determined by c-Kit (CD117) and CXCR4 (CD184) marker staining. Therefore, cells were harvested with TrypLE, enzymatic reaction was stopped with FC buffer containing 2% FCS in PBS and washed once with FC buffer (200 x g, 5 min). Cells were blocked for at least 20 min on ice with blocking buffer consisting of 10% FCS in PBS and washed again with FC buffer. After resuspension of the cell pellets in 50 μl FC buffer incubation with PE-conjugated CXCR4 antibody (Life Technologies) was performed on ice for 30 min. In the next step, APC-conjugated c-Kit antibody (Thermo) was directly added and both antibodies were incubated for another 15 min. Samples were washed, resuspended in FC buffer, and filtered using a 50 μm polyamide mesh (Hartenstein). DAPI (Thermo) was added in a concentration of 150 ng/ml to distinguish viable and dead cells during analysis.

Staining of intracellular marker

Differentiation efficiency was analyzed at the pancreatic endoderm (PE) and pancreatic progenitor (PP) stage by FC-based analysis of PDX1 and NKX6-1 expression. PDLOs were harvested as described before (see section "PDLO culture"), washed with PBS (200 x g, 5 min) and fixed on ice for 25 min in 4% PFA in PBS with 100 mM sucrose (both Sigma). Samples were washed twice with PBS and blocked with 5% normal donkey serum (DS, Jackson ImmunoResearch) in 0.1% Triton X-100/PBS for 30 min on ice. After centrifugation (1000 x g, 5 min), cells were resuspended in blocking solution with primary antibodies. Incubation was either performed o/n at 4°C or 90 min on ice if antibodies were directly coupled to a fluorescence protein. Next, the samples were washed three times with 2% DS, 0.1% Triton X-100 in PBS (wash solution) and, if primary antibodies were not directly coupled to a fluorochrome, incubated with Alexa Fluor secondary antibodies (Thermo) for 90 min on ice. Again, cells were washed twice, resuspended in washing solution, and filtered to obtain single cells before measurement.

Following antibodies were used within this study: anti-PDX1 (R&D Cat#AF2419, 1:500), anti-PDX1-PE (BD Cat#562161, 1:35), anti-NKX6-1 (DSHB Cat#F55A12, 1:150), anti-NKX6-1-APC (BD Cat#563338, 1:35), anti-Ki-67 (Thermo Cat#MA5-14520, 1:1000), anti-Ki-67 (Dako Cat# M7240, 1:1000), anti-H2AX (pS139)-APC (BD Cat#560447, 2.5 μl per sample), anti-HA (Cell Signaling Cat#3724, 1:1600), anti-C-peptide (Cell Signaling Cat#4593, 1:100), anti-GCG (Sigma Cat#G2654, 1:500) and anti-Vimentin (Cell Signaling Cat#5741, 1:100).

Cell-cycle analysis (EdU staining)

Cell-cycle was analyzed by FC using the Click-iT EdU Alexa Fluor 647 Assay Kit (Life Technologies). EdU at a concentration of 10 μM was added to the cell cultures 4 h before samples were harvested. Staining was performed following to manufacturer's recommendations, but the volume of antibody/reaction mix was reduced to 200 μl per sample and the next steps were also adapted to 1 ml for washing and 350 μl final resuspension volume. Staining of intracellular markers prior to EdU staining procedure was possible. DNA was stained with 3 μM DAPI to define the different cell-cycle phases.

FC measurement was performed on the LSR II flow cytometer (BD).

Please cite this article in press as: Breunig et al., Modeling plasticity and dysplasia of pancreatic ductal organoids derived from human pluripotent stem cells, Cell Stem Cell (2021), https://doi.org/10.1016/j.stem.2021.03.005

ICC staining

Immunocytochemistry (ICC/IF) staining were performed of cells cultivated and differentiated on Matrigel-coated ibidi-precoated glass-bottom 24-well μ-plates (IBIDI). Cells were washed with PBS, fixed in 4% PFA+100 mM sucrose solution at RT for 20 min, and washed with PBS three times. Quenching was done with 50 mM NH_4Cl (Sigma) for 10 min and wells were washed three times with PBS before permeabilization with 0.1% Triton X-100/PBS was performed. Cells were blocked with 5% normal goat (Jackson ImmunoResearch) or DS in 0.1% Triton X-100/PBS for 45 min and incubated with the primary antibody solution at 4°C o/n. On the next day, cells were washed three times with PBS and incubated with secondary antibodies diluted in blocking solution at RT for 1 h in the dark. After PBS wash, 500 ng/ml DAPI in PBS was added to the cells for 10 min before well-plates were stored in PBS at 4°C prior to imaging. Used antibodies were: OCT3/4 (Santa Cruz Cat#sc-5279, 1:200), NANOG (Cell Signaling Cat#3580, 1:500), SSEA4 (stained without permeabilization step, Cell Signaling Cat#4755, 1:500) and Alexa-conjugated secondary antibodies. Cells on IBIDI-plates were imaged on a Keyence Biozero BZ-9000 microscope.

Transmission electron microscopy

PDLOs were harvested at d30 by degrading surrounding Matrigel either with Collagenase/Dispase or Cell recovery solution (Corning). After collection and several washing steps with PBS to remove residual Matrigel, PDLOs were fixed in 0.1 M phosphate buffer pH 7.3, containing 2.5% glutaraldehyde, 1% sucrose and osmicated for 1 h in 2% OsO_4. Afterward they were dehydrated in graded series of ethanol, contrasted in 2% uranyl acetate and embedded in epoxy resin (Sigma) at 60°C. Thin sections of 70-80 nm were cut with a diamond knife on a Reichert ultramicrotome and collected on 300 mesh grids. The sections were contrasted with 0.3% lead citrate for 1 min and analyzed on the transmission electron microscope EM 10 (Zeiss) at 80 kV. Sample embedding and processing were carried out by the Central Electron Microscopy Unit at Ulm University.

RNA isolation, reverse transcription and qPCR

RNA extraction was performed with the GeneJET RNA Purification Kit (Thermo) according to manufacturer's instructions. Reverse transcription of 500-1000 ng of total RNA was done with the iScript cDNA Synthesis Kit (Bio-Rad) and cDNA was utilized for quantitative real-time PCR (qPCR) with SensiMix SYBR No-ROX Kit (Bioline) on the QuantStudio 3 Real-Time PCR System (Thermo). Self-designed or commercially available QuantiTect (QIAGEN) qPCR primers of target genes are listed in Methods S3. Hydroxymethylbilane synthase (HMBS) was used as endogenous reference gene for normalization with the $2^{-\Delta\Delta Ct}$ method. RNA values were normalized to the control treated samples of each experiment. For heatmap generation the relative RNA expression of EMT-associated genes was additionally scaled by the sum of each row.

RNA-seq experiments

RNA was isolated from different days of differentiation (d0, d3, d13, d20, d24, d30, d45, and d59) and from Panc163 cells as described above. For each condition, RNA samples from three different wells were sequenced. For non-transformed human patient-derived ductal organoids from resection specimens, RNA was isolated from three independent lines using the AllPrep DNA/RNA/miRNA Universal Kit (QIAGEN) according to the manufacturer's instructions. Library preparation for bulk 3′-sequencing of poly(A)-RNA was done as described previously (Parekh et al., 2016). Briefly, barcoded cDNA of each sample was generated with a Maxima RT polymerase (Thermo) using oligo-dT primer containing barcodes, unique molecular identifiers (UMIs) and an adaptor. 5′ ends of the cDNA were extended by a template switch oligo (TSO); after pooling of all samples, full-length cDNA was amplified with primers binding to the TSO-site and the adaptor. cDNA was tagmented with the Nextera XT Kit (Illumina) and 3′ end-fragments finally amplified using primers with Illumina P5 and P7 overhangs. In comparison to Parekh et al. (2016), the P5 and P7 sites were exchanged to allow sequencing of the cDNA in read1 and barcodes and UMIs in read2 to achieve a better cluster recognition. The library was sequenced on a NextSeq 500 (Illumina) with 75 cycles for the cDNA in read1 and 16 cycles for the barcodes and UMIs in read2.

Full proteome measurement

In-solution digest

Protein was isolated from PPs (d13) and PDLOs (d59) from three different wells per condition (n = 3). After harvesting and washing twice with PBS, cells were lysed in urea lysis buffer (8 M urea, 40 mM Tris (pH 7.6), 1x EDTA-free protease inhibitor and 1x phosphatase inhibitor (in-house, composition resembling phosphatase inhibitor cocktail 1, 2 and 3; Sigma)) for 10 min. After lysing, protein concentration was determined from the cell-free supernatant (20 min, 20,000 x g, 4°C) via Bradford protein assay (Pierce Coomassie Plus (Bradford) Assay Kit; Thermo). 100 μg protein of each sample was further digested. Here, samples were first reduced with 10 mM DTT for 45 min at 37°C at 700 rpm on a Thermoshaker and then alkylated with 55 mM chloroacetamide (CAA) for 30 min at RT in the dark. After diluting the samples < 1.6 M urea with 40 mM Tris (pH 7.6) and 2 mM $CaCl_2$, trypsin (Trypsin Sequencing Grade; Roche) was added 1:100 (enzyme:protein) and incubated for 3 h at 37°C and 700 rpm. After the pre-incubation, trypsin was added again 1:100 (enzyme:protein) and incubated o/n at 37°C and 700 rpm.

SepPak desalting

On the next day, samples were acidified with formic acid (FA) to pH 2-3 and further desalted using 50 mg Sep-Pak columns (Waters Corp.). The columns were first wetted with 100% acetonitrile (ACN), followed by 0.1% FA in 50% ACN and further equilibrated with three washes of 0.1% FA. The samples were slowly loaded onto the column and the flow-through was reloaded onto the column to

Please cite this article in press as: Breunig et al., Modeling plasticity and dysplasia of pancreatic ductal organoids derived from human pluripotent stem cells, Cell Stem Cell (2021), https://doi.org/10.1016/j.stem.2021.03.005

increase peptide binding. After washing off unspecific binders with three times 0.1% FA, peptides were eluted using 2x150 μl of 0.1% FA in 50% ACN. Samples were frozen at −80°C and dried using a Speed-Vac.

TMT labeling

TMT10-plex labeling was performed as previously described (Zecha et al., 2019). Briefly, 45 μg of peptides (measured on Nanodrop) were reconstituted in 20 μl of 50 mM HEPES (pH 8.5) and 5 μl of 11.6 mM TMT 10-plex (Thermo) in 100% ACN was added to each sample. After 1 h incubation at 25°C and 400 rpm, the reaction was stopped using 2 μl of 5% hydroxylamine. All TMT labeled samples were pooled. Remnants in sample vessels were rinsed with 20 μl of 10% FA in 10% ACN for 5 min and 400 rpm and added to pooled samples. The samples were frozen at −80°C and dried using a Speed-Vac.

Sep-Pak desalting

Pooled samples were again desalted using 50 mg Sep-Pak columns (Waters Corp.). The columns were first wetted with 100% ACN, followed by 0.1% FA in 50% ACN and further equilibrated with three washes of 0.1% FA. The dried pooled samples were reconstituted in 1 mL of 0.1% FA and loaded twice onto the column. After washing columns three times with 0.1% FA, peptides were eluted using 200 μl of 0.1% FA in 50% ACN. Samples were frozen at −80°C and dried using a Speed-Vac.

HpH reversed phase fractionation

For high pH reversed phase fractionation, dried samples were reconstituted in MS-grade water with 10% fractionation buffer A (25 mM ammonium bicarbonate (pH 8)) and centrifuged for 5 min at 20.000 x g and 4°C. The supernatant was then loaded on a C18 column (XBridge BEH130, 3.5 μm, 2.1 x 150 mm, Waters Corp), which was connected to a Dionex Ultimate 3000 HPLC system (Thermo). After injecting 100 μg peptides at a flow rate of 200 μg/min, the system was equilibrated for 5 min with 85% fractionation buffer B (MS-grade water), 10% fractionation buffer A and 5% fractionation buffer C (ACN). Peptides were eluted in a three-step linear gradient from 5% to 7% buffer C in 1 min with a constant amount of 10% buffer A. Then, a linear gradient from 7% to 42% buffer C in 44 min and from 42% to 80% buffer C in 6 min (with buffer A being constant at 10%) was used.

Starting from minute 3, 48 fractions (1 fraction/min) were collected in a 96-well plate and pooled to 24 fractions. For that, column 4 was pooled to column 1, column 5 was pooled to column 2 and column 6 was pooled to column 3. All fractions were frozen at −80°C and dried using a Speed-Vac.

LC-MS/MS data acquisition

Fractionated samples were measured in data-dependent acquisition mode using a nanoflow LC-MS/MS by coupling a Dionex Ultimate 3000 UHPLC+ system to a Fusion Lumos Tribrid mass spectrometer (Thermo). Dried samples were reconstituted in 0.1% FA and approximately 200 ng peptides were inserted. The sample was loaded to a trap column (75 μm x 2 cm, packed in-house with 5 μm C18 resin; Reprosil PUR AQ, Dr. Maisch, Ammerbruch-Etringen, Germany) with a flow rate of 5 μl/min and washed for 10 min with 0.1% FA. Subsequently, peptides were separated on an analytical column (75 μm x 40 cm, packed in-house with 3 μm C18 resin; Reprosil PUR AQ, Dr. Maisch, Ammerbruch-Etringen, Germany) with a flow rate of 300 nl/min and a linear 50 min gradient from 8% to 34% LC buffer B (0.1% FA, 5% DMSO in ACN) in LC buffer A (0.1% FA, 5% DMSO in MS-grade water). The eluate was sprayed via a stainless-steel emitter into the mass spectrometer, which was run in positive ion mode. Fullscan MS1 spectra were accorded in the Orbitrap with 60,000 resolution and a scan range from 360-1300 m/z (automatic gain control target of 4e5 charges, maximum injection time of 50 ms). A cycle time of 2 s and a dynamic exclusion of 90 s was used. MS2 spectra were recorded in the Ion Trap in rapid mode via sequential isolation of up to 10 precursors and the following settings: an automatic gain control target of 2e4, maximum injection time of 60 ms, isolation window of 0.7 m/z, and fragmentation via CID (NCE of 35%). For the following MS3 scan the ten most intense precursors were further fragmented via HCD (NCE of 55%) and acquired in the Orbitrap with 50,000 resolution, scan range of 100-1,000 m/z, automatic gain control target of 1.2e5 charges, maximum injection time of 120 s and a charge-dependent isolation window from 1.3 (2+) to 0.7 (5-6+).

Transplantation into the ACE

Suspension cultures of PPs and PDLOs were generated in preparation for the ACE injection. To generate PP-spheroids, cells at the PE-stage (d9 of the differentiation) were detached with TrypLE for 5-6 min resulting in clumps of 3 to 10 cells. After centrifugation at 400 rpm for 5 min the pellet was washed in BE3 medium and resuspended in d9 medium (detailed above) supplemented with 10 μM ROCK inhibitor. Cells were replated into suspension on an ultra-low attachment (ULA) plate and further cultivated in differentiation medium until d13. PDLOs in Matrigel were scraped off from the culture plate at d23, directly resuspended and washed in cold BE3 medium, and transferred in a ULA plate in PDLO medium with 10 μM Y-27632 for shipping. Transplantation of organoid clusters to the anterior chamber of the eye (ACE) and *in vivo* imaging was performed as previously described (Chmelova et al., 2015). Briefly, mice were anesthetized by inhalation of 2% isoflurane in 100% oxygen via a face mask. A 25-gauge needle was used to make a small incision in the cornea, close to the corneal limbus, and 10-15 organoids in PBS were slowly injected into the ACE, using a custom-made beveled glass cannula (outer diameter, 0.4 mm; inner diameter, 0.32 mm; Hilgenberg). For *in vivo* imaging, mice were intubated and anesthetized with 2% isoflurane in 100% oxygen. A drop of 0.4% pilocarpine (Pilomann; Bausch & Lomb) in saline was placed on the cornea shortly before imaging to limit pupil dilation and iris movement. Animals were fixated and kept on a heating pad during the imaging procedure. Repetitive *in vivo* imaging was performed at indicated time points on an upright laser scanning microscope (LSM780 NLO; Zeiss) with a water dipping objective (W Plan-Apochromat 20 × /1.0 DIC M27 75 mm; Zeiss) using vidisic eye gel (Bausch & Lomb) as immersion. Z stacks of entire organoids were acquired at 1.5 μm intervals by detection of 633 nm laser back-scatter. Additionally, FITC-Dextran (0.2 mg/ml in 100 μl PBS, Thermo) was injected into the tail vein to visualize blood vessels. Dextran was excited at 488 nm and detected at 468-607 nm. Z stacks were processed using Imaris 8.1 software (Bitplane AG)

Please cite this article in press as: Breunig et al., Modeling plasticity and dysplasia of pancreatic ductal organoids derived from human pluripotent stem cells, Cell Stem Cell (2021), https://doi.org/10.1016/j.stem.2021.03.005

and Fiji. Mice were sacrificed and eyes were collected 5 weeks after PDLO engraftment. Tissue specimens were fixed in 4% phosphate-buffered paraformaldehyde for 30 min at RT and then incubated in 25% sucrose solution o/n at 4°C. Eyes were embedded in Tissue-Tek OCT (Sakura Finetek) compound and snap-frozen in liquid nitrogen.

Orthotopic transplantation of PDLOs

For xenotransplantation of PDLOs into the pancreas, NSG mice were used. PDLOs between d27 and d31 were harvested and singularized as described above. After washing in BE3 medium, PDLO cells were resuspended in PDLO medium phase II supplemented with 20 μM Y-27632 and GFR-Matrigel in a 1:1 ratio. Aliquots with cell/Matrigel mixture were kept on ice until applied for transplantation.

Mice were pain mediated starting three days before transplantation by addition of 1 mg/ml Tramadol (Grünenthal) to the drinking water. After anesthesia with isoflurane the transplantation site was disinfected with skin antiseptic. A small 0.8 cm long cutaneous midline incision was made and subsequently a small subcutaneous pocket was prepared. After a 0.8 cm small incision into the peritoneum, the pancreas was mobilized and exposed. A volume of 40-50 μl with 0.5-1 x10^6 PDLO cells was injected per mouse directly into the pancreatic tail. Carefully, pancreas and spleen were repositioned in the abdomen before the peritoneum was closed by medical sewing using 5-0 polyglactin coated vicryl suture (Ethicon). Surgical staples were used for closing the skin and removed one week after transplantation, when also Tramadol treatment was stopped. For oncogene induction, Dox was added in a final concentration of 400 μg/ml to the drinking water supplemented with 5% sucrose starting the day of transplantation. Mice were sacrificed after eight weeks and pancreata were collected and processed for histological analysis. Similarly, as described in the paraffin embedding of PDLOs section, tissue samples were fixated, dehydrated, embedded, sectioned, and mounted.

All animal experiments were performed in compliance with the institutional guidelines, under ethical and animal protection regulations of Ulm University.

Paraffin embedding of PDLOs

PDLO cultures were washed with PBS and 4% PFA with 100 mM sucrose was directly added to the wells for fixation. After incubation at 4°C o/n, PFA was removed carefully and PDLOs were washed twice with PBS. By scratching with a pipet tip, all organoids were removed from the well, transferred to a tube and centrifuged at 1000 x g for 3 min. Samples were pre-embedded in 2% agarose (Sigma) and further processed according to standard histology procedures. After serial dehydration, PDLOs as well as pancreas tissue samples were embedded in paraffin and sectioned at 4 μm. Tissue slices were mounted on SuperFrost Ultra Plus microscope slides (Thermo).

Histological standard techniques

Histological staining including Hematoxylin and Eosin (H&E) staining as well as Alcian Blue (AB) and Alcian Blue+Periodic Acid-Schiff reaction (AB+PAS) were performed according to standard protocols. In brief, after deparaffinization and hydration AB staining was done by incubating 3 min in 1% acetic acid solution (Sigma), 5 min in Alcian Blue (Roth) and rinsed shortly first with 1% acetic acid solution and then with tap water. Nuclei were counterstained with 0.1% Nuclear Fast Red solution (Merck) for 10 min and washed with dH_2O. After dehydration slides were embedded in Entellan (Merck).

For AB+PAS staining procedure was identical but after washing with 1% acetic acid solution and tap water another short washing step with dH_2O was necessary before incubation with periodic acid solution (Sigma) was performed for 5 min. Slides were rinsed three times in dH_2O, incubated in Schiff's reagent (Merck) for 15 min and washed with running tap water for 5 min. Finally, 20% Haematoxylin was applied for 90 s, slides were washed with running tap water for 5 min, dehydrated and embedded in Entellan.

IF and IHC staining on paraffin tissue sections

Paraffin sections of PDLOs or pancreatic tissue were rehydrated in ethanol series followed by either heat-mediated or enzymatic antigen retrieval, depending on the antibody (Methods S4). Commercial Tris buffer (pH 9) or Citrate buffer (pH 6, both Vector Laboratories) were used for heat mediated antigen retrieval in the microwave or steamer, while a self-made Citrate buffer (pH 6, 1.9 g/l citric acid; Sigma) was used in the pressure cooker. For enzymatic antigen retrieval, sections were treated with 0.05 mg/ml pronase (Sigma) for 30 min at 37°C.

To continue with immunofluorescence (IF) staining, tissue permeabilization was performed with 0.5% Triton X-100/PBS (PBS-T) for 30 min at RT. After washing twice, primary antibodies diluted in Antibody Diluent (Zytomed) were added to the slides, which were then incubated o/n at 4°C in a wet chamber. After washing three times with PBS-T for 5 min, slides were stained with Alexa Fluor secondary antibodies (Thermo) and 500 ng/ml DAPI diluted in Antibody Diluent for 90 min at RT in the dark. Slides where washed three times with PBS-T and finally with dH_2O before sections were mounted with Fluoromount-G (SouthernBiotech).

For immunohistochemistry (IHC) staining, antigen retrieval was directly followed by incubation with primary antibody solution for 30 min at RT in a wet chamber. Slides were washed and antibody detection was performed applying the Dako Detection Kit (ABC, Dako); different secondary antibodies were used to detect goat or rat IgGs (Vector Laboratories). In brief, slides were incubated first with a biotinylated secondary antibody, washed and next incubated with Streptavidin both for 30 min at RT. After another washing step, slides were incubated with Red Detection Dye for 3-16 min depending on antibody recommendation, counterstained with 20% Hematoxylin solution (Merck) for 30 s, washed with tap water for 5 min and finally mounted with Aquatex (Merck).

Please cite this article in press as: Breunig et al., Modeling plasticity and dysplasia of pancreatic ductal organoids derived from human pluripotent stem cells, Cell Stem Cell (2021), https://doi.org/10.1016/j.stem.2021.03.005

IF staining on cryo sections

PDLOs were frozen in Shandon Cryomatrix (Thermo) and stored at −20°C as described previously (Molnár et al., 2020). Cyrosections of 7 μm thickness were cut, fixed in 4% PFA-PBS and washed in 1x TBS. For staining of CFTR (Alomone) and Occludin (Thermo) (Methods S4), antigen retrieval was performed in Sodium Citrate/Tween20 buffer (0.001 M Sodium Citrate Buffer, pH 6.0 and 0.05% Tween20) at 94°C for 30 min. During antigen retrieval, the slide was placed in a glass flask and the temperature was controlled on a heating block with a thermometer. Sections were blocked with 0.1% goat serum and 10% BSA-TBS for 1 h. Incubation with primary antibodies was performed o/n at 4°C. Incubation with Alexa Fluor secondary antibodies was performed at RT for 2 h. Sections were sealed with ProLong Gold Antifade Mounting Medium with DAPI (Thermo) then left to dry. Images were captured with a Zeiss LSM880 confocal microscope using a 40x oil immersion objective (Zeiss, NA: 1.4).

IF analysis of the eyes was performed on serial cryo sections of 8 μm. Frozen tissue slices were rehydrated for 10 min with PBS and quenched for 15 min using 100 mM Glycine (Sigma). Permeabilization and blocking were performed in 5% DS and 2% BSA in PBS-T (0.05% Tween20 in PBS) for 1 h. Subsequently, tissue sections were incubated with the primary antibodies diluted in 5% BSA/0.2% Triton X-100/PBS o/n at 4°C. Slides were washed three times for 5 min each with PBS-T followed by incubation with the secondary antibody solution supplemented with, 500 ng/ml DAPI for 1 h. Again, slides were washed, twice with 0.2% Triton X-100/PBS and once with PBS for 10 min each, and sections were mounted with Fluoromount-G. Fluorescence images were acquired on a Zeiss Axioscope2 microscope with ApoTome and Axiovision software was used for analysis. Imaging of IHC staining was performed with Olympus CKX41 microscope. Specific staining conditions for each antibody are listed in Methods S4.

β-Galactosidase staining

Organoids were washed with PBS and fixed in 4% PFA with 100 mM sucrose for 30 min at RT. Organoids were removed from the well by scratching with a pipet tip and transferred to a tube. After centrifugation at 1000 x g for 3 min supernatant was removed and organoids were incubated in 25% sucrose solution o/n at 4°C with rotation. After embedding in Tissue-Tek OCT compound, samples were frozen and stored at −80°C until serial cryo sections of 8 μm thickness were cut. Staining was done with the Senescence β-Galactosidase Staining Kit (Cell Signaling) according to manufacturer's instructions. In brief, staining solution was freshly prepared, adjusted to pH between 5.9 and 6.1 and added onto the slides. After incubation o/n (14-16 h), slides were carefully washed with PBS, mounted with Aquatex and finally imaged with an Olympus CKX41 microscope.

Processing of images

Most BF, H&E, IHC, and IF images were cropped and brightness and contrast were modified using Photoshop or ImageJ for improved illustration. For IF staining, the single channels were modified, and compositions were created afterwards. All modifications were applied to the whole image and modified images clearly reflect the original images.

DNA isolation of FFPE tumor tissue

Tumor tissue ($KRAS^{G12D}$ PDAC 1 and $CDKN2A^{KO/KO}$ $KRAS^{G12D}$ PDAC I, III) was isolated from formalin-fixed paraffin embedded (FFPE) tissue by microdissection using fine needles. DNA was isolated from that tissue with an adapted version of the Maxwell RSC Blood Kit (Promega). Briefly, FFPE tissue was incubated in incubation buffer (Promega) for 10 min at 80°C under agitation. After cool-down on ice, ProteinaseK (20 mg/ml, Sigma) was added and samples were incubated o/n at 65°C with gentle agitation. Subsequently, lysis buffer (Promega) was added and samples were incubated for 30 min at 65°C, cooled down on ice, and further processed on a Maxwell RSC instrument according to manufacturer's instructions. Eluted DNA was quantified using Qubit dsDNA HS reagents (Thermo Fisher).

Low coverage whole genome sequencing (lcWGS) of hESC lines and FFPE tissue

DNA isolated from FFPE tumor tissue was sequenced together with DNA from their respective parental cell line (HUES8 $KRAS^{G12D}$ and HUES8 $CDKN2A^{KO/KO}$ $KRAS^{G12D}$). In addition, HUES8 cells prior to *piggyBAC* gene editing were sequenced. Library preparation was performed with 50-200 ng DNA per sample using the NEBNext Ultra II FS DNA Library Prep Kit for Illumina following the manufacturer's instructions. An adapted library preparation protocol was used for low-input (< 50 ng) or FFPE-isolated DNA. In this case, AMPure XP bead purification was omitted after adaptor ligation and all DNA bound to AMPure XP beads (reaction volume:bead ratio: 0.8) directly eluted into PCR Mastermix. Further, denaturation, annealing and extension cycle number was varied according to DNA input (50-200 ng DNA: 4 cycles, < 50 ng DNA/ FFPE: 6 cycles). Samples were sequenced on NextSeq 500 (Illumina), resulting in ~20 Mio. single-end, 75 bp long, reads per tumor sample and ~10 Mio. reads per parental cell lines. Resulting reads were trimmed using "Trimmomatic" [version 0.39] (Bolger et al., 2014) and mapped to the human reference genome GRCh38.p12 using "bwa mem" [version 0.7.17] (Heng, 2013). "Sambamba" [version 0.7.0] (Tarasov et al., 2015) was used to identify read duplicate and the "GATK" toolkit [version 4.1.4.1] (Poplin et al., 2018) was used for base recalibration. Data from the parental hESC lines served as control for calling of somatic copy number alterations using the "CopywriteR" [version 2.16.0] package in R (Kuilman, 2020) (window size: 20kb, otherwise default settings). Raw sequencing data are available under the accession number PRJEB42190. Copy number alterations with a cut-off of $\log_2$ (PDAC/parental cell line) $\geq$ |0.75| can be found in Table S4.

Please cite this article in press as: Breunig et al., Modeling plasticity and dysplasia of pancreatic ductal organoids derived from human pluripotent stem cells, Cell Stem Cell (2021), https://doi.org/10.1016/j.stem.2021.03.005

Cancer-panel sequencing

DNA from CDKN2A$^{KO/KO}$ KRAS^{G12D} PDAC II was isolated as described above with the difference that laser microdissection was performed instead of fine-needle microdissection. DNA was subsequently sequenced with a targeted sequencing approach using QIAseq V3 chemistry (QIAGEN) and the Human Comprehensive Cancer Panel (QIAGEN). Target enrichment, amplicon processing, and library generation were performed according to the manufacturer's instructions. For target enrichment, we included 40 ng genomic DNA. Successful target enrichment and library generation was controlled using the High Sensitivity DNA kit on a bioanalyzer device (Agilent). Libraries were diluted to 10 pM solutions and sequencing was performed on a MiSeq platform (Illumina) using a V3 FlowCell. The resulting FASTQ files were further analyzed to identify somatic mutations using a common workflow in the CLC Genomic Workbench [version 20.0.3] (QIAGEN). The mean read depth on target regions was about 3000-fold, and 95% of bases reached a UMI depth of > 100x. All identified mutations were manually reanalyzed using the Integrated Genome Viewer Software (Broad Institute) (Robinson et al., 2011; Cho et al., 2012). The parental cell line was Sanger-sequenced (Eurofins Genomics) for the identified P53^{S94P} mutation and no mutation could be detected in the parental cell line.

QUANTIFICATION AND STATISTICAL ANALYSIS

Statistical analysis

In general, data summarize three independent experiments (independently started differentiations) with each analysis performed in duplicate (two wells per condition), unless otherwise stated.

Statistical analysis was performed using the GraphPad Prism 8 software, if not stated elsewise, and detailed information regarding the different applied tests are indicated in the figure legends. Statistical significance was defined as follows: * P value < 0.05, ** P value < 0.01, *** P value < 0.001, **** P value < 0.0001.

RNA-seq data analysis

Processing and generation of DEG lists

Raw sequencing data are available under the accession number PRJEB38015. Gene annotations of the human reference genome GRCh38 were derived from the Gencode homepage (EMBL-EBI). "Dropseq tool" [version 1.12] (Macosko et al., 2015) was used for mapping raw sequencing data to the reference genome. The resulting UMI filtered count matrix was imported into R [version 3.4.4]. Prior differential expression analysis with "DESeq2" [version 1.18.1] (Love et al., 2014), dispersion of the data was estimated with a parametric fit using the day of differentiation (d0, d3, d13, d20, d24, d30, d45, d59, and ductal controls) as covariate in the model matrix.

The Wald test was used for determining differentially regulated genes between all pairwise group comparisons and shrunken $\log_2$ fold changes were calculated afterward, with setting the type argument of the "lfcShrink" function to "apeglm" (Pairwise comparisons are listed in Table S2). A gene was determined to be differentially regulated if the absolute $\log_2$ fold change was at least 2 and the adjusted P value was below 0.01.

Deviating from this setting, the absolute $\log_2$ fold change threshold was set to 1 while keeping the same alpha level for comparisons between d20 versus d13 and d59 versus d30, and the absolute $\log_2$ fold change threshold was set to 0 for the comparison between 0.00 μM and 0.05 μM MSC2530818 d20. Overrepresentation analyses of the differentially regulated genes from depicted pairwise comparisons were conducted using "EnrichR" (Kuleshov et al., 2016) within the KEGG, GO-term, Reactome, and BioCharta common database. Rlog transformation of the data was performed for visualization and further downstream analysis.

Reanalysis of publicly available data

Within this study 15 reference gene lists from seven different studies were implemented (listed in Methods S5). Ten gene lists were directly retrieved from the literature, one gene set for pancreatic progenitors (Xie et al., 2013), three gene sets for trunk cells (De Lichtenberg et al., 2018; Krentz et al., 2018), and six gene sets for putative ductal subpopulations (Qadir et al., 2020). Gene sets from (De Lichtenberg et al., 2018) were compiled by filtering the published pairwise comparisons of a putative trunk domain against either tip (trunk1) or early-endocrine (trunk2) cells by a P value lower than 0.05 and sorting according to the 100 genes with the highest fold change (FC).

Five additional gene sets were compiled from raw data. A second pancreatic progenitor gene set was generated from FASTQ files (friendly provided by Neil Hanley) (Gerrard et al., 2016). Data was mapped to the human reference genome GRCh38 and the Gencode gene annotation [v29] with "Star aligner" version 2.6.1.c] (Dobin et al., 2013). Prior mapping sequencing reads were trimmed with "Trimmomatic" [version 0.36] (Bolger et al., 2014). Bases at the start and end of each read, for which the "phread" score was below 25 were removed. Furthermore, reads were clipped if the average quality within a sliding window of 10 fell below a "phread" score of 25. Conclusively, reads smaller than 50 bases were removed. "FeatureCounts" from the "Subread" package [v1.6.3] (Liao et al., 2019) was used to get sample wise gene counts in the stranded mode having the parameter "ignoreDup" set to "False." Resulting gene count lists were imported into R and quantile normalized with "Limma" (Ritchie et al., 2015) using the organ description as covariate during model fitting. Organ specific gene lists have been generated by pairwise comparisons between all investigated organs. All genes found significant in at least on pairwise comparison at an FDR level of 0.05 were subsequently sorted according to their peak expression to assign organ specific gene lists comprising of 100 genes.

Duct-specific gene lists have been generated using scRNA-seq data. For the first dataset (Enge et al., 2017), raw transcript count matrix and annotation data including donor age and cell type clustering information were downloaded from the GEO databank under

Please cite this article in press as: Breunig et al., Modeling plasticity and dysplasia of pancreatic ductal organoids derived from human pluripotent stem cells, Cell Stem Cell (2021), https://doi.org/10.1016/j.stem.2021.03.005

accession number GSE81547. The dataset contained 2527 cells and 23359 genes and for downstream analysis python package "scanpy" (Wolf et al., 2018) was used. For preprocessing, cells with less than 300 counts, cells with less than 300 expressed genes, and genes expressed in less than 10 cells were filtered out. Normalization of the preprocessed raw data was performed using "scran" (Lun et al., 2016) and batch correction for donors was performed using "ComBat" (Johnson et al., 2007). Cluster were assigned as in the original publication (acinar, ductal, mesenchymal, alpha, beta, delta, and unsure). The top 4000 genes with the highest variance were selected to generate UMAPs (Mcinnes et al., 2018). Marker genes were identified using "sc.tl.rank_genes_groups" function (Wolf et al., 2020) for each cell type with default parameters except for "groupby" set to "Celltype." To generate reference input lists a P value lower than 0.01 was used as threshold and the top 100 genes with highest FC were subsequently used for GSEA.

For the second scRNA-seq dataset (Baron et al., 2016), the raw transcript count matrix and annotation data was downloaded from the GEO databank under accession number GSE84133. The dataset contained 8569 cells and 20125 genes. Preprocessing including filtering, normalization, and batch correction was done exactly as described above. Clustering of cells was redone in this study: Cells were clustered using the Louvain algorithm (Traag, 2015; Blondel et al., 2008; Levine et al., 2015) implemented with "scanpy.tl.louvain" function with resolution = 1.0 and further parameters set as default. The clusters obtained from Louvain algorithm were merged into new custom clusters. As part of reclustering, we only focused on cells of interest (acinar, ductal, alpha, beta, combined gamma-epsilon, and delta cells), while omitting non-parenchymal cells (stellate, endothelial, immune, and unknown cells). Subsequent steps including identification of marker genes were identical as in the first scRNA-seq dataset.

From the second scRNA-seq dataset, we additionally generated ductal subpopulation-specific gene lists by assigning *CFTR*^{high} *MUC1*^{low} and *CFTR*^{low} *MUC1*^{high} cell clusters based on the original publication. For that, cells were ranked once according to their expression of *CFTR* and a second time according to their expression of *MUC1*. The difference in ranks was calculated and all cells with a rank score difference (rank_CFTR_minus_MUC1) of at least 100 were assigned to a "ductal_CFTR" cluster and vice versa. Remaining cells were assigned to a third "ductal_other" cluster, which was not further investigated. The additional ranked marker gene list was calculated using the "sc.tl.rank_genes_groups" function (Wolf et al., 2020) for each cell type with "groupby" set to "subClusters" and "groups" set to ["ductal_MUC1," "ductal_CFTR," "ductal_other"] in order to compare "ductal_CFTR" versus "ductal_MUC1." To generate the respective reference input lists a P value lower than 0.01 was used as threshold and all genes, fulfilling the P value criteria (less than 100), were subsequently used for GSEA.

Gene set enrichment analysis (GSEA, Broad Institute)

Gene lists for pairwise comparisons were ranked using $\log_2$("FC_Shrink-apeglm") and ranked lists were analyzed with the "GSEAPreranked" tool of GSEA [version 4.0.3] (Subramanian et al., 2005) using except for the Collapse parameters ("No_collaps") default settings including 1000 permutations with a weighted statistical analysis. For comparison with reference gene sets, gene lists have been either directly compiled from literature or raw data has been reanalyzed as indicated above. A complete list of applied gene sets can be found in Methods S5.

Cell type deconvolution using cell population mapping (CPM)

A recently published cell population mapping algorithm for cell type deconvolution (Frishberg et al., 2019) was implemented with the help of the R package "scBio." Our Rlog transformed bulk RNA data matrix was used in conjunction with the processed scRNA-seq dataset to determine similarity scores of PDLOs (d30) and human primary ductal organoids with the distinct cell types of a human adult pancreas (Enge et al., 2017). Prior running the CPM algorithm, the bulk RNA dataset was reduced to the number of genes that have been used to generate the UMAP representations for the scRNA-seq data (see above).

Heatmap of most significant genes

A heatmap of stage-specific significant genes was generated based on a data matrix including only samples of the time course of differentiation (d0, d3, d13, d20, d24, d30, d45, and d59). Read counts were processed as described above. All genes with a P value ≤ 0.01 and a $\log_2$FC ≥ 2 in at least one pairwise comparison between different time points were ordered according to their peak expression value (Stage-specific Peak expression is listed in Table S1).

Heatmap of target genes/proteins and ward clustering

Heatmaps to illustrate target gene or protein expression were conducted using the packages "pheatmap" for plotting and the package "biomaRt" for retrieval of gene sets from common databases. The function "pheatmap" was used with parameter "scale" set to "row" and "clustering_method" set to "ward.D" and with further parameters set as default. To cluster all samples of the RNA-seq experiment the same function was applied on the entire data matrix containing all processed (15630) genes.

Proteome data analysis

Acquired raw files were mapped with "Maxquant" [version 1.5.7.4] (Cox and Mann, 2008) against the UniProtKB human reference list (downloaded 22.07.2013). For the search settings, up to 2 missed cleavages were allowed, carbamidomethylation was defined as a fixed modification and oxidation of methionine as well as N-terminal protein acetylation were set as variable modifications. Reporter ion MS3 was set as quantification type and TMT10plex as isobaric labels. The first search peptide tolerance was set to 20 ppm and the main search peptide tolerance was set to 4.5 ppm. Results were filtered by setting the protein and peptide false discovery rate to 1% using a classical target-decoy approach. All the following data analysis was performed using R [version 6.1.7601]. From the "Maxquant" output, all reversed and "only identified by site" protein entries were filtered out and the $\log_2$ reporter ion intensities of the three replicates were further "ComBat" (Johnson et al., 2007) adjusted with the "sva" package [version 3.30.1]

(Leek et al., 2012) to correct for batch effects across the measured samples. P values were calculated with the "limma" package [version 3.38.3] and corrected for multiple testing using the Benjamini-Hochberg method (Benjamini and Hochberg, 1995) (Comparison of protein expressionis shown in Table S3).

The mass spectrometry proteomics data have been deposited to the ProteomeXchange Consortium via the PRIDE (Perez-Riverol et al., 2019) partner repository with the dataset identifier PXD018785.

RNA-proteome data comparison

To adjust for different modes of measurement in RNA-seq and full proteome (read counts versus protein intensities), the normalized counts per million (CPM) values and the batch effect corrected reporter ion intensities were normalized with the modified "MComBat" procedure (Frejno et al., 2017) based on the protein data and the correlation was further visualized by histogram plots (package "ggExtra," [version 0.8]).